https://ntrs.nasa.gov/search.jsp?R=19840004244 2020-03-21T01:39:03+00:00Z

NASA-CR-168251
PWA-5777-29

NASA

NASA-CR-168251
19840004244

Final Report

Development of Strain Tolerant Thermal Barrier Coating Systems

Tasks I-III

FOR REFERENCE

NOT TO BE TAKEN FROM THIS ROOM

by
N.P. Anderson
K.D. Sheffler

UNITED TECHNOLOGIES CORPORATION
Pratt & Whitney Aircraft Group
Engineering Division

LIBRARY COPY

JAN 3 1984

LANGLEY RESEARCH CENTER
LIBRARY, NASA
HAMPTON, VIRGINIA

Prepared for

NATIONAL AERONAUTICS AND SPACE ADMINISTRATION

Lewis Research Center
Cleveland, Ohio 44135

Contract NAS3-22548

25 1 1 RN/NASA-CR-168251
DISPLAY 25/2/1
84N12312*# ISSUE 3 PAGE 356 CATEGORY 27 RPT#: NASA-CR-168251 NAS 1.26:168251 PWA-5777-29 CNT#: NAS3-22548 83/09/00 117 PAGES
UNCLASSIFIED DOCUMENT
UTTL: Development of strain tolerant thermal barrier coating systems, tasks 1 - 3
AUTH: A/ANDERSON, N. P.; B/SHEFFLER, K. D.
CORP: Pratt and Whitney Aircraft Group, East Hartford, Conn. CSS: (Engineering Div.) AVAIL.NTIS SAP: HC A06/MF A01
MAJS: /*CERAMIC COATINGS/*COATING/*ENGINE PARTS/*SPRAYED COATINGS/*THERMAL CONTROL COATINGS/*TURBINE BLADES
MINS: / AIRCRAFT ENGINES/ GAS TURBINE ENGINES/ HOT CORROSION/ MICROSTRUCTURE/ OXIDATION RESISTANCE/ PLASMA SPRAYING/ SERVICE LIFE/ SPALLING/ THERMAL CYCLING TESTS/ ZIRCONIUM OXIDES
ABA: M.G.
ABS: Insulating ceramic thermal barrier coatings can reduce gas turbine airfoil metal temperatures as much as 170 C (about 300 F), providing fuel efficiency improvements greater than one percent and durability improvements of 2 to 3X. The objective was to increase the spalling resistance of zirconia based ceramic turbine coatings. To accomplish this, two baseline and 30 candidate duplex (layered MCrAlY/zirconia based ceramic) coatings were iteratively evaluated microstructurally and in four series of laboratory burner rig tests. This led to the selection of two
ENTER:

UNITED TECHNOLOGIES
PRATT&WHITNEY
AIRCRAFT

400 Main Street
East Hartford, Connecticut 06108

In reply please refer to:
KDS:AJG:165-37 (0282I)
Ref. No. PWA-5777-29

November 30, 1983

To: National Aeronautics and Space Administration
Lewis Research Center
21000 Brookpark Road
Cleveland, OH 44135

Attention: Mr. J. P. Merutka
Mail Stop 49-1

Subject: Submittal of Development of Strain Tolerant Thermal Barrier Coating Systems Final Report, Tasks I - III, NASA CR-168251 (PWA-5777-29)

References: (a) NASA Contract NAS3-22548

(b) Letter, Anthony Long to R.M. Gaines, "Contract NAS3-22548 - Approval of Final Draft" dated November 11, 1983, ref. 5121

Enclosures: Twenty-five copies of Subject Report, PWA-5777-29

Dear Mr. Merutka:

In accordance with the requirements of references (a) and (b), we are pleased to submit twenty-five copies of the subject report, which includes all revisions to the draft discussed in the reference (b) letter.

Distribution is being made in accordance with the reference (b) letter.

Sincerely yours,

UNITED TECHNOLOGIES CORPORATION
Pratt & Whitney Aircraft Group
Engineering Division

K. D. Sheffler
Program Manager

1. REPORT NO. NASA-CR-168251	2. GOVERNMENT ACCESSION NO.	3. RECIPIENT'S CATALOG NO.
4. TITLE AND SUBTITLE Development of Strain Tolerant Thermal Barrier Coating Systems, Tasks I - III		5. REPORT DATE September 1983 6. PERFORMING ORG. CODE
7. AUTHOR(S) Neal P. Anderson and Dr. Keith D. Sheffler		8. PERFORMING ORG. REPT. NO. PWA-5777-29
9. PERFORMING ORG. NAME AND ADDRESS UNITED TECHNOLOGIES CORPORATION Pratt & Whitney Aircraft Group Engineering Division East Hartford, CT 06108		10. WORK UNIT NO. 11. CONTRACT OR GRANT NO. NAS3-22548
12. SPONSORING AGENCY NAME AND ADDRESS NATIONAL AERONAUTICS AND SPACE ADMINISTRATION Lewis Research Center 21000 Brookpark Road, Cleveland, Ohio 44135		13. TYPE REPT./PERIOD COVERED Contractor 14. SPONSORING AGENCY CODE

15. SUPPLEMENTARY NOTES
NASA Project Manager, Mr. J . P. Merutka

NASA - Lewis Research Center, 21000 Brookpark Rd., Cleveland, OH 44135

16. ABSTRACT Insulating ceramic thermal barrier coatings can reduce gas turbine airfoil metal temperatures as much as 170°C (about 300°F), providing fuel efficiency improvements greater than one percent and durability improvements of 2 to 3X. The objective of this program was to increase the spalling resistance of zirconia based ceramic turbine coatings. To accomplish this, two baseline and 30 candidate duplex (layered MCrAlY/zirconia based ceramic) coatings were iteratively evaluated microstructurally and in four series of laboratory burner rig tests. This led to the selection of two candidate optimized 0.25 mm (0.010 inch) thick plasma sprayed partially stabilized zirconia ceramics containing six weight percent yttria and applied with two different sets of process parameters over a 0.13 mm (0.005 inch) thick low pressure chamber sprayed MCrAlY bond coat. Both of these coatings demonstrated at least 3X laboratory cyclic spalling life improvement over the baseline systems, as well as cyclic oxidation life equivalent to 15,000 commercial engine flight hours. It is planned that both of these candidate optimized coatings will be evaluated in an experimental engine.

17. KEY WORDS (SUGGESTED BY AUTHOR(S)) Thermal Barrier Coatings Spallation Life Improvement Zirconia Coatings Plasma Spray Coatings	18. DISTRIBUTION STATEMENT		
19. SECURITY CLASS THIS (REPT) UNCLASSIFIED	20. SECURITY CLASS THIS (PAGE) UNCLASSIFIED	21. NO. PGS	22. PRICE *

* For sale by the National Technical Information Service, Springfield, VA 22161

N84-12312#

TABLE OF CONTENTS

TABLE OF CONTENTS (Continued)

LIST OF ILLUSTRATIONS

LIST OF ILLUSTRATIONS (Continued)

LIST OF ILLUSTRATIONS (Continued)

LIST OF ILLUSTRATIONS (Continued)

LIST OF ILLUSTRATIONS (Continued)

LIST OF ILLUSTRATIONS (Continued)

LIST OF ILLUSTRATIONS (Continued)

LIST OF TABLES

1.0 SUMMARY

The use of insulating ceramic thermal barrier coatings on turbine airfoils in aircraft gas turbine engines can reduce metal temperature as much as 170°C (about 300°F). This reduction can be translated into engine performance improvements of more than one percent reduction in specific fuel consumption and/or factors of 2-3X improvement in component durability. The objective of this program was to develop and verify the methodology necessary to improve the resistance of ceramic thermal barrier coating systems to spallation during aircraft gas turbine engine operation. The program focused on increasing thermal barrier coating strain tolerance and thus life through innovative improvements in coating chemistry and processing.

To evaluate candidate approaches, three iterative series of cyclic thermal tests were conducted on 36 different candidate composition/process combinations. Results of these laboratory tests led to selection of two candidate optimized coating systems for experimental engine evaluation. The laboratory test results are summarized below and described in detail in the body of this report. Results of the engine test will be reported in a separate volume.

Task I - Screening of Experimental Coatings and Processes

The objective of this task was to screen 16 initial composition/process combinations and to select four combinations for subsequent optimization in Task II. Two of these 16 initial coatings were "baseline" systems representing the best "state of the art" in coating durability at the beginning of the program. Selection of an additional 14 modified systems was based on structural concepts which previously had been shown to increase the strain tolerance of ceramic coatings. Screening criteria included a critical evaluation of cyclic thermal spall resistance using triplicate rapid cycle* laboratory burner rig tests of each system, together with extensive pre- and post test structural evaluations using light and scanning electron microscopy, electron probe, and x-ray diffraction. All of the coatings evaluated in this and subsequent tasks were two layer systems incorporating a nominal 0.25 mm (0.010 inch) layer of ceramic applied over a nominal 0.13 mm (0.005 inch) layer of NiCoCrAlY** bond coat. Ceramic compositions were based on zirconia stabilized with varying levels of magnesia and yttria, and included various second phase additions designed to promote more strain tolerant structures. The primary ceramic deposition method was air plasma spray; process variables included deposition energy, ceramic residual stress (as controlled through workpiece temperature) and various post-coat thermal stock treatments designed to "segment" the ceramic structure. Electron beam (EB) vapor deposition, which previously had been shown to produce a highly strain tolerant ceramic structure, also was evaluated. For this first task, all specimens coated with plasma sprayed ceramic had an air plasma sprayed bond coat. In all subsequent tasks, plasma sprayed ceramics were applied over a low pressure chamber plasma sprayed bond coat. All EB ceramics were applied over an EB deposited bond coat.

* = Cycle duration 6 minutes:
4 minutes flame immersion with maximum specimen surface temperature controlled to 1107°C (2025°F) - 2 minutes forced air cool
** = Ni - 22%Co - 18%Cr - 12%Al - 0.4%Y (weight percent)

Results of the Task I tests clearly demonstrated that partially stabilized zirconia containing six weight percent yttria was the most durable of the ceramic compositions evaluated. It also was demonstrated that low workpiece temperature, which minimizes compressive residual stresses in the ceramic, provides substantial benefits to cyclic thermal durability. Process variations which produce enhanced ceramic segmentation were shown to have significant promise, and the previously observed benefits of electron beam vapor deposition were confirmed. Typical cyclic lives of the most promising Task I candidates were on the order of 4000 to more than 6000 cycles. The lives of the baseline systems were on the order of 1500 to 2000 cycles. Based on these results, four process variations, including ceramic plasma powder size and morphology, high energy plasma deposition, post-coat thermal shock of plasma coatings, and electron beam vapor deposition were selected for optimization in Task II.

Task II - Coating/Process Improvement

The objective of this task was to optimize the four composition/process combinations identified in Task I. To accomplish this objective, four variations of each of these four combinations were evaluated microstructurally and by cyclic burner rig testing as in Task I. Plasma coatings were made with partially stabilized zirconia containing six weight percent yttria, deposited using workpiece temperature control. Various plasma powder size distributions and shapes were investigated with "baseline" plasma deposition parameters. High energy process variations included reduced standoff (plasma gun to workpiece distance), deposition with a high energy plasma gun, and post coat plasma surface treatment. To promote improved ceramic segmentation, various post coat quenching treatments were investigated using both water and liquid tin as quenching media. Various compositions were applied by electron beam - physical vapor deposition, including mullite and zirconia stabilized with varying levels of yttria and ceria.

Results of the burner rig evaluations indicated that the "baseline" plasma spray coating was optimized with coarse (45% +325 mesh) spherical ceramic powder. The average cyclic life of this coating was 6647 cycles. Among the various high energy deposition processes evaluated, the best results were obtained with standoff reduced to one third of the 7.6 cm (three inch) baseline distance which provided an average life of 6843 cycles. None of the quenching variants investigated in this task worked as well as the liquid tin quench from 1079°C (1975°F) employed in the Task I evaluation which produced an average life of 5425 cycles. Excellent cyclic thermal performance was demonstrated for electron beam physical vapor deposited zirconia stabilized with either six or 12 percent yttria. While some failures occurred at about 5500 cycles, most tests of this coating were discontinued in the range of 6000 to 8000 cycles without failures.

Based on these results three plasma spray and one electron beam vapor deposited six percent yttria zirconia ceramic coatings were selected for cyclic oxidation and hot corrosion evaluation in Task III. All four of the selected candidates demonstrated at least 3X rapid cycle thermal spall life improvement relative to the average baseline performance measured in Task I.

Task III - Coating Durability

The objective of this task was to evaluate the four candidate optimized coatings identified in Task II using cyclic oxidation and hot corrosion conditions which more realistically simulate those encountered in commercial aircraft turbine engine operation. The three candidate plasma coatings all were fabricated with coarse spherical powder and workpiece temperature control. Plasma process variations included the baseline 7.6 cm (three inch) and 2.5 cm (one inch) standoffs, and post coat liquid tin quenching from 1079°C (1975°F).

Cyclic Oxidation Testing

The objective of this test was to evaluate the cyclic thermal durability of candidate coatings using test conditions which realistically simulate the oxidizing conditions encountered in commercial gas turbine engine flight operations. As in Tasks I and II, these tests were conducted in a cyclic burner rig. Primary differences between these tests and those conducted in the first two tasks were the employment of a longer cycle time (one hour as opposed to six minutes) to better simulate flight exposure times, and continuous internal cooling of the test specimens to simulate the thermal gradient across the wall of an internally cooled turbine airfoil. The 60 minute test cycle consisted of 57 minutes immersion in the combustion flame and three minutes forced air cooling. Tests were conducted with a ceramic surface temperature of 1148°C (2100°F) and a metal substrate temperature of 982°C (1800°F).

Results of these tests indicated the quenched ceramic coating system to have relatively poor oxidation resistance, with the performance of other three coatings [EB and plasma with 2.5 cm (one inch) and 7.6 cm (three inch) standoff distances] being relatively similar. Based on an average hot exposure time of about 350 hours, the performance of these latter three coatings was judged equivalent to over 15,000 hours of typical commercial flight service.

Cyclic Hot Corrosion Testing

The objective of this testing was to evaluate the cyclic durability of candidate coatings in a hot corrosion environment. To accomplish this objective, burner rig tests were conducted with 30.5 liters/hr SO_2 (which converts to SO_3 during combustion) and 20 ppm synthetic sea salt (ASTM D-1141-52) added to the burner primary air supply. The specimens were exposed to a ceramic surface temperature of 954°C (1750°F) and an inner diameter metal temperature of 898°C (1650°F) for 57 minutes in a ducted rig, followed by three minutes of forced air cooling. Results of these tests indicated that the plasma spray coating system produced with a 2.5 cm (one inch) standoff performed significantly better than the other three coating systems, which were grouped relatively closely at about 420 hours to failure. Experience with metallic coating systems indicates that with the levels of salt and sulfur utilized for this testing, metallic coating rig lives are less than typical service lives by 2 to 5X. However, not enough is currently known about life prediction of ceramic coating performance from laboratory data to quantitatively predict airfoil coating life from these data.

Selection of Coatings for Engine Evaluation

Based on results of the first three tasks, two of the four coating/process systems evaluated in Task III were selected for future evaluation in a ground based experimental gas turbine engine. The plasma spray coating made with a 2.5 cm (one inch) standoff distance was selected on the basis of its combination of good performance in the Task III cyclic oxidation and hot corrosion tests. The quenched coating was not selected because of its poor performance in cyclic oxidation testing. While performance of the electron beam physical vapor deposited coating was generally outstanding in all tests except for cyclic hot corrosion, this coating was not selected because reproducible process methods for application to complex geometry turbine components have not yet been demonstrated. The plasma spray coating produced with a 7.6 cm (three inch) standoff distance thus was selected as the second coating system to be engine tested. Both of these systems will be made with coarse spherical partially stabilized zirconia powder containing six weight percent yttria, and will be plasma sprayed on experimental turbine blades using workpiece temperature control.

2.0 INTRODUCTION

The use of ceramic thermal barrier coatings on turbine airfoils in aircraft engines is providing substantial improvements in operating economy through reductions in fuel usage and maintenance requirements. Ceramic coatings provide the same impact as major recent advances in engine materials such as directional solidification and single crystal technology. For instance, the capability of these insulating coatings to reduce turbine airfoil metal temperatures by as much as 100 to 300°F can be translated into engine performance improvements of more than a one percent reduction in specific fuel consumption and/or a two to threefold improvement in component durability. Additional benefits are derived from damping of airfoil thermal fatigue crack inducing temperature gradients during engine operating transients.

Ceramic coating systems have been used for over 20 years to decrease the severity of oxidation damage and improve the cracking resistance of combustors and afterburners. However, it was not until the past decade that these coatings were considered for use on turbine section airfoils, which operate in a more severe thermal environment. In the mid 1970's, a series of successful engine tests of ceramic coated turbine blades at NASA's Lewis Research Center demonstrated that thermal barrier coating of turbine airfoils was feasible (Reference 1). This result led to an expanded effort at industrial and Government laboratories to define the actual capabilities of then state-of-the-art thermal barriers, their deficiencies, and methods for improvement. Additional engine tests of coated turbine blades showed that still greater ceramic spall resistance was required (References 2, 3), and laboratory experiments uncovered susceptibility to thermal barrier degradation from oxidation and hot corrosion effects (References 2, 4, 5, 6). Nevertheless, some of these studies indicated that considerable improvements in ceramic coating durability could be achieved (References 3, 7). In particular, it was found that a considerable increase in zirconia spall resistance was achieved when certain strain tolerant microstructures were built into the deposited ceramic layer through process variations (References 3, 8, 9, 10, 11).

Currently, combinations of oxidation, hot corrosion, stress induced spallation and erosion in the operating environment are limiting the life of ceramic coatings (References 2, 4, 5, 6). To improve the durability of these coatings, there must be better adhesion of the coating system to the substrate and improved cohesion within the ceramic layer. In addition, the ability of the ceramic layer to accommodate strains resulting from thermal transients, temperature gradients through the coating, and thermal expansion mismatch must be improved.

The objective of this program was to develop and verify the methodology necessary to improve the resistance of thermal barrier coating systems to spallation during aircraft gas turbine engine operation. The program focuses on increasing thermal barrier coating strain tolerance and thus life through innovative improvements in coating chemistry, processing, process control and through procedures other than plasma spraying such as electron beam vapor deposition of ceramics. To accomplish these objectives, a research program was conducted consisting of the following three tasks.

Task I - Experimental thermal barrier coating systems based on structural concepts which have been shown to increase the strain tolerance of ceramic coatings were deposited on test specimens and subjected to burner rig screening tests. Based on the ranking tests and post test evaluation, four coating/process systems were selected for further improvement and evaluation in Task II.

Task II - A system improvement study was conducted to optimize each of the four systems selected in Task I. Four variations of each of the four coating/process combinations were identified for further burner rig testing. Based on the results of these tests, four coating/process systems were selected for further improvement and evaluation in Task III.

Task III - The four coatings selected in Task II were subjected to cyclic oxidation exposure and to cyclic hot corrosion exposure. Based on results of these tests, two coating/process systems were selected for engine evaluation.

This final report discusses results of the three tasks described above. A fourth task will involve experimental engine evaluation of the two selected systems.

3.0 TASK I - COATING/PROCESS SCREENING

The objective of this task was to screen the cyclic thermal durability of sixteen candidate thermal barrier coating systems and to select four of these systems for compositional and process optimization in Task II. Screening was accomplished by cyclic burner rig testing at 1107°C (2025°F) as described in Appendix A. Substantial pre- and post test coating structural evaluation was performed to aid in interpreting the rig test results and in selecting approaches for Task II optimization. Results of this test and evaluation program are described in the following sections.

3.1 CANDIDATE SYSTEMS

The sixteen candidate coating systems selected for evaluation in this task are listed in Table 3-I. These are all two layer coatings, consisting of a 0.10 to 0.15 mm (0.004 to 0.006 inch) inner layer of oxidation resistant NiCoCrAlY(*) and an 0.20 to 0.30 mm (0.008 to 0.012 inch) outer layer of insulating ceramic. With the exception of system 16, all metallic and ceramic coatings were applied by air plasma spray. Both layers of system 16 were applied by electron-beam physical vapor deposition. The compositions and processes listed in Table 3-I were selected on the basis of previously available data indicating the potential for improved strain tolerance; that is, increased ability to tolerate the cyclic thermal and mechanical strains imposed on the ceramic during operation in a gas turbine engine (References 3, 8, 9, 11, 12). The specific mechanisms incorporated in each of these systems for strain tolerance improvement are described in the following paragraphs.

All of the candidate ceramics investigated in this program were based on zirconia (ZrO_2), which exhibits an unusual combination of low thermal conductivity, relatively high thermal expansion, and good environmental stability. Low conductivity is required to provide the thermal insulation capability inherent to the thermal barrier concept. High ceramic thermal expansion minimizes ceramic strains resulting from large differences between the relatively high expansion of typical nickel and cobalt turbine alloys and the typically much smaller expansion of ceramics. These differential thermal expansion strains are considered to be primarily responsible for spalling encountered with earlier generation thermal barrier coatings. Environmental stability is needed to survive in the uniquely hostile gas turbine combustion environment.

(*) Ni - 22 w% Co - 18 w% Cr - 12 w% Al - 0.4 w% Y (Note that all compositions in this report are listed in weight percent.)

TABLE 3-I

COATING SYSTEMS SELECTED FOR TASK I EVALUATION

Ceramic Coating Type	Coating System Number	Ceramic Layer	Substrate Temperature During Coating°C(°F)	Post Coating Processing
A Baseline	1	8 w% Y_2O_3 - ZrO_2	Uncontrolled	1079°C(1975°F)/4 hrs/H_2
Baseline	2	21 w% MgO - ZrO_2	Uncontrolled	None
B Substrate Temperature Controlled Plasma Spray Process	3	6 w% Y_2O_3 - ZrO_2	149 (300)	1079°C(1975°F)/4 hrs/H_2
	4	20 w% Y_2O_3 - ZrO_2	149 (300)	1079°C(1975°F)/4 hrs/H_2
	5	21 w% MgO - ZrO_2	149 (300)	None
C New Microcracked Ceramics	6	85 w% (20 w% YSZ) + 15 w% Al_2O_3	149 (300)	1079°C(1975°F)/4 hrs/H_2
	7	85 w% (20 w% YSZ) + 15 w% MgO	149 (300)	1079°C(1975°F)/4 hrs/H_2
D High Energy Input (2.5 cm; 1 inch standoff)	8	6 w% Y_2O_3 - ZrO_2	149 (300)	1079°C(1975°F)/4 hrs/H_2
	9	20 w% Y_2O_3 - ZrO_2	149 (300)	1079°C(1975°F)/4 hrs/H_2
E High Energy Input (High energy gun)	10	21 w% MgO - ZrO_2	149 (300)	None
	11	6 w% Y_2O_3 - ZrO_2	149 (300)	1079°C(1975°F)/4 hrs/H_2
F Post Plasma Spray Thermal Shock	12	21 w% MgO - ZrO_2	149 (300)	221°C(430°F) Liquid Tin Quench from 1079°C (1975°F)/Air
	13	6 w% Y_2O_3 - ZrO_2	149 (300)	221°C(430°F) Liquid Tin Quench from 1079°C (1975°F)/Air
	14	20 w% Y_2O_3 - ZrO_2	149 (300)	221°C(430°F) Liquid Tin Quench from 1079°C (1975°F)/Air
G Micro-Porosity	15	20 w% Y_2O_3 - ZrO_2 + 15 w% carbon	149 (300)	1079°C(1975°F)/4 hrs/Air
H Micro-Segmented	16	20 w% Y_2O_3 - ZrO_2 (EB-PVD)	--	1079°C(1975°F)/4 hrs/H_2

Notes:

Two layer systems; ceramic thickness 0.20 to 0.30 mm (0.008 to 0.012 inch), Metallic layer thickness 0.10 to 0.15 mm (0.004 to 0.006 inch). Metallic layer composition, Ni - 22 w% Co - 18 w% Cr - 12 w% Al - 0.4 w% Y. All Metallic and ceramic coatings applied by air Plasma spray except system 16, both layers of which were applied by Electric Beam - Physical Vapor deposition (EB-PVD). Except as indicated, ceramic spray stand off (Plasma spray gun to workpiece distance) was 7.6 cm (3 inches).

w% = weight percent
YSZ = yttria stabilized zirconia
EB-PVD = Electron Beam-Physical Vapor Deposition

All of the zirconia compositions listed in Table 3-I contain additives to stabilize the cubic crystal structure. Pure zirconia is subject to reversible allotropic phase transformations among three different crystal polymorphs which are stable in different temperature ranges. Density changes associated with these transformations, particularly the tetragonal-monoclinic transformation which occurs at temperatures in the gas turbine operating range, can lead to massive internal strains and consequent spalling of the ceramic coating. These allotropic phase transformations are controlled by alloy additions which tend to stabilize the high temperature cubic crystal structure at lower temperatures (References 13, 14, 15).

The various ceramic types listed in Table 3-I represent different approaches to enhance ceramic strain tolerance and durability. A description of the general concept of microstructural strain tolerance enhancement is provided below. Succeeding paragraphs will describe each of the selected systems in terms of these concepts.

Studies of ceramic coating degradation and failure mechanisms indicate that spalling results from propagation of cracks parallel to, or coincident with, the ceramic/metal interface (References 16, 17, 18, 19, 20). The crack driving forces are stresses generated primarily by differential thermal expansion strains between the ceramic and the metal. Because metals typically expand more than ceramics, ceramic coating strains tend to be predominantly tensile at elevated temperatures. One approach to increased coating durability is to decrease the crack driving force (stress). This can be accomplished by increasing ceramic tensile compliance in the plane of the coating, thus reducing the magnitude of crack tip stress fields developed by thermally induced ceramic tensile strains. As illustrated in Figure 3-1, tensile compliance of a ceramic can be increased by careful control of ceramic microstructure. The ideal ceramic microstructure (Figure 3-1a) consists of aligned ceramic columns, each of which is strongly bonded to the metal substrate but is structurally independent of adjacent columns. The in-plane tensile compliance of this coating is essentially infinite, so that crack driving stresses developed by in-plane tensile displacements are virtually zero. A less idealized form of this compliance enhancement feature is shown in Figure 3-1b. This structure is less desirable than that shown in Figure 3a because the larger segments permit higher thermal stress to develop within each segment. The extensive network of extremely, fine, short cracks shown in Figure 3-1c and the porosity shown in Figure 3-1d represent other types of structures which enhance ceramic compliance. Careful process control is required in fabrication of coatings with these favorable structures to avoid development of unfavorable features such as cracks parallel to the plane of the coating, which represent built-in failure initiation sites. The application of these idealized strain tolerant features in each of the selected Task I candidates is described in more detail in the following paragraphs.

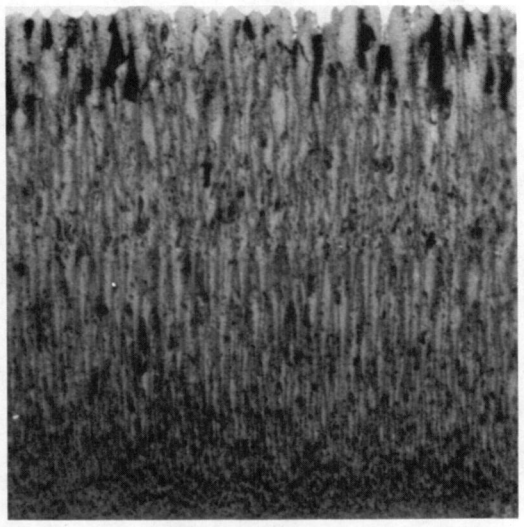

a. CERAMIC SEGMENTATION 220X

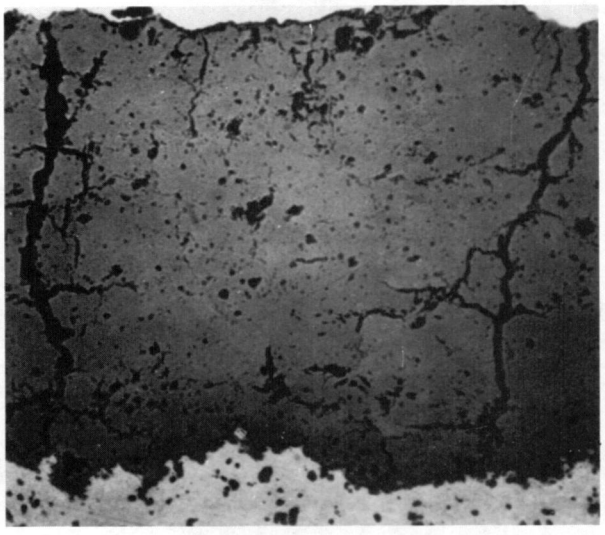

b. SEGMENTATION CRACKING 200X

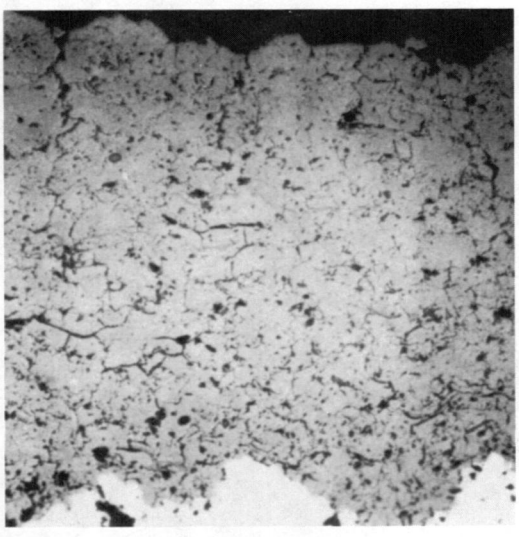

c. MICROCRACKING 200X

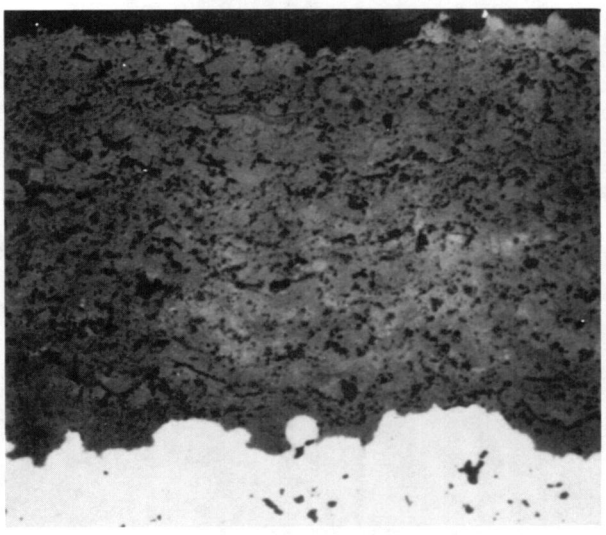

d. POROSITY 200X

Figure 3-1 Microstructural Features which Enhance the Strain Tolerance of Ceramic Coatings

Coating systems 1 and 2 in Table 3-I represent baseline systems against which the performance of other experimental systems was compared. Coating system 2 incorporates a ceramic composition for which substantial service experience exists as a combustor thermal barrier coating. This composition naturally develops internal microcracking during plasma deposition. The NASA developed 6 to 8 w% Y_2O_3 - ZrO_2 ceramic (system 1) was selected as a second baseline representative of the state-of-the-art (Reference 17).

The primary goal of coating systems 3, 4, and 5 was to demonstrate the durability benefits of substrate temperature control with ceramic compositions which tend to exhibit different strain tolerant microstructural features. Prior work (Reference 8) had shown that the partially stabilized 6 w% Y_2O_3 - ZrO_2 composition (system 3) naturally favors the formation of segmentation cracks, while the fully stabilized 20 w% Y_2O_3 - ZrO_2 composition (system 4) can be easily sprayed with a relatively high porosity level. System 5 was included to allow direct assessment of substrate temperature control benefits through comparison with system 2.

Control of substrate temperature was expected to enhance coating durability by controlling residual compressive stresses in the ceramic layer. With the exception of porosity, the microstructural compliance enhancement features illustrated in Figure 3-1 effectively reduce only tensile stresses. In compression, compliance decreases as segmentation and microcracks close, leading to high compressive stresses and attendant ceramic spalling. To avoid development of high compressive stresses, the temperature of the metal substrate is controlled during coating application so that minimal compressive ceramic residual strains are developed during thermal cycling. There was sufficient prior experience with, and confidence in, the benefits of substrate temperature control (Reference 11) that it also was used in conjunction with the balance of the plasma spray systems described below.

Systems 6 and 7 in Table 3-I represent compositional modifications intended to enhance microcracking in a fully stabilized (cubic) zirconia. The approach involves incorporation of an extremely fine dispersion of second phases with either higher (MgO) or lower (Al_2O_3) expansion coefficients than ZrO_2. Differential expansion or contraction of the dispersoids with respect to the ZrO_2 matrix was expected to promote microcracking of the matrix during thermal cycling.

Systems 8 through 14 incorporate process variations which were intended to promote segmentation cracking in various compositions, either through increased deposition energy (reduced stand-off or high energy spray gun) or through post-coat thermal shock (quenching). Increased deposition energy promotes segmentation cracking in two ways. First, higher particle energy (either thermal or kinetic) at the point of workpiece impact increases consolidation, resulting in a more dense ceramic microstructure that is less strain tolerant and more susceptible to segmentation cracking. Secondly, the higher energy content of the transient thermal pulse created by passage of the high energy plasma flame over the workpiece creates higher transient thermal strains which promote the formation of segmentation cracks in the more susceptible dense and brittle ceramic structure. Quenching provides an alternative means to promote segmentation cracking by application of an extremely large transient thermal strain pulse to a previously applied ceramic.

System 15 represents an attempt to produce controlled porosity through incorporation of a fine dispersion of carbon which subsequently oxidizes to a gaseous phase (CO/CO_2) during heat treatment in air.

System 16 represents a fundamentally different ceramic deposition process which produces an extremely fine, strain tolerant columnar structure such as that shown in Figure 3-1a. Although the process technology for this coating is in a relatively early stage and is not considered ready for coating of turbine components, this coating was included to evaluate the benefits which could be achieved as the process technology matures.

3.2 SPECIMEN PREPARATION AND CHARACTERIZATION

The specimen used for burner rig evaluation of all candidate coatings is described in Appendix A. With the previously noted exception of coating system 16, all Task I metallic and ceramic coatings were applied by plasma spray in the Pratt & Whitney Aircraft Manufacturing Research and Development Laboratory. Gun and specimen manipulations were mechanized to provide uniform and reproducible coating thickness control. For Task I only, the metallic bond coat consisted of a nominal 0.03 mm (0.001 inch) layer of air plasma sprayed metallic applied using the parameters shown in Table 3-IIC over a nominal 0.13 mm (0.005 inch) layer of low pressure chamber sprayed metallic applied using the parameters shown in Table 3-IID. Ceramic systems 1 through 9 and 12 through 15 were applied using a Plasmadyne SG-100 gun operating at the parameters noted in Table 3-IIa. Systems 10 and 11 were applied using an Electro-Plasma high energy spray system operating as indicated in Table 3-IIb. Control of substrate temperature during deposition of ceramic systems 3 through 15 was accomplished using the apparatus illustrated in Figure 3-2, which provides the capability to internally cool the specimen during coating deposition. Specimens coated with systems 12 through 14 were quenched in a 221°C (430°F) liquid tin bath immediately following heat treatment at 1079°C (1975°F). The system 16 coating was deposited in the Materials Engineering Research Laboratory using an Airco 10KW electron beam gun operating in a vacuum chamber at pressures in the order of 10^{-4} to 10^{-6} Torr. Specimens were rotated above the electron beam pool to provide a uniform application of vapor deposited coating. All specimens except those coated with 21 w% MgO - ZrO_2 were heat treated at 1079°C (1975°F) for four hours. Heat treatment was performed in hydrogen except for the specimens coated with 20 w% Y_2O_3 - ZrO_2 + carbon (system 15) and the specimens which were quenched in liquid tin immediately following heat treatment (systems 12 through 14). These coatings were heat treated in air.

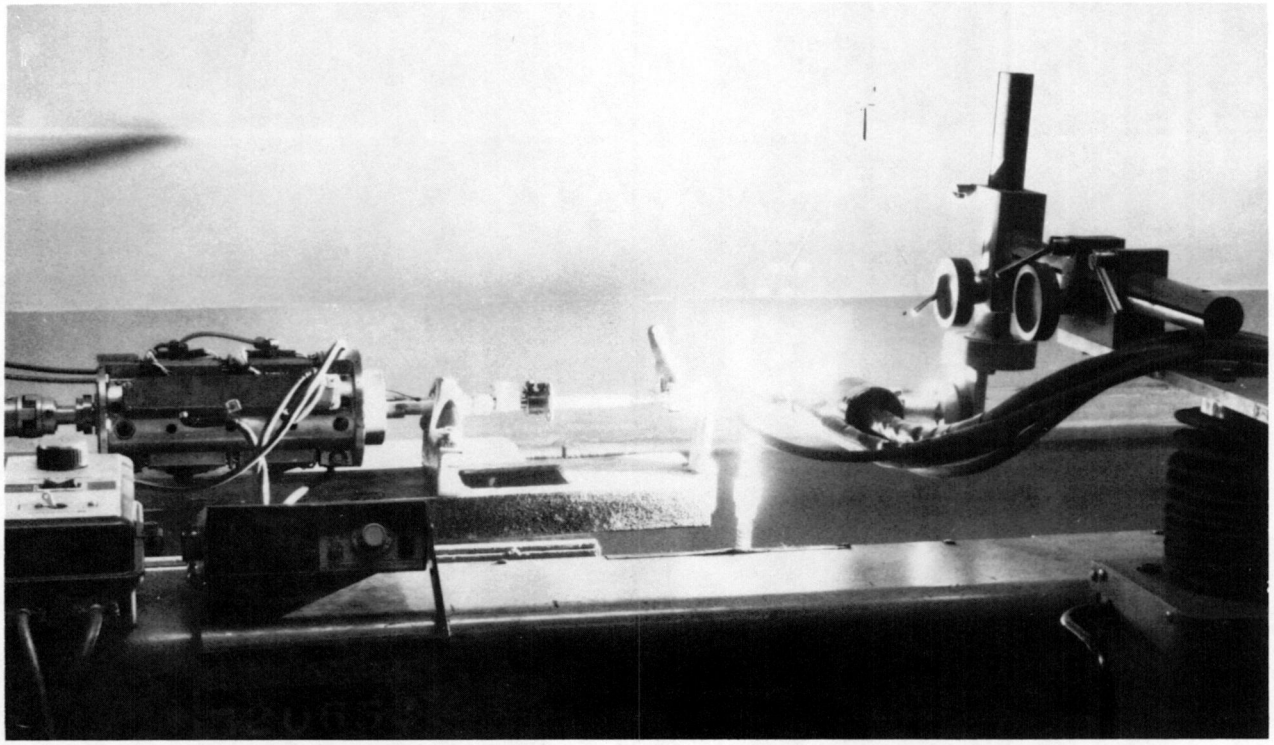

a. CERAMIC COATING BEING APPLIED

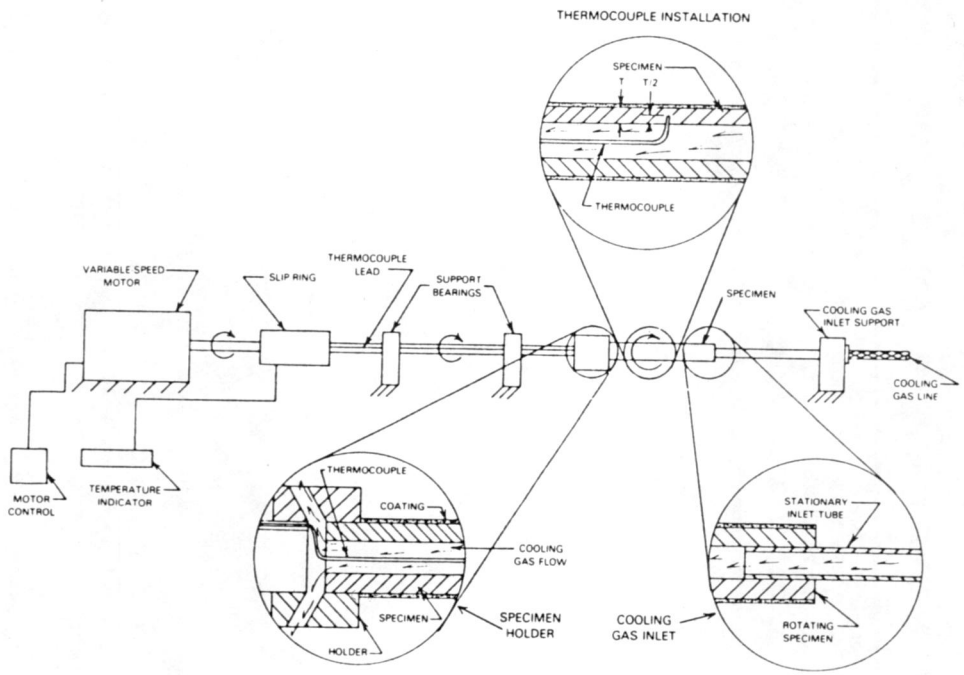

b. SCHEMATIC ILLUSTRATION OF APPARATUS

Figure 3-2 Apparatus Used to Ceramic Coat Burner Rig Test Specimens with Controlled Substrate Temperture

TABLE 3-II
DEPOSITIONS PARAMETERS FOR PLASMA SPRAY COATINGS

	A) Ceramic Systems 1-9 and 12-15 (Plasmadyne SG-100 Gun)	B) Ceramic Systems 10 and 11 (Electroplasma High Energy Gun)	C) Metallic Air Spray Overcoat, Systems 1-15 (Plasmadyne SG-100 Gun)	D) Metallic LP Chamber Spray Undercoat, Systems 1-15 (Electroplasma High Energy Gun)
Gun Voltage	42 volts	55 volts	47 volts	58 volts
Gun Current	900 amps	1600 amps	600 amps	1500 amps
Gun Power	37.8 kw	88 kw	28.2 kw	87 kw
Standoff(1)	7.6 cm (3 in.)(2)	31.8 cm (12.5 in.)	7.6 cm (3 in.)	38.1 cm (15 in.)

(1)Distance between gun nozzle and specimen surface
(2)Except as noted in Table 3-I

Prior to burner rig testing, the tip of each test specimen was removed for documentation of as-deposited coating structure. Metallography and x-ray diffraction were used to evaluate ceramic microstructure and phase distribution. All pre- and post-test x-ray diffraction measurements in this and subsequent Tasks were made from the ceramic surface of in-situ coatings. Results of these evaluations are described in the following paragraphs.

Results of the pre-test x-ray diffraction phase analysis of the ceramic coating surface are tabulated in Table 3-III together with results obtained on the same coatings after burner rig exposure; these latter results will be described in a later section.

Inspection of the pre-test results indicates the 20 w% Y_2O_3 - ZrO_2 composition to be the most "fully stabilized" of the four compositions evaluated, ranging from 100% cubic in the vapor deposited form to less than 5% monoclinic for the various plasma sprayed coatings. In the case of the "enhanced microcracking" coatings (systems 6 and 7), substantial free alumina was detected in the alumina-containing coating; free magnesia, on the other hand, was not found in the MgO containing 20 w% Y_2O_3 - ZrO_2 ceramic. The former result was expected, as Al_2O_3 exhibits virtually no solubility in ZrO_2 at lower temperatures. The absence of free MgO in system 7 is puzzling, since MgO also has low solubility in pure ZrO_2. It may be that the presence of yttria in solution alters the solubility of ZrO_2 for MgO.

Analysis of the 21 w% MgO - ZrO_2 coating is, for the most part, more consistent with expected behavior, with between 8% and 17% free MgO being found in the as-deposited coatings. With one exception, the cubic zirconia phase appears to be highly stabilized, with only small amounts of monoclinic and tetragonal ZrO_2 being found. The exception is the quenched coating (system 12) which is the only 21 w% MgO - ZrO_2 ceramic to be thermally

TABLE 3-III

X-RAY DIFFRACTION PHASE ANALYSIS OF CERAMIC SURFACE

Coating System Number	Ceramic Layer	Substrate Temperature During Coating °C (°F)	Post Coating Processing	Exposure(1) Cycles for Post Test Specimen	VOLUME/PERCENT OF PHASE PRESENT(2)											
					Cubic ZrO_2		Tetragonal ZrO_2		Monoclinic ZrO_2		Cubic MgO		Alpha Al_2O_3		Delta Al_2O_3	
					Pre-Test	Post Test	Pre-Test	Post Test	Pre-Test	Post Test	Pre-Test	Post Test	Pre-Test	Post Test	Pre-Test	Post Test
1	8 w% Y_2O_3 - ZrO_2	Uncontrolled	1079°C (1975°F)/ 4 hrs/H_2	1770	42	30	57	65	1	5						
2	21 w% MgO - ZrO_2	Uncontrolled	None	1690	83	40			-	45	17	15				
3	6 w% Y_2O_3 - ZrO_2	149 (300)	1079°C (1975°F)/ 4 hrs/H_2	4820	40	27	55	71	5	2						
4	20 w% Y_2O_3 - ZrO_2	149 (300)	1079°C (1975°F)/ 4 hrs/H_2	660	97	96			3	4						
5	21 w% MgO - ZrO_2	149 (300)	None	1480	83	35	5	-	-	47	12	18				
6	85 w% (20 w% YSZ) + 15 w% Al_2O_3	149 (300)	1079°C (1975°F)/ 4 hrs/H_2	390	88	95			2	4			8	1	2	-
7	85 w% (20 w% YSZ) + 15 w% MgO	149 (300)	1079°C (1975°F)/ 4 hrs/H_2	190	98	92			2	5	-	3				
8	6 w% Y_2O_3 - ZrO_2 (2.5 cm (1 inch) gun distance)	149 (300)	1079°C (1975°F)/ 4 hrs/H_2	2470	35	12	60	87	5	1						
9	20 w% Y_2O_3 - ZrO_2 (2.5 cm (1 inch) gun distance)	149 (300)	1079°C (1975°F)/ 4 hrs/H_2	350	96	95			4	5						
10	21 w% MgO - ZrO_2 (High energy gun)	149 (300)	None	1930	92	33	-	-	-	60	8	7				
11	8 w% Y_2O_3 - ZrO_2 (High energy gun)	149 (300)	1079°C (1975°F)/ 4 hrs/H_2	6110	100	23	-	75	-	2						
12	21 w% MgO - ZrO_2	149 (300)	221°C (430°F) Liquid Tin Quench from 1079°C (1975°F)/Air	1280	45	42	50	-	5	40		18				
13	6 w% Y_2O_3 - ZrO_2	149 (300)	221°C (430°F) Liquid Tin Quench from 1079°C (1975°F)/Air	4820	35	33	60	67	5	-						
14	20 w% Y_2O_3 - ZrO_2	149 (300)	221°C (430°F) Liquid Tin Quench from 1079°C (1975°F)/Air	1060	96	96			4	4						
15	20 w% Y_2O_3 - ZrO_2 + carbon	149 (300)	1079°C (1975°F)/ 4 hrs/Air	620	96	96			4	4						
16	20 w% Y_2O_3 - ZrO_2	-	1079°C (1975°F)/ 4 hrs/H_2	6200	100	100										

(1) 1107°C(2025°F)/4 Min., Forced Air Cool/2 Min.
(2) Accuracy Tolerances Generally Are ±5%
(3) YSZ = Yttria stabilized zirconia

exposed at 1079°C (1975°F) prior to testing. This coating consists of approximately equal amounts of cubic and tetragonal ZrO_2, with 5% monoclinic and no free magnesia. The high percentage of tetragonal ZrO_2 may result from equilibration in a two-phase field at 1079°C (1975°F); the absence of free magnesia in the thermally exposed system 12 coating is not understood.

With the exception of system 11, results for the "partially stabilized" 6 w% and 8 w% Y_2O_3 - ZrO_2 compositions indicate between 55 and 60% tetragonal phase after the 1079°C (1975°F) thermal exposure, with between 1 and 5% monoclinic and the balance cubic zirconia. The existence of the system 11 ceramic in the fully cubic form, even after heat treatment, is not understood.

Pre-test metallographic examination revealed a variety of ceramic microstructures having various strain relief features, as shown in Figures 3-3 through 3-18. Representative Task I plasma spray bond coat microstructures are included in Figure 3-3. Microstructures of the bond coat on systems 2 through 15 are identical to those shown for system 1 in Figure 3-3. Specific features identified in the various ceramic systems are described in the following paragraphs.

Plasma sprayed coatings which exhibit prominent segmentation cracking include system 1 (8 w% Y_2O_3 - ZrO_2 plasma sprayed without substrate temperature control) shown in Figure 3-3a, and systems 8 and 9 (6 and 20 w% Y_2O_3 - ZrO_2 plasma sprayed at 1 inch gun-to-specimen distance) shown in Figures 3-10a and 3-11a. The higher than normal temperature generated in the absence of substrate temperature control during deposition of coating system 1 resulted in conditions which favored the formation of a moderate level of segmentation cracking. A high level of segmentation cracking was promoted by the high energy input employed in deposition of systems 8 and 9. The relatively coarse segmentation cracking of these plasma sprayed coatings contrasts sharply with the fine columnar microsegregation inherent to the EB-PVD coating (system 16, Figure 3-18a).

Coatings exhibiting moderate levels of strain relief cracking include systems 3, 4, 13, and 14 [6 w% Y_2O_3 - ZrO_2, 149°C (300°F) substrate control; 20 w% Y_2O_3 - ZrO_2, 149°C (300°F) substrate temperature control; 6 w% Y_2O_3 - ZrO_2, liquid tin quenched from 1079°C (1975°F); and 20 w% Y_2O_3 - ZrO_2, liquid tin quenched from 1079°C (1975°F), respectively]. Photomicrographs of these coatings are shown in Figure 3-5a, -6a, -15a, and -16a. Small amounts of cracking were observed in the as-deposited 21 w% MgO_2 - ZrO_2 coatings (systems 2, 5, 10, and 12, see Figures 3-4a, -7a, -12a, and -14a.) As shown in the corresponding photomicrographs, the amount of microcracking found in the 21 w% MgO - ZrO_2 coatings increases substantially during cyclic thermal response. While some of these 21 w% MgO - ZrO_2 coatings appear to have relatively high levels of porosity (see for example Figure 3-7a), this is believed to be an effect of the polishing process. The 21 w% MgO - ZrO_2 coating is very difficult to polish without pullout.

Examination of coatings to which fugitive and differential expansion diluents were added provides several interesting observations. While the Al_2O_3 additive in system 6 was not clearly visible in the light metallograph (Figure 3-8a), x-ray distribution maps of this coating clearly show the presence of

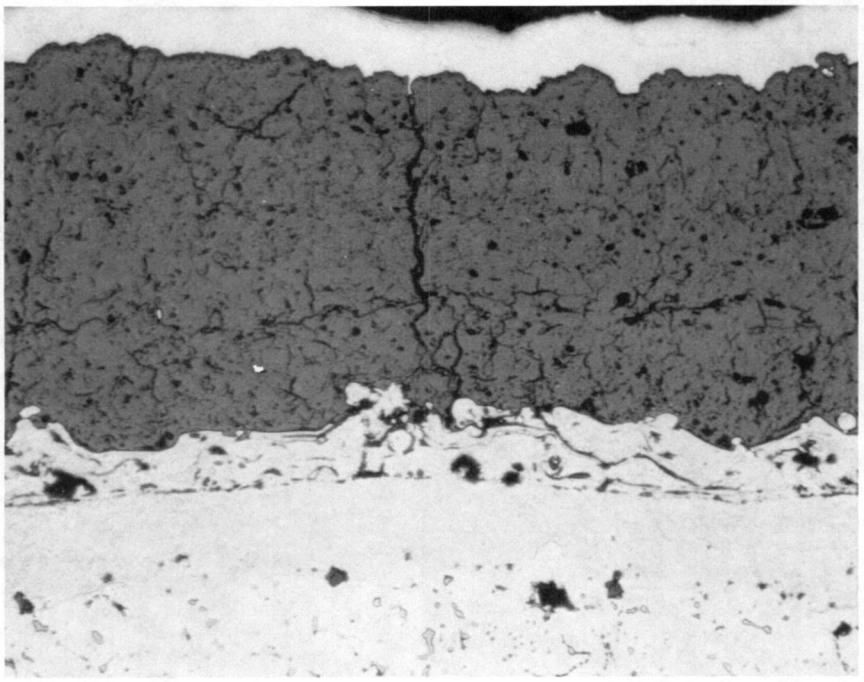

200X

a. PRE-TEST LIGHT PHOTOMICROGRAPH. NOTE SEGMENTATION CRACK THROUGH THE THICKNESS OF CERAMIC COATING.

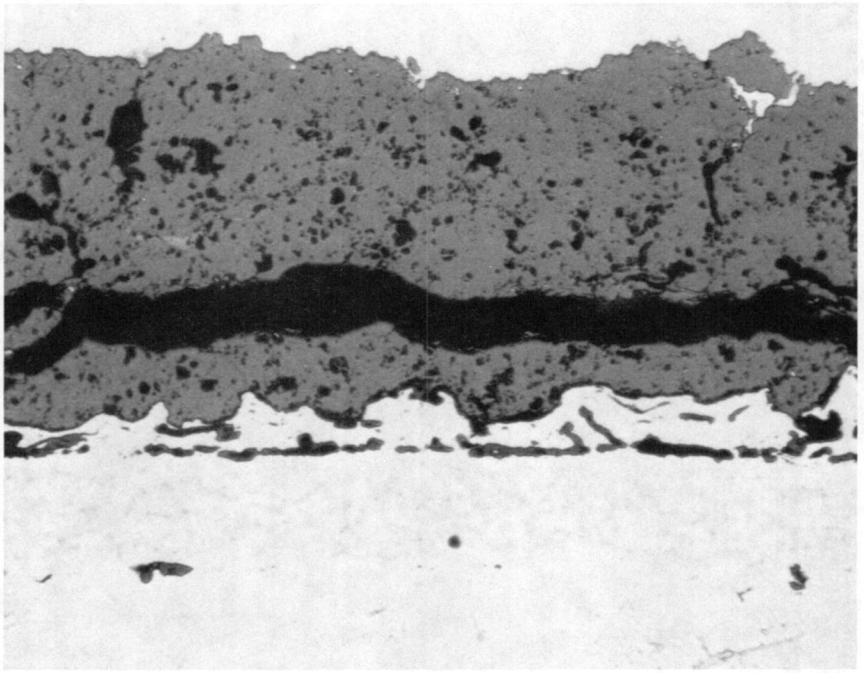

200X

b. POST-TEST LIGHT PHOTOMICROGRAPH. NOTE DOMINANT IN-PLANE CRACK NEAR METAL/CERAMIC INTERFACE.

Figure 3-3 Microstructures of Task I Coating system 1 [8 w% Y_2O_3 - ZrO_2 Plasma Sprayed with Uncontrolled Substrate Temperature] before and after 1770 Cycles of Burner Rig Exposure at 1107°C (2025°F)

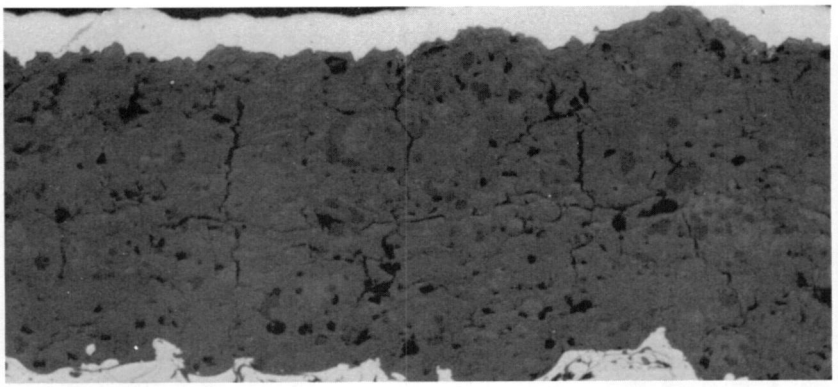

200X

a. PRE-TEST LIGHT PHOTOMICROGRAPH. NOTE EXTENSIVE MICROCRACKING WITH SAME TENDENCY FOR THE FORMATION OF INCIPIENT SEGMENTATION CRACKS.

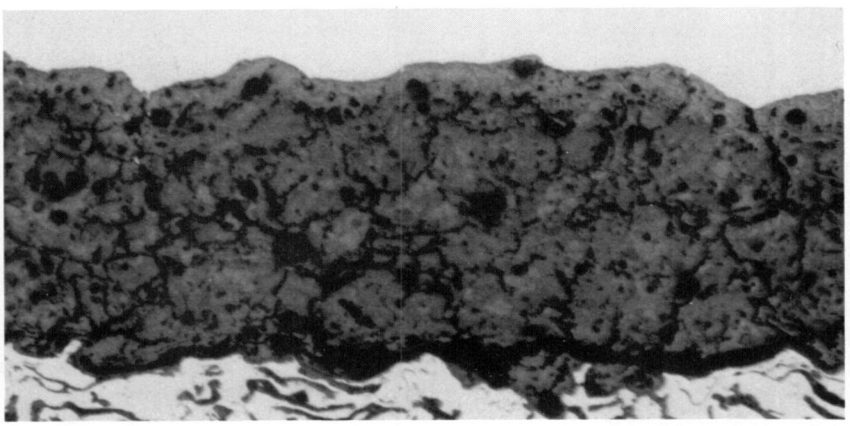

200X

b. POST-TEST LIGHT PHOTOMICROGRAPH. NOTE INCREASED MICROCRACKING COMPARED TO PRE-TEST STRUCTURE.

Figure 3-4 Microstructure of Task I Coating System 2 [21 w% MgO - ZrO_2 Plasma Sprayed with Uncontrolled Substrate Temperature] before and after 1690 Cycles of Burner Rig Exposure at 1107°C (2025°F)

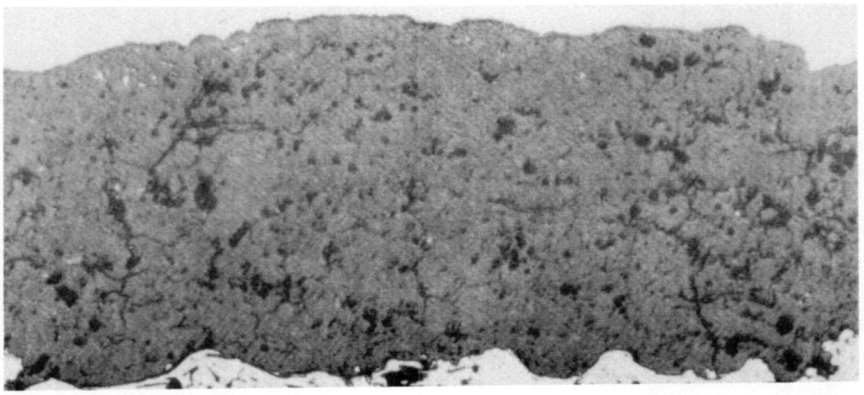

a. PRE-TEST LIGHT PHOTOMICROGRAPH 200X

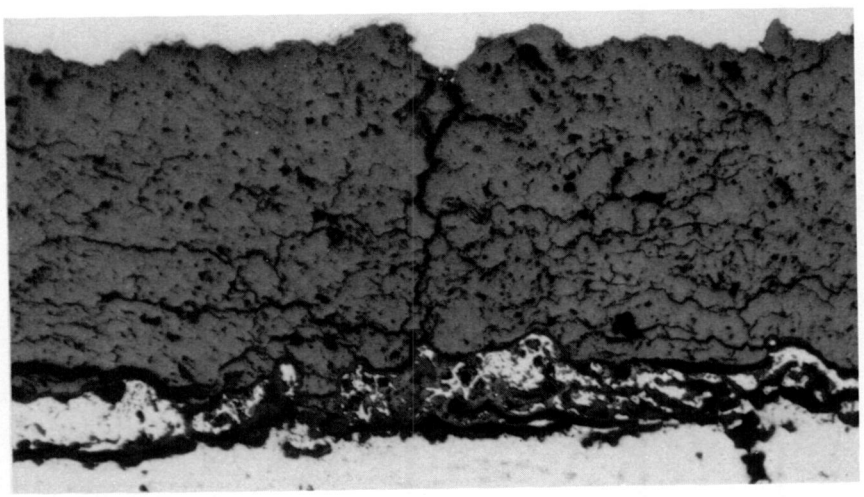

b. POST-TEST LIGHT PHOTOMICROGRAPH 150X

Figure 3-5 Microstructure of Task I Coating System 3 [6 w% Y_2O_3 - ZrO_2 Plasma Sprayed with 149°C (300°F) Substrate Temperature Control] before and after 4820 Cycles of Burner Rig Exposure at 1107°C (2025°F)

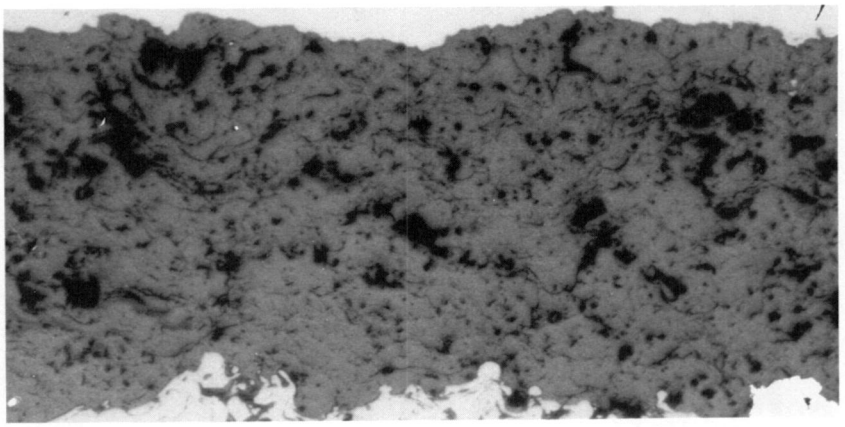

200X

a. PRE-TEST LIGHT PHOTOMICROGRAPH

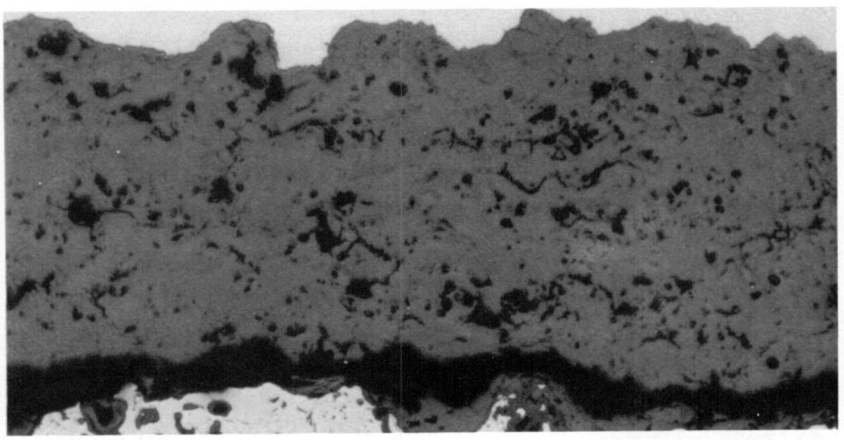

200X

b. POST-TEST LIGHT PHOTOMICROGRAPH. NOTE THE INCREASED CERAMIC DENSITY COMPARED TO PRE-TEST STRUCTURE.

Figure 3-6 Microstructure of Task I Coating System 4 [20 w% Y_2O_3 - ZrO_2 Plasma Sprayed with 149°C (300°F) Substrate Temperature Control] before and after 660 Cycles of Burner Rig Exposure at 1107°C (2025°F)

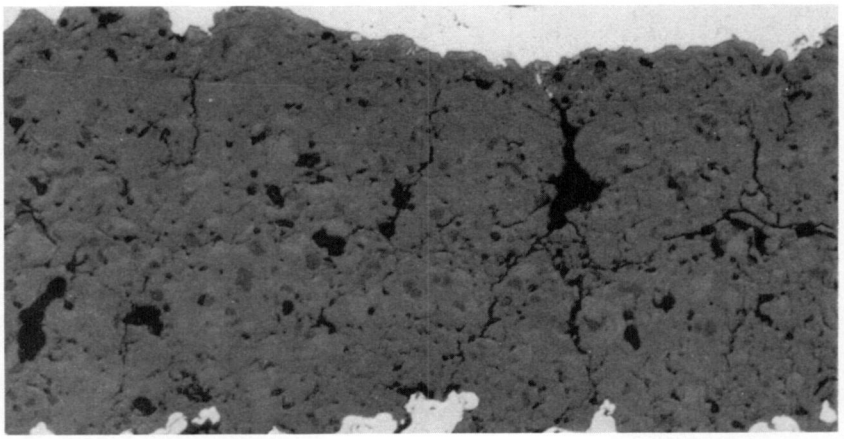

200X

a. PRE-TEST LIGHT PHOTOMICROGRAPH. NOTE EXTENSIVE MICROCRACKING WITH SAME TENDENCY FOR FORMATION OF INCIPIENT SEGMENTATION CRACKING.

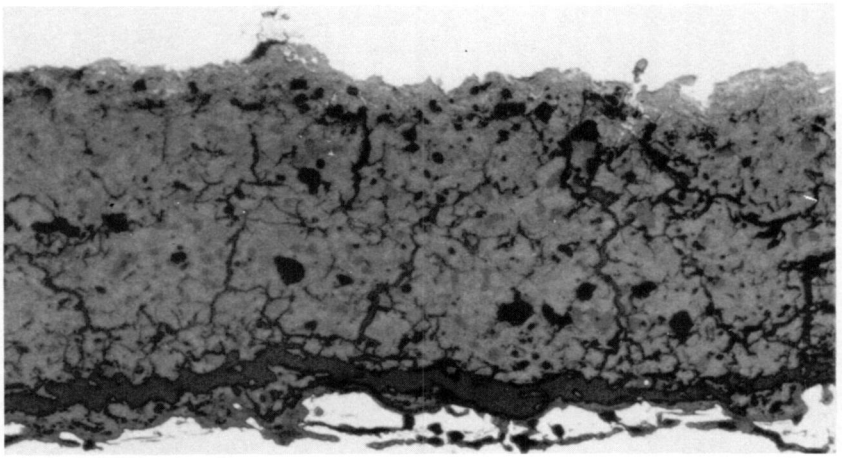

200X

b. POST-TEST LIGHT PHOTOMICROGRAPH. NOTE INCREASED MICROCRACKING COMPARED TO PRE-TEST STRUCTURE.

Figure 3-7 Microstructure of Task I Coating System 5 [21 w% MgO - ZrO_2 Plasma Sprayed with 149°C (300°F) Substrate Temperature Control] before and after 1480 Cycles of Burner Rig Exposure at 1107°C (2025°F)

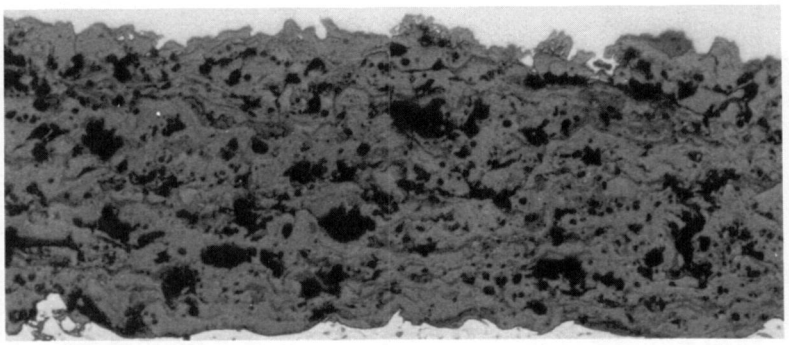

a. PRE-TEST LIGHT PHOTOMICROGRAPH 200X

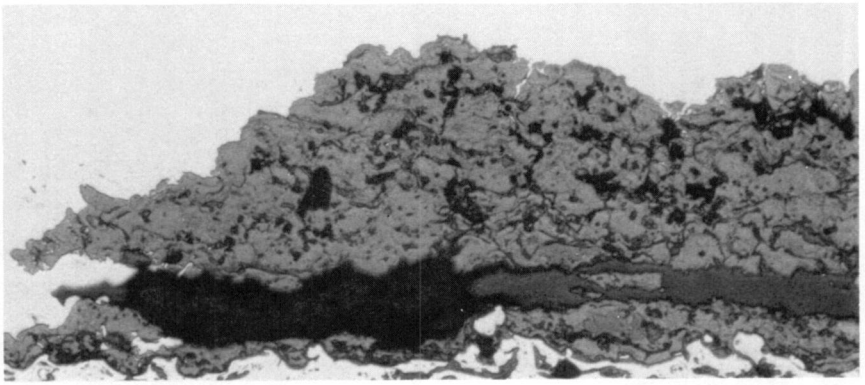

150X

b. POST-TEST LIGHT PHOTOMICROGRAPH. NOTE INCREASED "STRUCTURAL DEGRADATION" COMPARED TO PRE-TEST STRUCTURE.

Figure 3-8 Microstructure of Task I Coating System 6 [85 w% (20 w% Y_2O_3 - ZrO_2) + 15 w% Al_2O_3 Plasma Sprayed with 149°C (300°F) Substrate Temperature Control] before and after 390 Cycles of Burner Rig Exposure at 1107°C (2025°F)

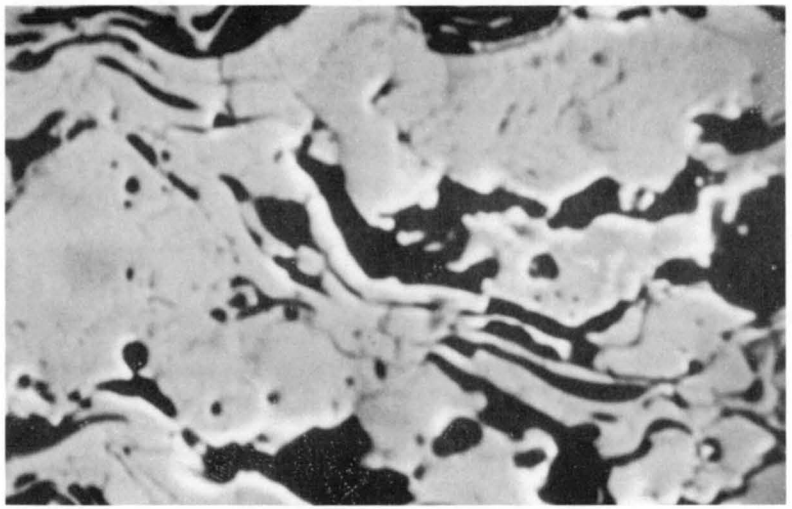

c. BACKSCATTERED ELECTRON IMAGE 1000X

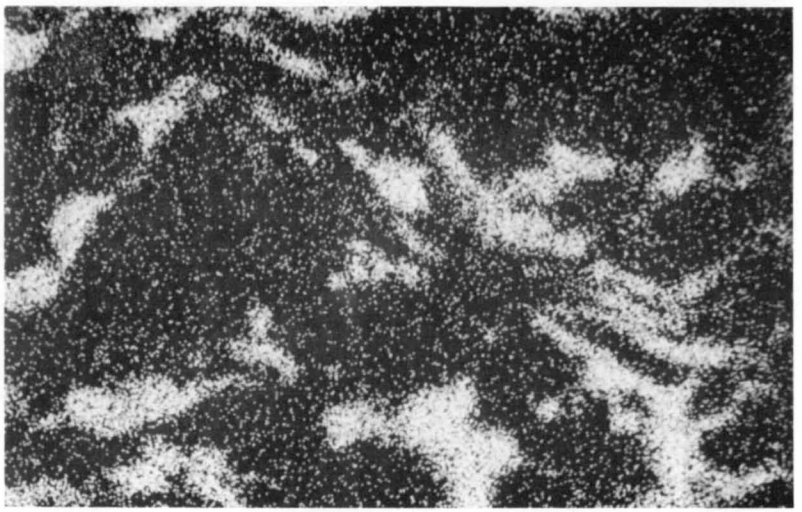

d. ALUMINUM X-RAY IMAGE 1000X

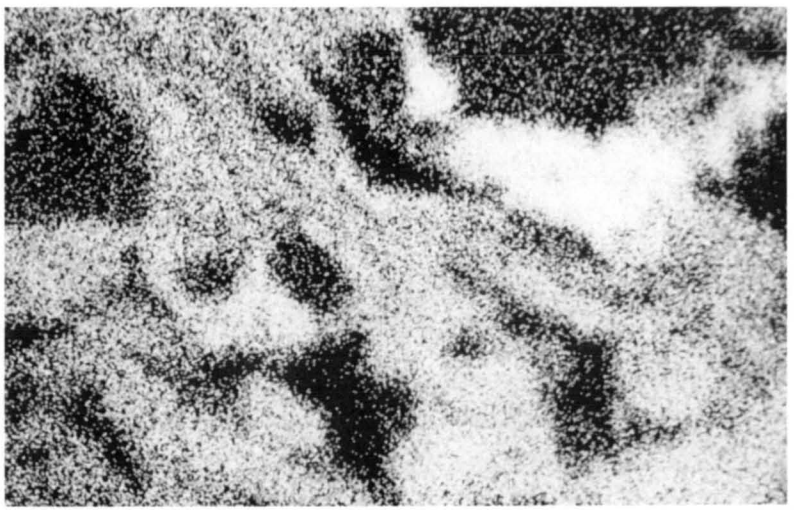

e. YTTRIUM X-RAY IMAGE 1000X

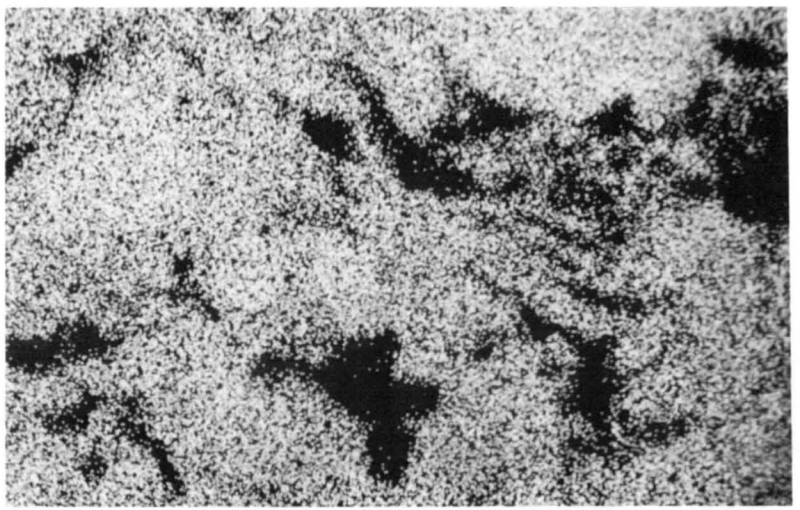

f. ZIRCONIUM X-RAY IMAGE 1000X

Figure 3-8 (Continued) Backscattered Electron Image Photograph and X-ray Image Photographs Showing Pre-Test Elemental Distributions in Task I Coating System 6 [85 w% (20 w% Y_2O_3 - ZrO_2) + 15 w% Al_2O_3]

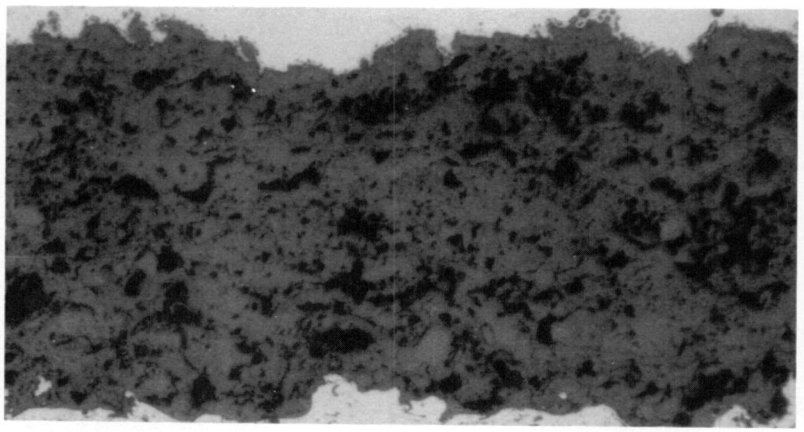

a. PRE-TEST LIGHT PHOTOMICROGRAPH 200X

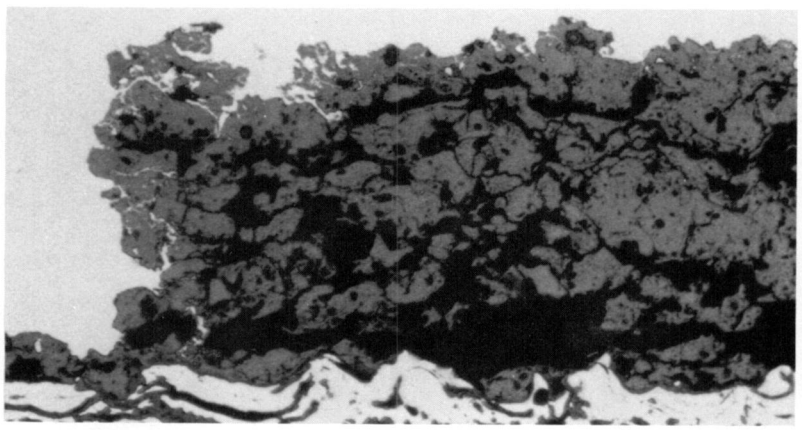

200X

b. POST-TEST LIGHT PHOTOMICROGRAPH. NOTE INCREASED "STRUCTURAL DEGRADATION" COMPARED TO PRE-TEST STRUCTURE.

Figure 3-9 Microstructure of Task I Coating System 7 [85 w% (20 w% Y_2O_3 - ZrO_2) + 15 w% MgO Plasma Sprayed with 149°C (300°F) Substrate Temperature Control] before and after 190 Cycles of Burner Rig Exposure at 1107°C (2025°F)

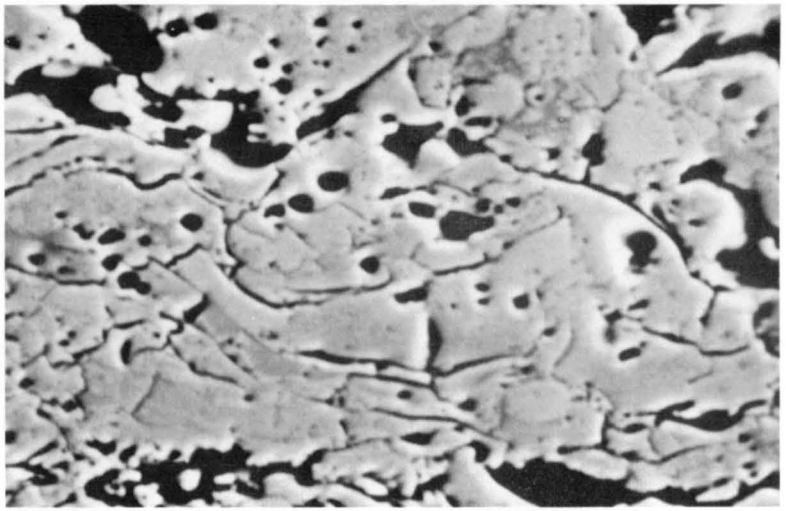

c. BACKSCATTERED ELECTRON IMAGE 1000X

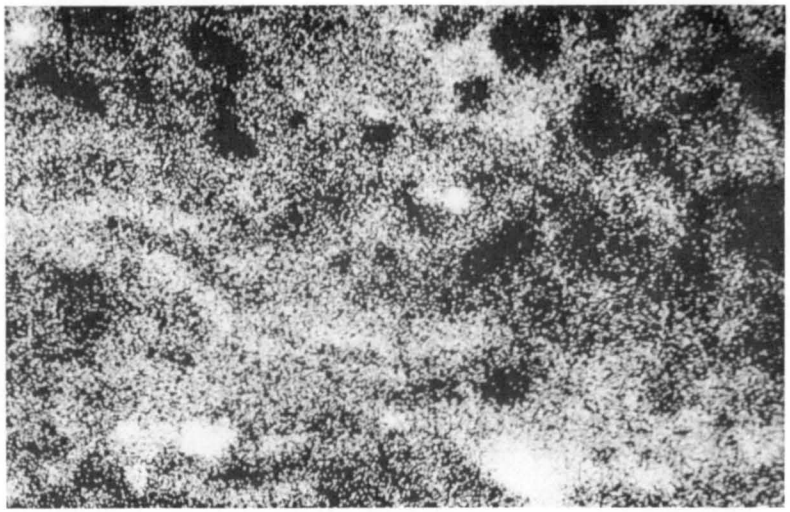

d. MAGNESIUM X-RAY IMAGE 1000X

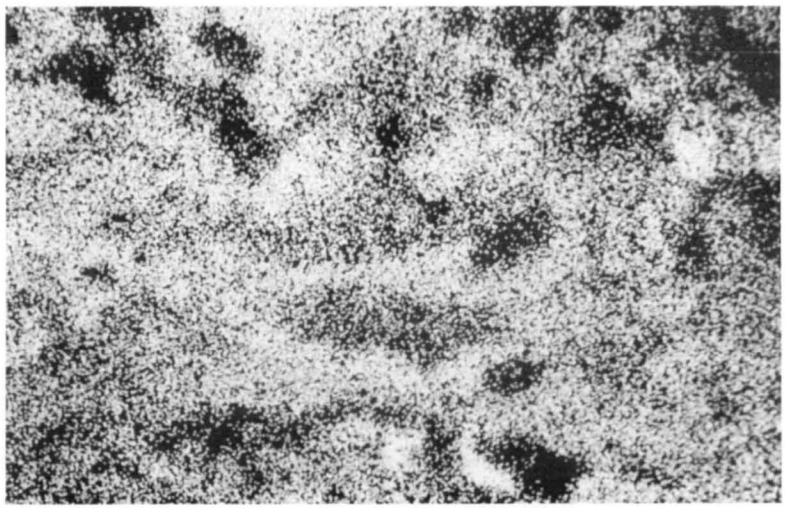

e. YTTRIUM X-RAY IMAGE 1000X

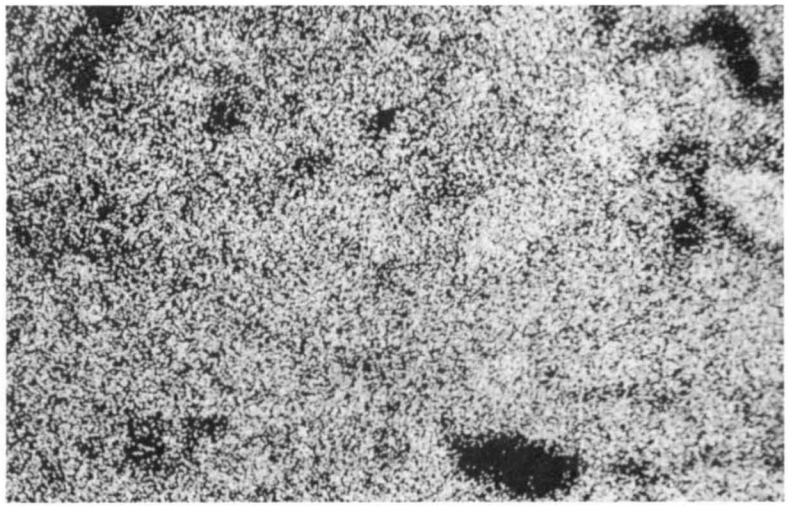

f. ZIRCONIUM X-RAY IMAGE 1000X

Figure 3-9 (Continued) Backscattered Electron Image Photograph and X-ray Image Photographs Showing Pre-Test Elemental Distributions in Task I Coating System 7 [85 w% (20 w% Y_2O_3 - ZrO_2) + 15 w% MgO]

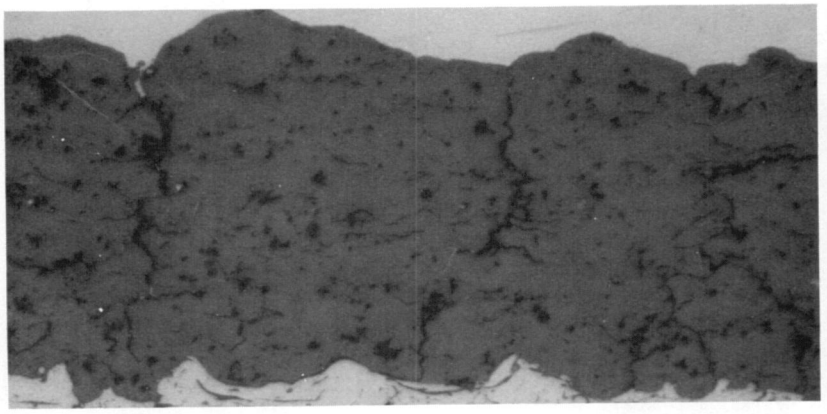

200X

a. PRE-TEST LIGHT PHOTOMICROGRAPH

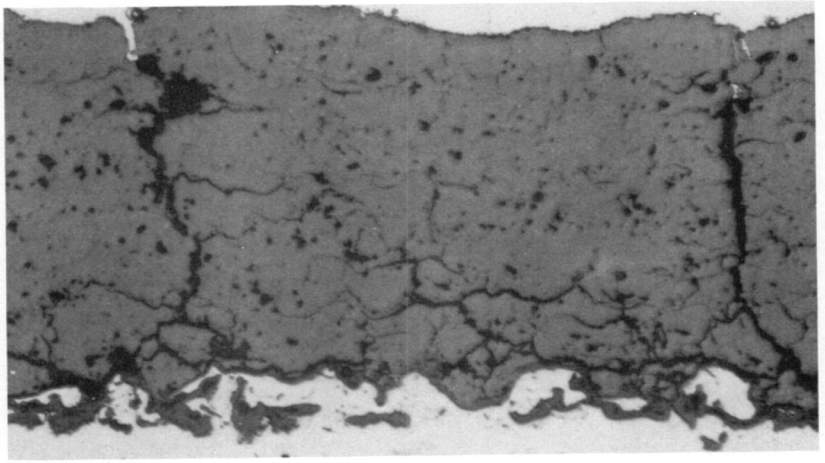

200X

b. POST-TEST LIGHT PHOTOMICROGRAPH

Figure 3-10 Microstructure of Task I Coating System 8 [6 w% Y_2O_3 - ZrO_2, 1 inch Gun-to-Specimen Distance, Plasma Sprayed with 149°C (300°F) Substrate Temperature Control] before and after 2470 Cycles of Burner Rig Exposure at 1107°C (2025°F)

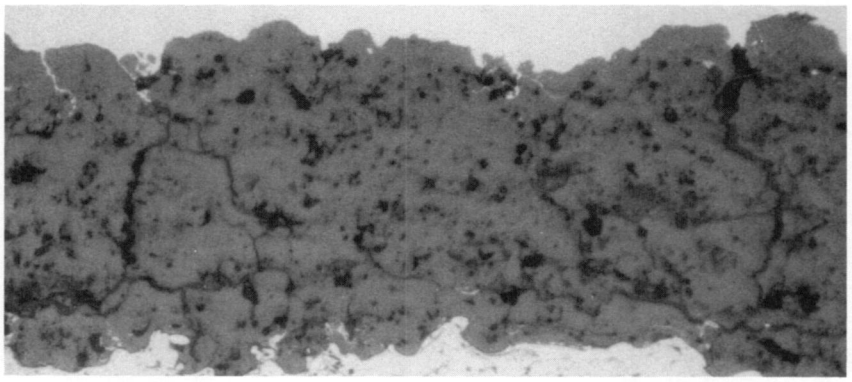

150X

a. PRE-TEST LIGHT PHOTOMICROGRAPH. NOTE SIGNIFICANT CRACKING IN THE PLANE OF THE COATING CAUSED BY HIGH ENERGY DEPOSITION.

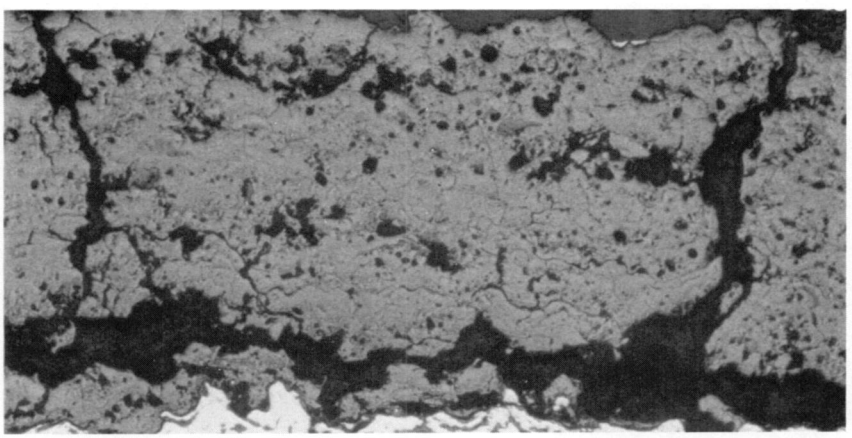

150X

b. POST-TEST LIGHT PHOTOMICROGRAPH. NOTE THE ABSENCE OF SIGNIFICANT SINTERING, WHICH IS ATTRIBUTED TO REDUCED EXPOSURE TIME COMPARED TO SYSTEMS 4, 14 and 15.

Figure 3-11 Microstructure of Task I Coating System 9 [20 w% Y_2O_3 - ZrO_2), 1 inch Gun-to-Specimen Distance, Plasma Sprayed with 149°C (300°F) Substrate Temperature Control] before and after 350 Cycles of Burner Rig Exposure at 1107°C (2025°F)

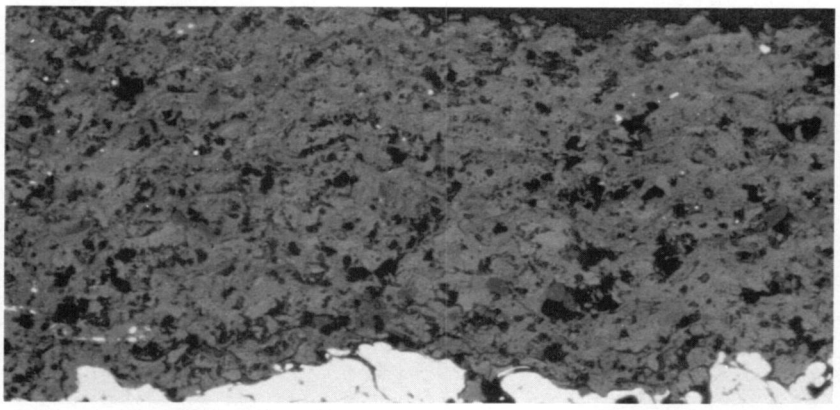

200X

a. PRE-TEST PHOTOMICROGRAPH. NOTE EXTENSIVE MICROCRACKING.

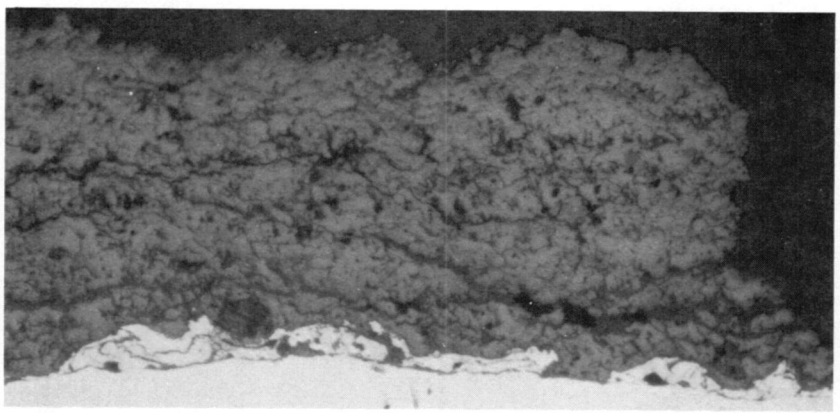

150X

b. POST-TEST LIGHT PHOTOMICROGRAPH. NOTE INCREASED MICROCRACKING COMPARED TO PRE-TEST STRUCTURE.

Figure 3-12 Microstructure of Task I Coating System 10 [20 w% MgO - ZrO_2, Plasma Sprayed with High Energy Gun and 149°C (300°F) Substrate Temperature Control] before and after 1060 Cycles of Burner Rig Exposure at 1107°C (2025°F)

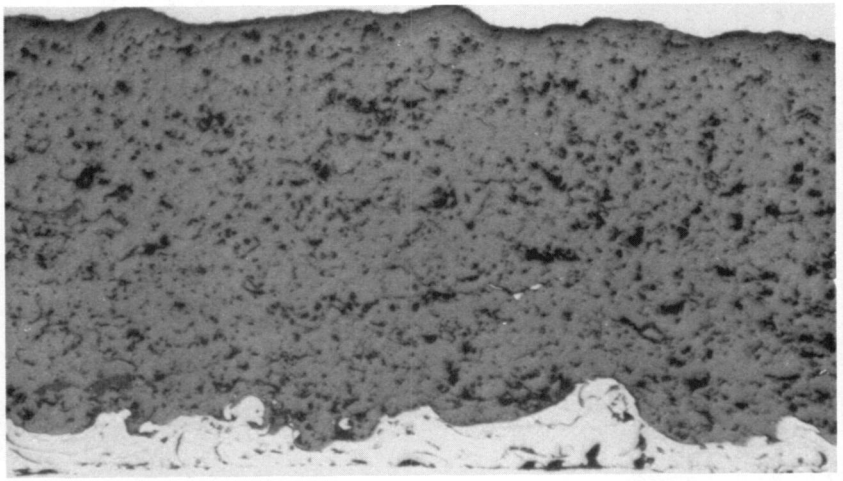

200X

a. PRE-TEST LIGHT PHOTOMICROGRAPH

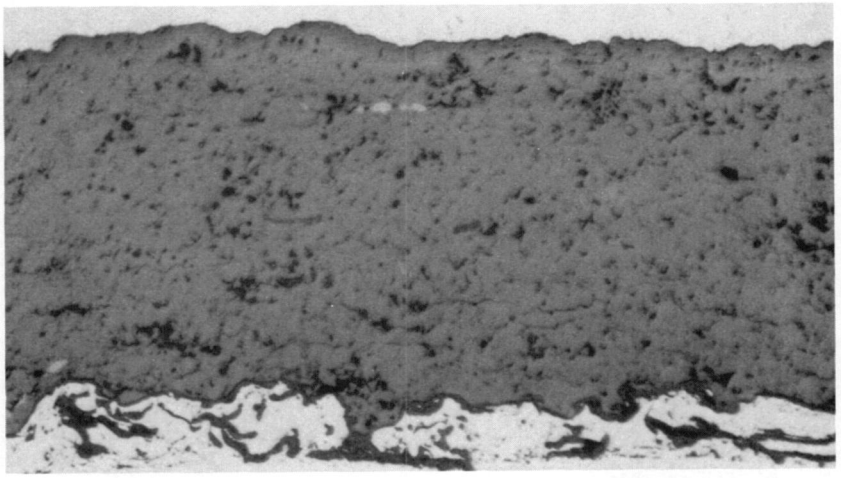

200X

b. POST-TEST LIGHT PHOTOMICROGRAPH

Figure 3-13 Microstructure of Task I Coating System 11 [8 w% Y_2O_3 - ZrO_2, Plasma Sprayed with High Energy Gun and 149°C (300°F) Substrate Temperature Control] before and after 6110 Cycles of Burner Rig Exposure at 1107°C (2025°F)

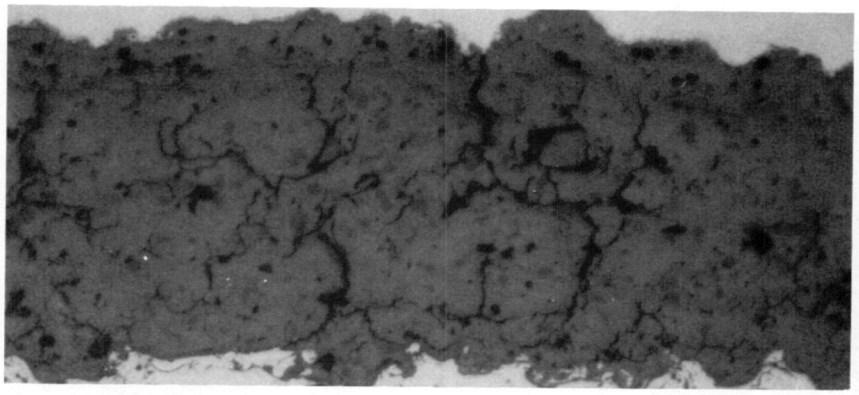

200X

a. PRE-TEST LIGHT PHOTOMICROGRAPH. NOTE EXTENSIVE MICROCRACKING.

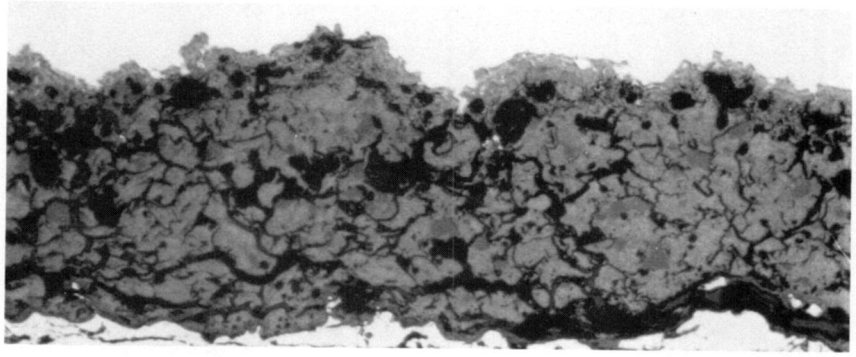

200X

b. POST-TEST LIGHT PHOTOMICROGRAPH. NOTE INCREASED MICROCRACKING COMPARED TO PRE-TEST STRUCTURE.

Figure 3-14 Microstructure of Task I Coating System 12 [21 w% MgO - ZrO_2, Plasma Sprayed with 149°C (300°F) Substrate Temperature Control and Liquid Tin Quenched from 1079°C (1975°F)] before and after 1280 Cycles of Burner Rig Exposure at 1107°C (2025°F)

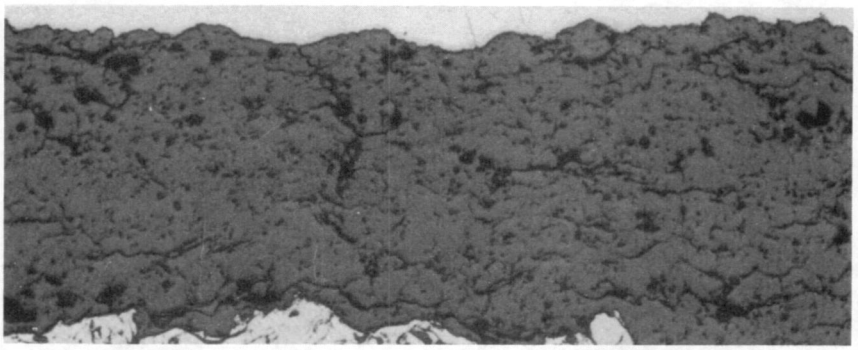

200X

a. PRE-TEST LIGHT PHOTOMICROGRAPH

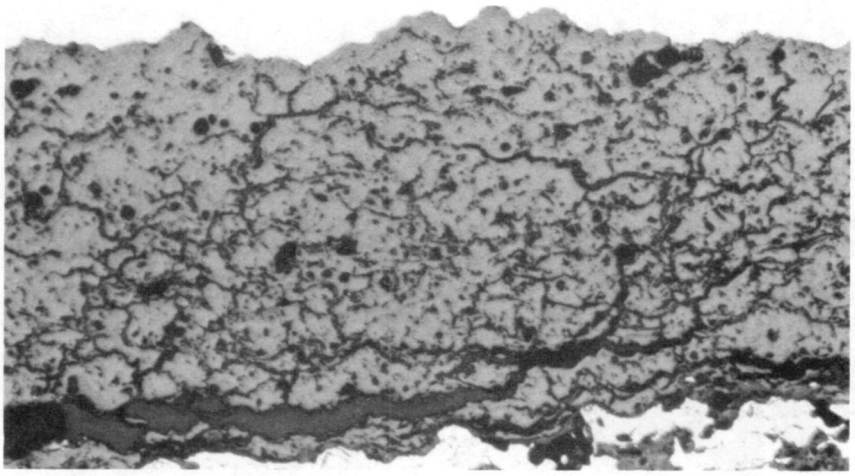

200X

b. POST-TEST LIGHT PHOTOMICROGRAPH

Figure 3-15 Microstructure of Task I Coating System 13 [6 w% Y_2O_3 - ZrO_2, Plasma Sprayed with 149°C (300°F) Substrate Temperature Control and Liquid Tin Quenched from 1079°C (1975°F)] before and after 4820 Cycles of Burner Rig Exposure at 1107°C (2025°F)

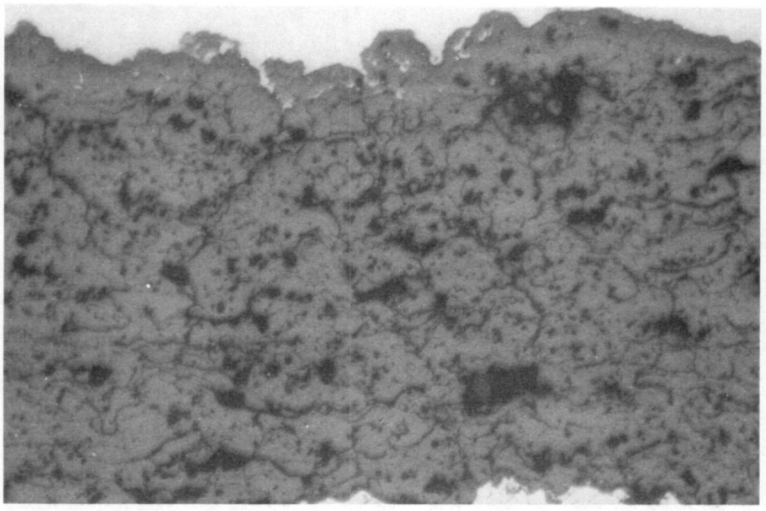

200X

a. PRE-TEST LIGHT PHOTOMICROGRAPH. NOTE INCREASED MICROCRACKING COMPARED TO SYSTEM 4.

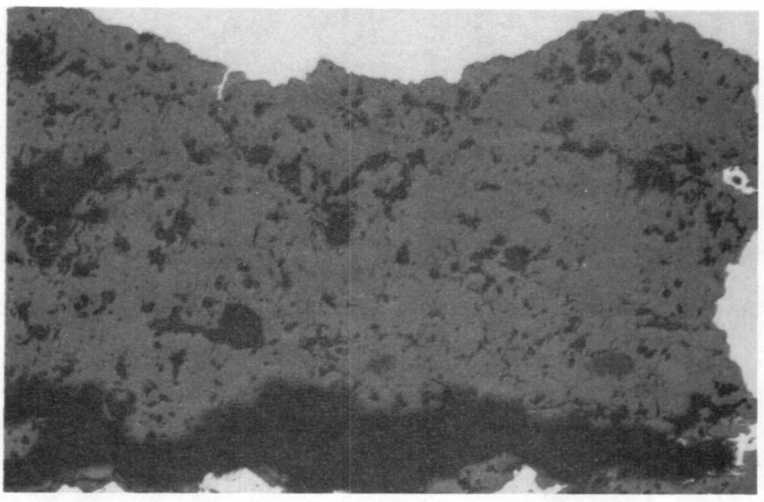

200X

b. POST-TEST LIGHT PHOTOMICROGRAPH. NOTE INCREASED DENSITY COMPARED TO PRE-TEST STRUCTURE.

Figure 3-16 Microstructure of Task I Coating System 14 [20 w% Y_2O_3 - ZrO_2, Plasma Sprayed with 149°C (300°F) Substrate Temperature Control and Liquid Tin Quenched from 1079°C (1975°F)] before and after 1060 Cycles of Burner Rig Exposure at 1107°C (2025°F)

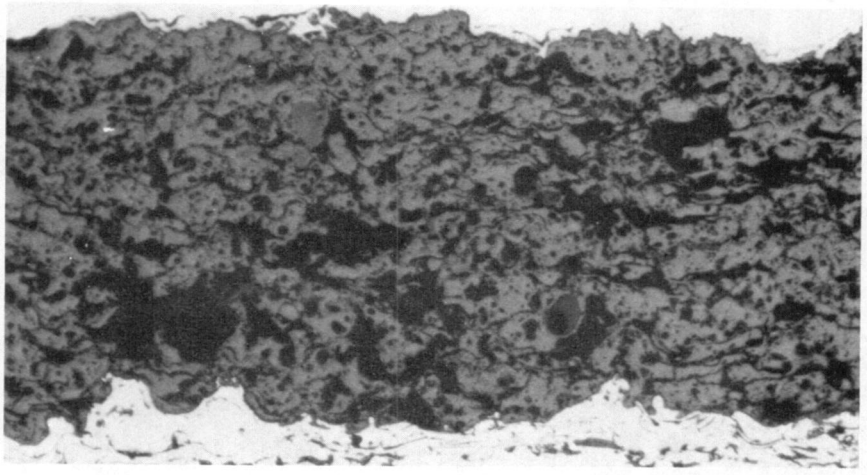

a. PRE-TEST LIGHT PHOTOMICROGRAPH 200X

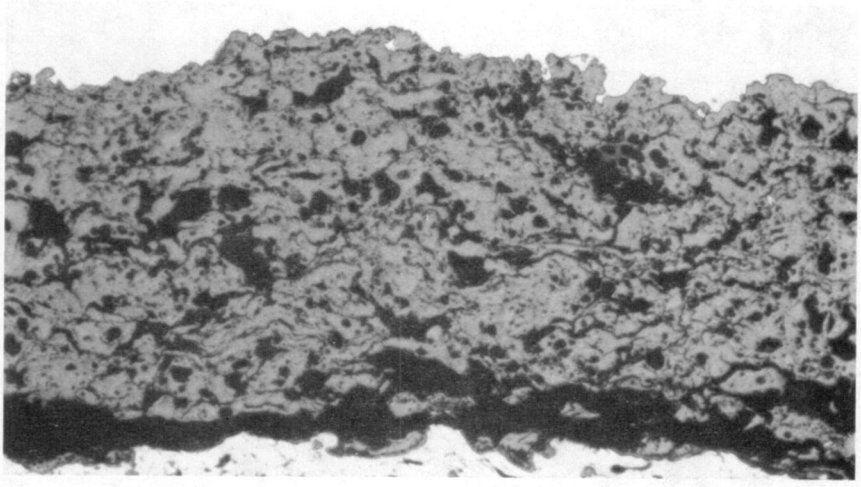

b. POST-TEST LIGHT PHOTOMICROGRAPH 200X

Figure 3-17 Microstructure of Task I Coating System 15 [85 w% (20 w% Y_2O_3 - ZrO_2) + 15 w% Carbon, Plasma Sprayed with 149°C (300°F) Substrate Temperature Control] before and after 620 Cycles of Burner Rig Exposure at 1107°C (2025°F)

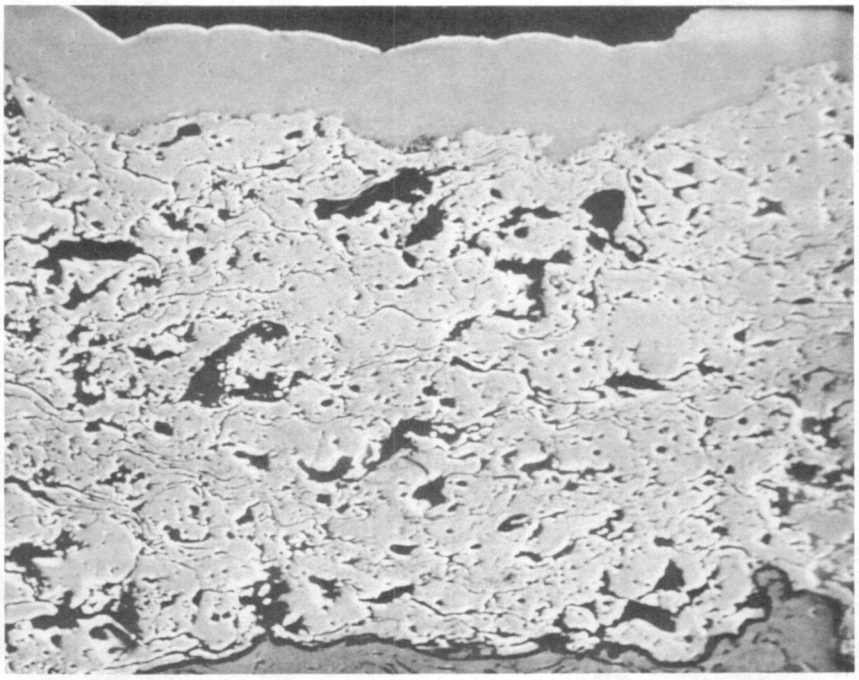

c. 300X

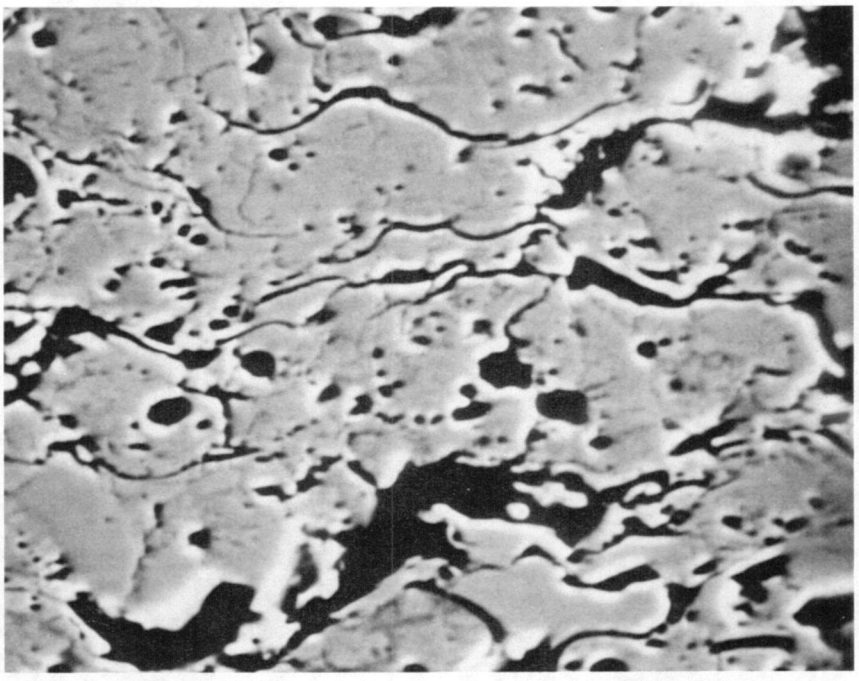

d. 1000X

Figure 3-17 (Continued) Backscattered Electron Image Photographs Showing Pre-Test Task I Coating System 15 [85 w% (20 w% Y_2O_3 - ZrO_2) + 15 w% Carbon]

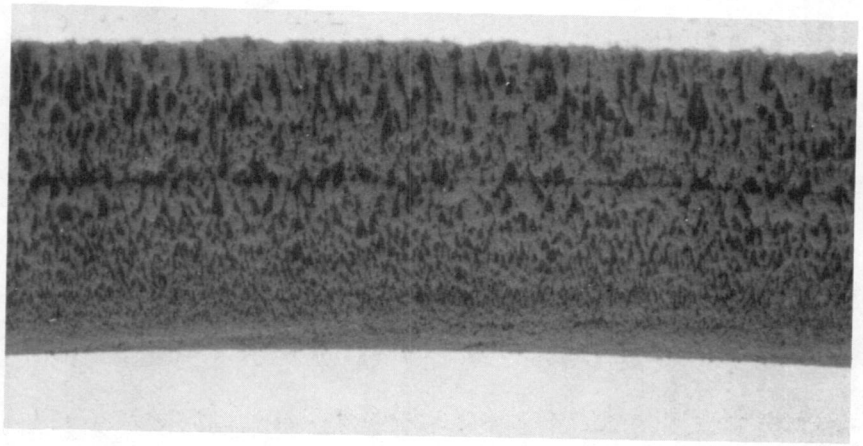

a. PRE-TEST LIGHT PHOTOMICROGRAPH 200X

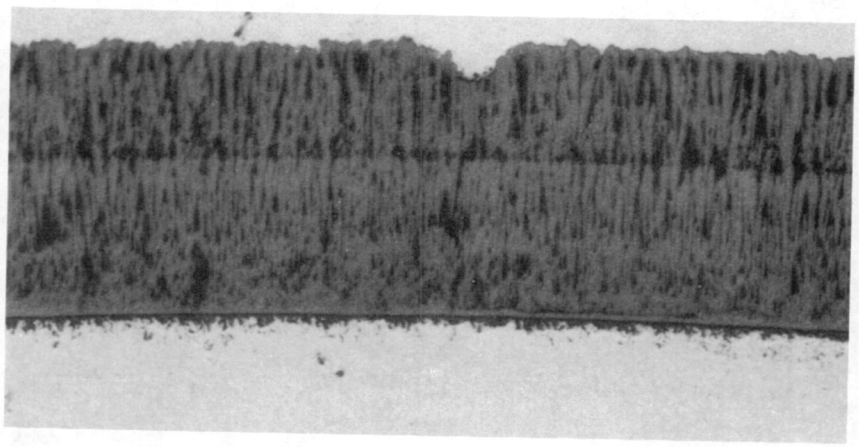

b. POST-TEST LIGHT PHOTOMICROGRAPH 200X

Figure 3-18 Microstructure of Task I Coating System 16 [EB-PVD 20 w% Y_2O_3 - ZrO_2] before and after 6200 Cycles of Burner Rig Exposure at 1107°C (2025°F)

free Al_2O_3 (Figure 3-8d). These maps also suggest some heterogeneity of Y distribution in the coating (Figure 3-8e). Similar examination of the MgO doped Y_2O_3 stabilized ZrO_2 coating (Figure 3-9d through f) suggests a substantially smaller content of free MgO than the amount of free Al_2O_3 seen in the Al_2O_3 doped ceramic of the same composition. There also appears to be significant amounts of MgO in solution in the Y_2O_3 stabilized ZrO_2 matrix. This observation is consistent with the previously described x-ray results (Table 3-III), which suggested that Y_2O_3 significantly alters the solubility of ZrO_2 for MgO. Scanning electron micrography of the carbon doped coating (Figure 3-17c and d) confirms the presence of significant amounts of porosity created presumably by conversion of carbon to volatile oxides during pre-test thermal exposure in air.

3.3 TASK I BURNER RIG EVALUATION

To evaluate the relative thermal spall resistance of the candidate coatings, triplicate specimens coated with each of the systems listed in Table 3-I were cyclic burner rig tested at 1107°C (2025°F) maximum leading edge temperature as described in Appendix A.

Failure was defined as spalling of the ceramic layer over approximately 50% of the specimen test section, which constitutes about the middle 2.5 cm (1 inch) of the hottest side of the bar. This failure criterion recognizes that some ceramic loss may occur without severe degradation of the protective nature of the ceramic. It should be noted that, once initiated, spallation failure propagates relatively rapidly, so that the stated coating life is not highly sensitive to end point definitions. A typical failed specimen is shown in Figure 3-19. Coatings which had not failed after 6000 cycles of exposure were removed from the test.

Results of the burner rig tests are listed in Table 3-IV and presented graphically in Figure 3-20. Coatings which clearly show improvement compared to the baseline include systems 3, 8, 11, 13, and 16. With the exception of system 16, which has a unique structure produced by the vapor deposition process, the best performing coatings were all partially stabilized zirconia containing either 6 or 8 w% Y_2O_3. Performance of the 21 w% MgO - ZrO_2 modification tended to be comparable to the baseline, regardless of processing. With the exception of the EB-PVD results, performance of the 20 w% Y_2O_3 "fully stabilized" ZrO_2 tended to be poor, regardless of processing or compositional modifications.

3.4 EVALUATION OF TESTED SPECIMENS

To provide additional understanding of coating behavior, burner rig tested specimens were evaluated metallographically and by x-ray diffraction. Exposed specimens were sectioned through the hot zone for metallographic evaluation. X ray diffraction patterns were obtained from remnant ceramic in the hot zone area. Light micrographs of exposed ceramic structures are included in Figures 3-3 through 3-18. Post-test x-ray diffraction results are listed together with pre-test results in Table 3-III.

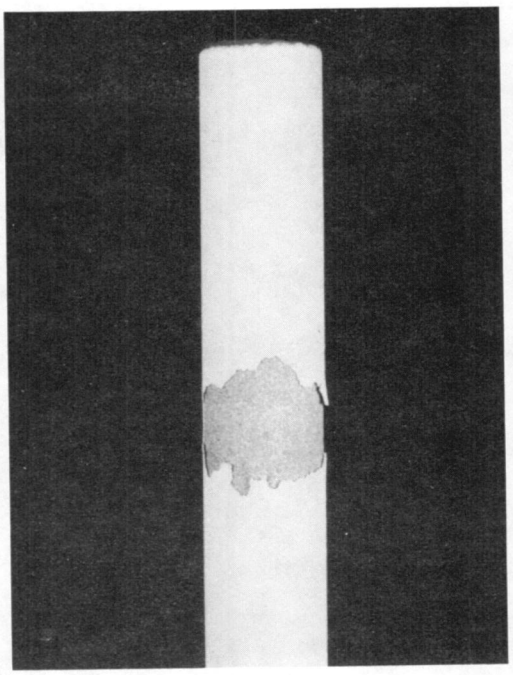

a. 1X

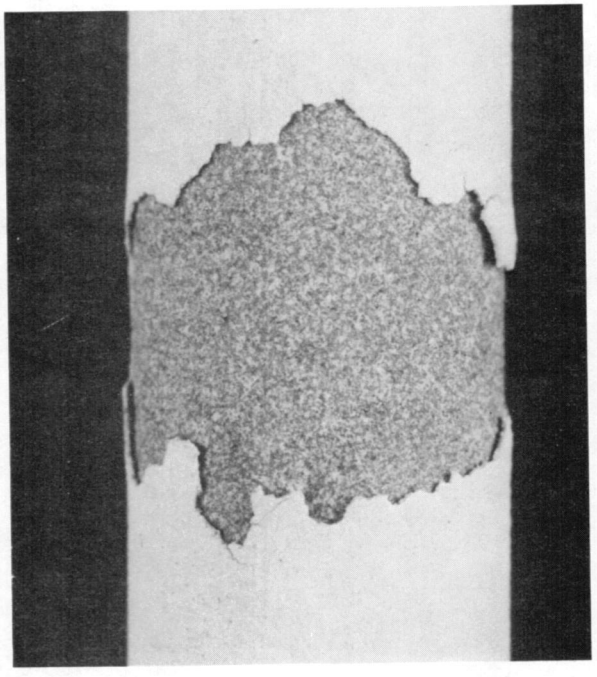

b. 4X

Figure 3-19 Typical Ceramic Spallation Failure of 21 w% MgO - ZrO_2 Coated Specimen [149°C (300°F) Substrate Temperature Control, Tin Quench, System 12] following 1280 Cycles of Test Exposure. Note remnant ceramic in spalled area.

TABLE 3-IV

TASK I CYCLIC THERMAL TEST RESULTS

Coating System Number	Ceramic Layer	Substrate Temperature During Coating °C (°F)	Post Coating Processing	Cycles to Ceramic Failure			
				Bar 1	Bar 2	Bar 3	Avg.
1	8 w% Y_2O_3 - ZrO_2	Uncontrolled	1079°C (1975°F)/ 4 hrs/H_2	1770	1820	2770	2120
2	21 w% MgO - ZrO_2	Uncontrolled	None	1480	1500	1690	1557
3	6 w% Y_2O_3 - ZrO_2	149 (300)	1079°C (1975°F)/ 4 hrs/H_2	1600(2)	4820	5830	5325(3)
4	20 w% Y_2O_3 - ZrO_2	149 (300)	1079°C (1975°F)/ 4 hrs/H_2	340	660	1590	863
5	21 w% MgO - ZrO_2	149 (300)	None	700(2)	1480	1690	1585(3)
6	85 w% (20 w% YSZ) +(1) 15 w% Al_2O_3	149 (300)	1079°C (1975°F)/ 4 hrs/H_2	190	390	620	400
7	85 w% (20 w% YSZ) + 15 w% MgO	149 (300)	1079°C (1975°F)/ 4 hrs/H_2	160	190	190	180
8	6 w% Y_2O_3 - ZrO_2 (2.5 cm (1 inch) gun distance)	149 (300)	1079°C (1975°F)/ 4 hrs/H_2	2430	2470	3510	2803
9	20 w% Y_2O_3 - ZrO_2 (2.5 cm (1 inch) gun distance)	149 (300)	1079°C (1975°F)/ 4 hrs/H_2	340	350	660	450
10	21 w% MgO - ZrO_2 (High energy gun)	149 (300)	None	1060	1060	1930	1350
11	8 w% Y_2O_3 - ZrO_2 (High energy gun)	149 (300)	1079°C (1975°F)/ 4 hrs/H_2	6110 NF(5)	6110 NF	6110 NF	More than 6110
12	21 w% MgO - ZrO_2	149 (300)	221°C (430°F) Liquid Tin Quench from 1079°C (1975°F)/Air	680	840(2)	1280	980(3)
13	6 w% Y_2O_3 - ZrO_2	149 (300)	221°C (430°F) Liquid Tin Quench from 1079°C (1975°F)/Air	1430(2)	4820	6030 NF	5425(3)
14	20 w% Y_2O_3 - ZrO_2	149 (300)	221°C (430°F) Liquid Tin Quench from 1079°C (1975°F)/Air	610	1020	1060	897
15	20 w% Y_2O_3 - ZrO_2 + carbon	149 (300)	1079°C (1975°F)/ 4 hrs/Air	610	620	1260	830
16	20 w% Y_2O_3 - ZrO_2 (EB-PVD)	-	1079°C (1975°F)/ 4 hrs/H_2	(4)	6200 NF	6200 NF	More than(3) 6200 NF

(1) YSZ = Yttria stabilized zirconia
(2) Metallic defect failure
(3) Average of only two data points
(4) Burner rig malfunction
(5) NF = No failure

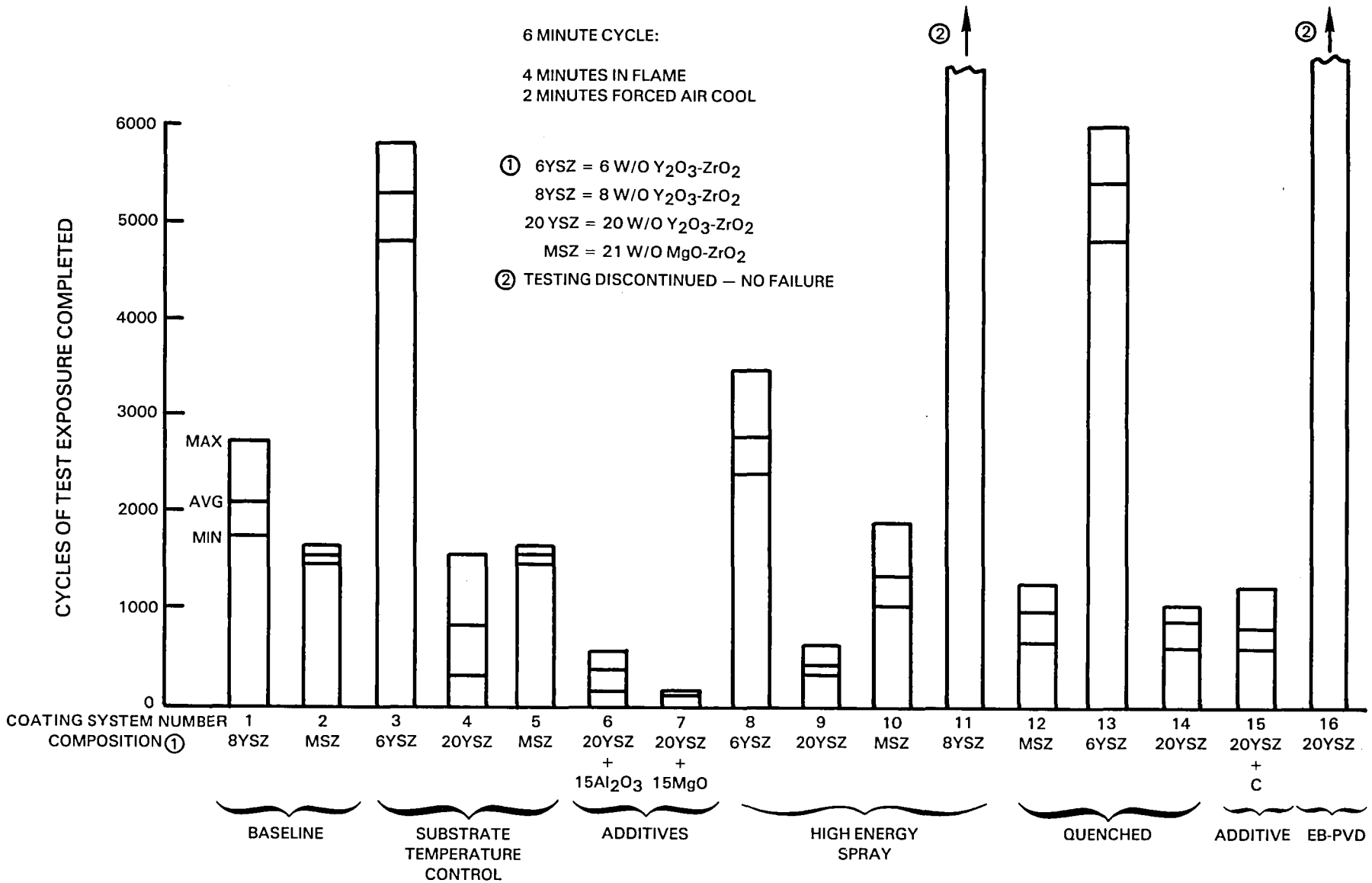

Figure 3-20 Thermal Cycle Test Exposure of Experimental Thermal Barrier Coatings at 1107°C (2025°F)

Visual and metallographic observation indicated that the predominant ceramic failure mode involved the formation and propagation of a dominant crack within the ceramic parallel to the metal-ceramic interface, as shown in Figure 3-3b. As shown in Figure 3-4b, cracking sometimes occurs at the interface between the ceramic and the oxide scale formed on the surface of the metallic coating layer; more often, however, a thin layer of remnant ceramic is left adhering to the metal after ceramic spallation. This layer is clearly observable on the failed specimen shown in Figure 3-19.

The relative performance of the various coating systems may, to some extent, be rationalized by comparison of the pre- and post-test structures and phase distributions. All of the magnesia stabilized ceramic coatings (systems 2, 5, 10, and 12), for example, exhibit a significant increase in the extent of microcracking as a result of cyclic thermal exposure (Figures 3-4, 7, 12, and 14). Examination of the pre- and post-test x-ray diffraction results for these coating systems (Table 3-III) suggests that this increased microcracking results from a progressive de-stabilization of the higher temperature phases, with an attendant increase in the volume fraction of monoclinic phase (45 to 60%) when measured at room temperature. This phase is thought to undergo a reversible transformation to tetragonal during each thermal cycle, which results in the development of large internal stresses caused by the large difference in density between these two phases. These cyclically reversed internal volume changes cause progressively increasing amounts of internal cracking, leading eventually to destruction of coating integrity.

As opposed to the 21 w% $MgO - ZrO_2$ composition discussed above, phase distribution in the 20 w% $Y_2O_3 - ZrO_2$ composition appears to be quite stable during cyclic thermal exposure. As noted previously, this composition deposits as virtually all cubic with only trace amounts (less than 5%) of monoclinic phase, and shows essentially no change after testing. The only significant change seen is in system 6, where the amount of free Al_2O_3 decreased from 8% to 1%. This result suggests there may be some solubility of Al_2O_3 in ZrO_2 at the 1107°C (2025°F) exposure temperature.
Microstructurally, undiluted plasma sprayed 20 w% $Y_2O_3 - ZrO_2$ systems 4 and 14, which are identical except for the enhanced microcracking produced by quenching of system 14, both exhibited a substantial reduction of the amount of strain tolerant features present in the microstructure after testing. This increase of post-test density indicates that sintering of the ceramic may be occurring during thermal exposure. This reduction of strain tolerance during exposure is thought to be responsible for the relatively poor cyclic thermal performance of the plasma deposited 20 w% $Y_2O_3 - ZrO_2$ composition. The carbon diluted 20 w% $Y_2O_3 - ZrO_2$ ceramic (system 15) exhibits a similar, though less pronounced, densification after exposure. The average performance of this system was virtually identical to that of systems 4 and 14 (Table 3-IV).

The high energy deposited 20 w% $Y_2O_3 - ZrO_2$ coating (system 9) exhibited significant cracking in the plane of the coating (Figure 3-11a). Rapid propagation of these in-plane cracks is presumed to be responsible for the poor performance of this coating. This coating did not exhibit sintering to the same degree as systems 4, 14, and 15. This reduced sintering is attributed to the lower average exposure time of the system 9 specimens.

Both of the 20% Y_2O_3 - ZrO_2 coatings which were modified by the inclusion of a second phase having a different coefficient of thermal expansion (systems 6 and 7) performed very poorly in cyclic burner rig testing. As opposed to the undiluted systems of the same composition discussed above, both of these systems exhibited moderate to substantial increases of microcracking as a result of exposure. This presumably is the result of the cyclic differential expansion and contraction of the innoculant relative to the ZrO_2 matrix. This observation suggests that these coatings progressively self-destruct in the same way as the 21 w% MgO - ZrO_2 ceramic discussed previously.

The partially stabilized zirconias (systems 1, 3, 8, 11, and 13) appear to be relatively stable both structurally (Figures 3-3, 5, 10, 13, and 15) and with respect to conversion to monoclinic phase (Table 3-III). The primary structural change observed as a result of cyclic thermal exposure of these coatings is a slight increase in the percentage of the tetragonal phase. In the case of the high energy gun coating (system 11), which deposits as 100% cubic, this change was substantial, with 75% conversion from cubic to tetragonal after testing. The poorest performing of the five partially stabilized zirconia coatings was the baseline (system 1), which did not have the benefit of residual stress (substrate temperature) control during deposition. The best performing is system 11, which appears to have a slightly higher level of porosity and less microcracking than the other three partially stabilized zirconia systems which were sprayed with controlled residual stress processing. The relatively lower performance of the high energy system 8 (sprayed from a 1 inch distance) is attributed to incipient in-plane cracking similar to that which occurred in the companion system 9. Taken as a group, the performance of the partially stabilized zirconia compositions clearly is superior to the other two compositions evaluated (except for the EB-PVD coating described below).

The structure and phase distribution observed in the EB-PVD 20 w% Y_2O_3 - ZrO_2 remained essentially unchanged after 6000 cycles of thermal exposure (Figure 3-18). This high level of structural stability, coupled with the extremely high level of strain tolerance inherent to the columnar PVD structure, is presumed to be responsible for the excellent performance of this coating.

3.5 SELECTION OF TASK II CANDIDATES

Based on the clearly superior performance in the Task I burner rig evaluations, plasma sprayed, partially stabilized zirconia (6 w% Y_2O_3 - ZrO_2) was selected for three of the four coatings to be optimized in Task II. Specific plasma spray processes selected for optimization were the controlled substrate temperature plasma spray process (system 3), the high energy input plasma spray process (systems 8 and 11), and post coat thermal shock (system 13). The fourth system selected was the EB-PVD deposition process (system 16), which also performed extremely well in Task I. Efforts to optimize each of these four coating systems are described in the following section.

4.0 TASK II - COATING/PROCESS IMPROVEMENTS

The objectives of this task were to optimize each of the four coating systems selected in Task I and to evaluate these systems for selection of four Task III candidates. Methods of coating, testing, and evaluation were identical to those employed in Task I (Section 3.0).

4.1 SELECTION OF APPROACHES TO SYSTEM OPTIMIZATION

For each of the four coating concepts selected in Task I, four process or chemistry modifications were identified to provide increased durability or producibility. These approaches are listed in Table 4-I and are described in the following paragraphs.

Modifications to system 3 involved evaluation of different powder particle sizes and morphologies and of post-coat surface finishing. Three starting ceramic powder size/shape variables were utilized to investigate effects on coating structure, life, and producibility. A fourth condition investigated the effect of media surface finishing on ceramic spalling resistance. This latter variable was considered important since the surface roughness of conventional plasma sprayed ceramics (5.08-7.61 μm/200-300 μin AA) is greater than that desired for the intended turbine airfoil applications.

The high energy plasma process modifications were based on Task I coating systems 8 (2.5 cm/1 in. gun distance) and 11 (high energy gun), both of which were shown to be capable of producing long life strain tolerant coatings. To permit direct comparison of results, all of these modifications were performed on one composition (6 w% Y_2O_3 - ZrO_2). Modifications 8A and B were included to determine the relationship between the extent of segmentation (and in-plane cracking) and gun-to-specimen distance. The high energy spray process (8C) was included for direct comparison with Task I system 11 results. Modification 8D involved post-coat processing with the plasma torch to provide segmentation/microcracking.

Modifications of coating system 13 included variation of the pre-heat temperature and substitution of water quenching for liquid tin quenching as a potential production simplification. Two water quench pre-heat temperatures (982°C, 1800°F and 1079°C, 1975°F) were evaluated (system 13A and B). Two different tin quenching pre-heats (982°C, 1800°F and 1079°C, 2050°F) also were evaluated with systems 13C and D.

Two of the modifications of the 20 w% Y_2O_3 - ZrO_2 electron beam vapor deposited coating evaluated in Task I included variations of the Y_2O_3 stabilizer content. Specific compositions tested were 6 w% Y_2O_3 - ZrO_2 and 12 w% Y_2O_3 - ZrO_2 (system 16B and C). Two alternate ceramic compositions ($3Al_2O_3.2SiO_2$ and 23% CeO_2 - ZrO_2) also were evaluated (system 16A and D). These compositions were of interest because of their wide variation of chemical and physical properties which contributed to their utility as model systems to aid in defining the strain tolerance potential of micro-segmented coatings.

TABLE 4-I

TASK II COATING/PROCESS SYSTEMS[1]

	Ceramic Coating Type	Ceramic Layer	Modification
3	Controlled Substrate Temperature Plasma Spray Process	6 w% Y_2O_3 - ZrO_2	3A Fine spherical Powder (-325 Mesh)
			3B Coarse Spherical Powder (45% + 325 Mesh)
			3C Bimodal Distribution Angular Powder +200 Mesh 10%-40% -325 Mesh 65% max.
			3D Media Surface Finishing of 3C
8	High Energy Input Plasma Spray Process	6 w% Y_2O_3 - ZrO_2 (Distribution as in Mod. 3C)	8A 50 Volts 800 Amps-2.5 cm (1 inch) Gun Distance
			8B 50 volts 800 Amps-5.1 cm (2 inch) Gun Distance
			8C 50 Volts 1500 Amps-High Energy Gun - 15.2 - 33 cm (6-13 inch) Gun Distance
			8D Plasma Surface Treatment - Post Coating
13	Post Plasma Spray Thermal Shock	6 w% Y_2O_3 - ZrO_2 (Distribution is in Mod. 3C)	13A Water Quench from 982°C (1800°F) to RT
			13B Water Quench from 1079°C (1975°F) to RT
			13C Tin Quench from 982°C (1800°F) to 221°C (430°F)
			13D Tin Quench from 1121°C (2050°F) to 221°C (430°F)
16	Micro Segmented	Electron Beam Physical Vapor Deposited Ceramic	16A 3 Al_2O_3 - $2SiO_2$ (Mullite)
			16B 6% Y_2O_3 - ZrO_2
			16C 12% Y_2O_3 - ZrO_2
			16D 23% CeO_2 - ZrO_2

(1) = Metallic Coating Layer Applied Using Low Pressure Chamber Spray with Parameters Given in Table 3-IID

4.2 SPECIMEN PREPARATION AND CHARACTERIZATION

Except as noted in Table 4-I and in the following description, coating deposition and processing conditions were not changed from those used in coating Task I specimens. The metal bond coat under all plasma deposited coatings was applied by low pressure chamber spray using the parameters indicated in Table 3-IID. Substrate temperature control was used for all plasma ceramic coated specimens. Coating system 3D was media finished to a surface roughness of 2.49 μm (98 μin) AA. For comparison, surface roughness measurements taken on several other Task II specimens are listed in Table 4-II. Post-coating plasma surface treatment of system 8D was done immediately after coating by stopping the powder feed to the plasma gun while continuing specimen rotation and gun traverse. This procedure produced very high surface temperatures that caused melting of the outer regions of the coating, thus promoting additional segmentation cracking. Despite the use of substrate temperature control, substrate temperatures above 427°C (800°F) were experienced during application of coating systems 8C and D. Electron beam deposition of 3 Al_2O_3 - $2SiO_2$ was not successful and evaluation of system 16A thus was not continued through the balance of Task II. All plasma ceramic coated specimens were heat treated in hydrogen at 1079°C (1975°F) for four hours prior to burner rig testing. Subsequent to the hydrogen heat treatment, coating systems 13A-D were reheated in air to the temperature indicated in Table 4-I and were quenched either in room temperature water (systems 13A&B) or in 221°C (430°F) liquid tin (systems 13C&D). The EB-PVD coatings (systems 16B, C, and D) were heat treated in hydrogen at 1079°C (1975°F) for four hours after metallic coating and in air at 871°C (1600°F) for four hours after ceramic coating.

TABLE 4-II

TASK II PRE-TEST SURFACE ROUGHNESS MEASUREMENTS OF SELECTED COATINGS

Coating Modification System		Surface Roughness A.A. μm (μin.)	
3A	6 w% Y_2O_3 - ZrO_2 Fine Spherical Powder (-325 mesh)	3.50	138
3B	6 w% Y_2O_3 - ZrO_2 Coarse Spherical Powder (45% #325 mesh)	8.98	354
3C	6 w% Y_2O_3 - ZrO_2 Bimodal Distribution Angular Powder	6.55	258
3D	6 w% Y_2O_3 - ZrO_2 Media Surface Finishing (See Mod. 3C)	2.49	98
16B	6 w% Y_2O_3 - ZrO_2 EB-PVD	2.28	90
16C	12 w% Y_2O_3 - ZrO_2 EB-PVD	2.11	83
16D	23 w% CeO_2O_3 - ZrO_2 EB-PVD	1.19	47

As in Task I, coatings produced in this task were evaluated metallographically and by x-ray diffraction prior to testing. X-ray diffraction results are presented in Table 4-III. Photomicrographs of each coating system are included in Figures 4-1 through 4-16.

Phase distributions observed in the 6 w% Y_2O_3 - ZrO_2 plasma sprayed coatings are more or less consistent with those measured in Task I. Relatively small amounts of monoclinic (less than 8%) were found, with the predominant phase being tetragonal. There was, however, substantial variability of the relative amounts of tetragonal and cubic phases present in each coating, depending on specific conditions. Specimens with exceptionally high tetragonal (and correspondingly low cubic) phases include the coating produced with coarse spherical powder (3B), and the coatings quenched from 982°C (1800°F). The reason for this result in system 3B is not fully understood, but may be related to the inherently nonhomogeneous nature of the spray-dried spherical powder. The observation of low cubic content in coatings 13A and C quenched from 982°C (1800°F) is attributed to equilibration of the tetragonal structure at 982°C (1800°F) just within the tetragonal plus cubic phase field shown on the phase diagram of Stubican et. al. (Reference 15). The somewhat higher cubic content of coatings 13B and D which were equilibrated and quenched from higher temperatures is consistent with this rationalization. The data also suggests that the tetragonal-to-monoclinic transformation was entirely suppressed by the very high cooling rate tin quench applied to coatings 13C and D.

The phase distributions observed in the EB-PVD coatings are somewhat puzzling. The 6 w% Y_2O_3 - ZrO_2 coating was predominantly cubic, with a small amount (5%) monoclinic in the as-deposited condition. The higher (12%) Y_2O_3 coating also was predominantly cubic, but contained 5% free Y_2O_3. Predominance of the cubic phase in the EB-PVD 6 w% Y_2O_3 - ZrO_2 coating might be attributed to preferential enrichment of the Y_2O_3 in the EB-PVD deposit, which would tend to stabilize the cubic phase. This enrichment could result from the higher vapor pressure of Y_2O_3 as compared to ZrO_2, which would tend to enrich yttrium in the vapor cloud. This observation is consistent with the observation of free Y_2O_3 in the nominal 12% Y_2O_3 - ZrO_2 EB-PVD coating. It is not, however, consistent with the absence of free Y_2O_3 in the 20 w% Y_2O_3 - ZrO_2 coating studied in Task I (Table 3-III). What is clear about the EB deposited Y_2O_3 stabilized zicronias is that they tend to deposit (and remain) virtually 100% cubic, as opposed to the CeO_2 stabilized ZrO_2, which deposited as 100% tetragonal phase.

Metallographic evaluation of the as-deposited coatings indicated a range of microstructural strain relief features, as shown in Figure 4-1 through 4-16. Typical low pressure chamber sprayed bond coat structures are shown in Figures 4-1A and C. To aid in interpretation of the ceramic structures, a qualitative assessment of the relative amounts of various strain relief features is listed in Table 4-IV.

TABLE 4-III

TASK II X-RAY DIFFRACTION PHASE ANALYSIS OF COATING SURFACE

Coating System Number	Ceramic Layer	Post-Coating Processing	Exposure Cycles For Post-Test Specimen	VOLUME PERCENT OF PHASE PRESENT[1] Cubic ZrO_2 Pre-Test	Cubic ZrO_2 Post-Test	Tetragonal ZrO_2 Pre-Test	Tetragonal ZrO_2 Post-Test	Monoclinic ZrO_2 Pre-Test	Monoclinic ZrO_2 Post-Test	Y_2O_3 Pre-Test	Y_2O_3 Post-Test
3A	6w% Y_2O_3 - ZrO_2 Fine Spherical Powder (-325 Mesh)	1079°C (1975°F)/4 hrs./H_2	5250	40	62	60	35	0	3	-	-
3B	6w% Y_2O_3 - ZrO_2 Coarse Spherical Powder (45% +325 Mesh)	1079°C (1975°F)/4 hrs./H_2	6180	7	55	85	42	8	3	-	-
3C	6w% Y_2O_3 - ZrO_2 Bimodal Distribution Angular Powder	1079°C (1975°F)/4 hrs./H_2	2380	20	58	73	40	7	2	-	-
3D	6w% Y_2O_3 - ZrO_2 Bimodal Distribution Angular Powder-Media Surface Finishing	1079°C (1975°F)/4 hrs./H_2	2110	22	60	73	38	5	2	-	-
8A	6w% Y_2O_3 - ZrO_2 Bimodal Distribution Angular Powder, 2.5 cm (1 inch) Gun-To-Specimen Distance	1079°C (1975°F)/4 hrs./H_2	6180	30	60	62	38	8	2	-	-
8B	6w% Y_2O_3 - ZrO_2 Bimodal Distribution Angular Powder, 5.1 cm (2 inch) Gun-To-Specimen Distance	1079°C (1975°F)/4 hrs./H_2	6180	40	58	53	40	7	2	-	-
8C	6w% Y_2O_3 - ZrO_2 Bimodal Distribution High Energy Gun	1079°C (1975°F)/4 hrs./H_2	200	40	58	55	40	5	2	-	-
8D	6w% Y_2O_3 - ZrO_2 Bimodal Distribution Post Coating Plasma Surface Treatment	1079°C (1975°F)/4 hrs./H_2	2040	55	65	42	32	3	3	-	-
13A	6w% Y_2O_3 - ZrO_2 Bimodal Distribution Angular Powder	1079°C (1975°F)/4 hrs./H_2 + Water Quench from 982°C (1800°F) to Room Temp.	3240	0	58	95	40	5	2	-	-
13B	6w% Y_2O_3 - ZrO_2 Bimodal Distribution Angular Powder	1079°C (1975°F)/4 hrs./H_2 + Water Quench from 1079°C (1975°F) to Room Temp.	1050	25	75	70	22	5	3	-	-
13C	6w% Y_2O_3 - ZrO_2 Bimodal Distribution Angular Powder	1079°C (1975°F)/4 hrs./H_2 + Tin Quench from 982°C (1800°F) to 221°C (430°F)	1050	10	60	90	38	0	2	-	-
13D	6w% Y_2O_3 - ZrO_2 Bimodal Distribution Angular Powder	1079°C (1975°F)/4 hrs./H_2 + Tin Quench from 1121°C (2050°F) to 221°C (430°F)	2090	25	58	75	40	0	2	-	-
16B	6w% Y_2O_3 - ZrO_2 EB-PVD	1079°C(1975°F)/4 hrs./H_2 After Metallic Coating, 871°C (1600°F)/4 hrs./Air After Ceramic Coating	5770	95	100	0	-	5	-	-	-
16C	12w% Y_2O_3 - ZrO_2 EB-PVD	1079°C(1975°F)/4 hrs./H_2 After Metallic Coating, 871°C (1600°F)/4 hrs./Air After Ceramic Coating	5640	95	100	0	-	0	-	5	-
16D	23w% CeO_2 - ZrO_2 EB-PVD	1079°C(1975°F)/4 hrs./H_2 After Metallic Coating, 871°C (1600°F)/4 hrs./Air After Ceramic Coating	5070	0	70	100	30	0	-	-	-

[1]Accuracy tolerances are generally ±5%

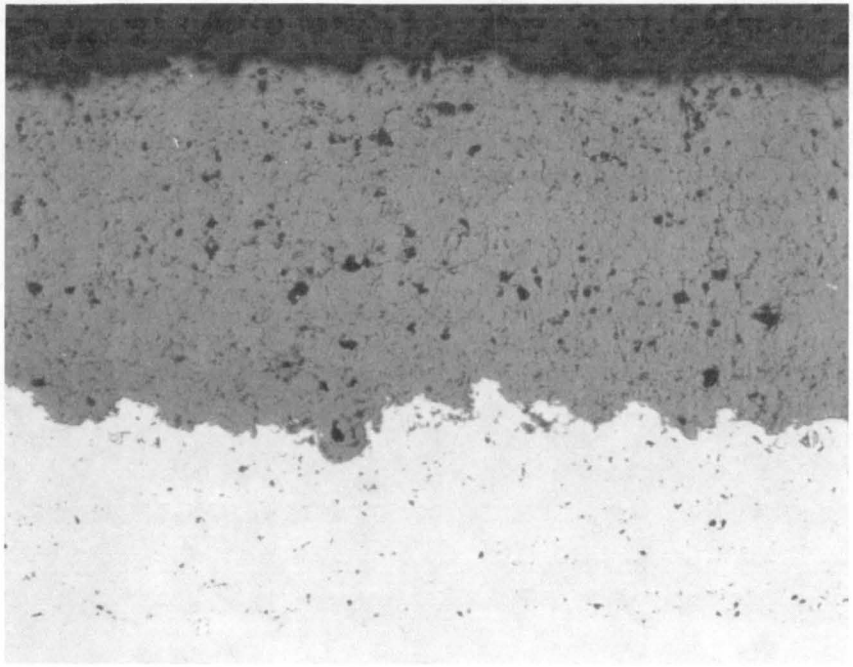

A) PRE-TEST LIGHT PHOTOMICROGRAPH 200X

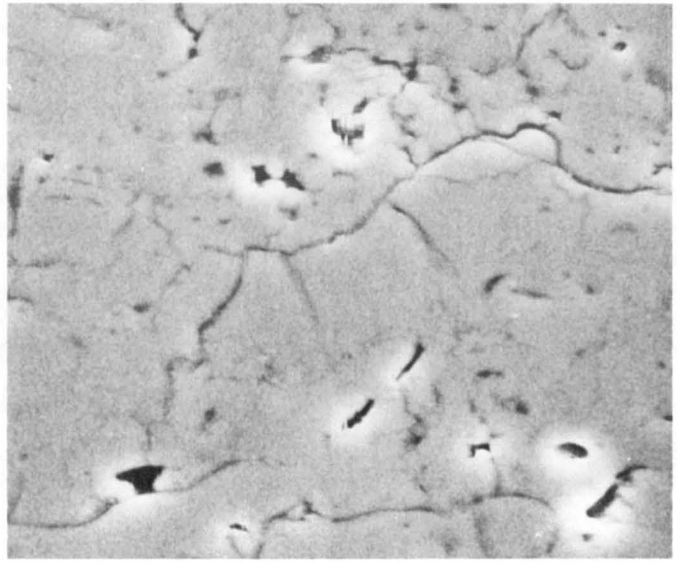

2000X

B) PRE-TEST SCANNING ELECTRON MICROGRAPH

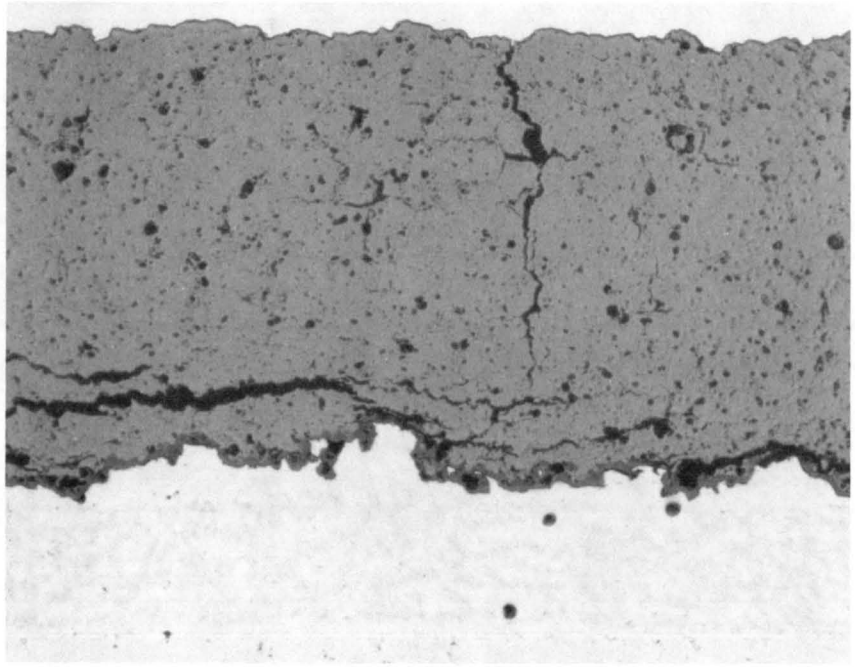

C) POST-TEST LIGHT PHOTOMICROGRAPH 200X

Figure 4-1 Microstructures observed in Task II coating system 3A (plasma spray 6 w% Y_2O_3 -ZrO_2, fine (-325 mesh) spherical powder) before and after 5250 cycles of burner rig exposure at 1107°C (2025°F)

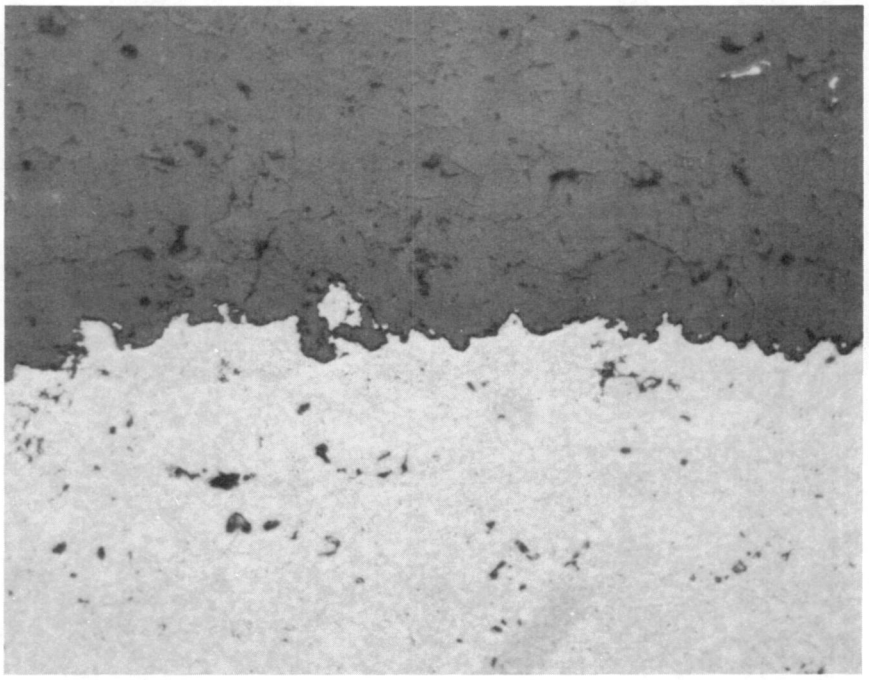

D) PRE-TEST INTERFACE 500X

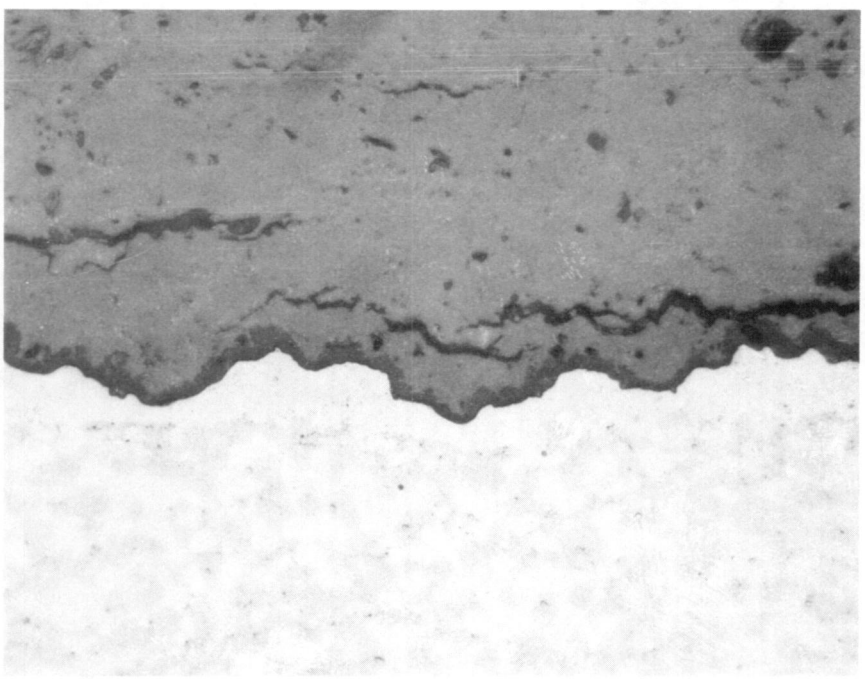

E) POST—TEST, SHOWING OXIDE SCALE GROWTH AT INTERFACE 500X

Figure 4-1 (Continued) Microstructures observed in Task II coating system 3A (plasma spray 6 w% Y_2O_3 -ZrO_2, fine (-325 mesh) spherical powder) showing details of metallic-ceramic interface before and after test

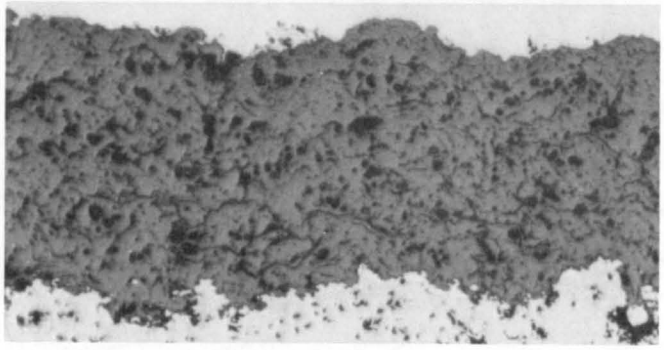

150X

A) PRE-TEST LIGHT PHOTOMICROGRAPH

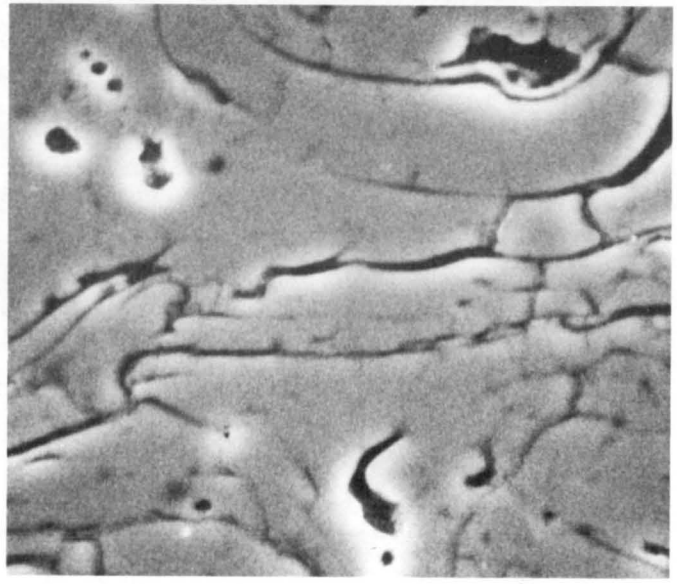

2000X

B) PRE-TEST SCANNING ELECTRON MICROGRAPH

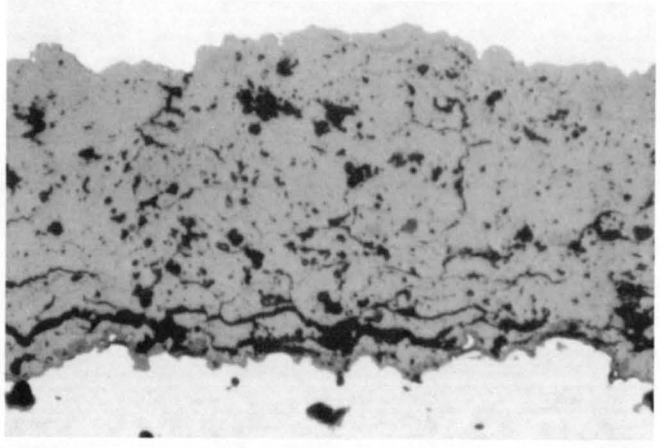

150X

C) POST-TEST LIGHT PHOTOMICROGRAPH

Figure 4-2 Microstructures observed in Task II coating system 3B (plasma spray 6 w% Y_2O_3 -ZrO_2, coarse (45% + 325 mesh) spherical powder) before and after 6180 cycles of burner rig exposure at 1107°C (2025°F)

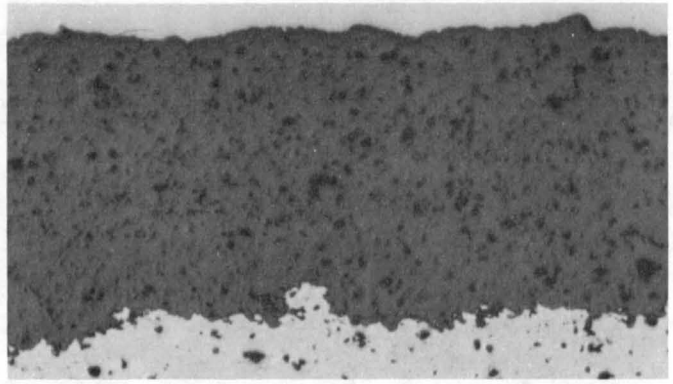

150X

A) PRE-TEST LIGHT PHOTOMICROGRAPH

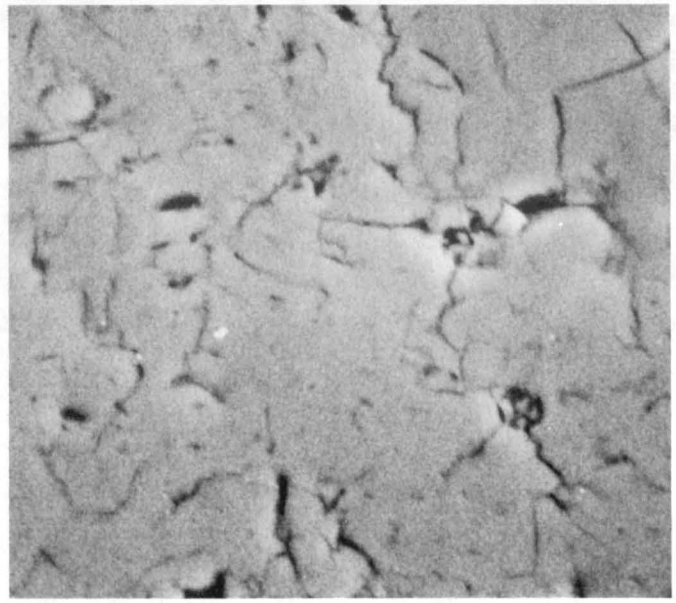

2000X

B) PRE-TEST SCANNING ELECTRON MICROGRAPH

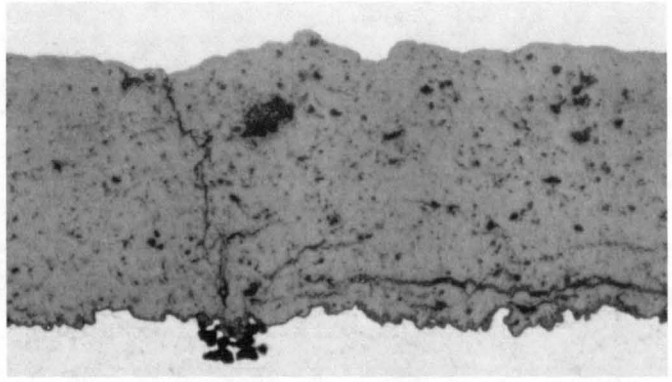

150X

C) POST-TEST LIGHT PHOTOMICROGRAPH

Figure 4-3 Microstructures observed in Task II coating system 3C (plasma spray 6 w% Y_2O_3 -ZrO_2, bimodal distribution angular powder) before and after 6180 cycles of burner rig exposure at 1107°C (2025°F)

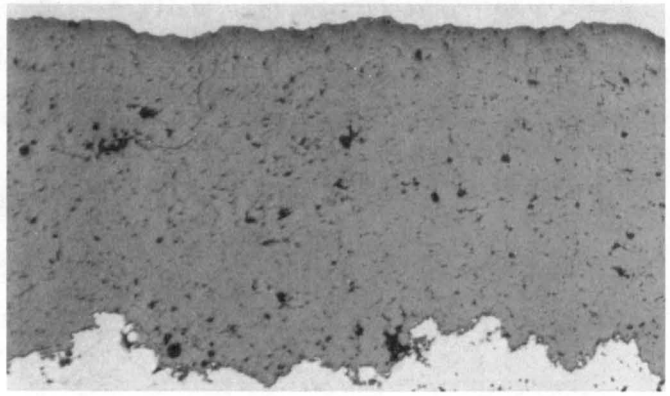

150X

A) PRE-TEST LIGHT PHOTOMICROGRAPH

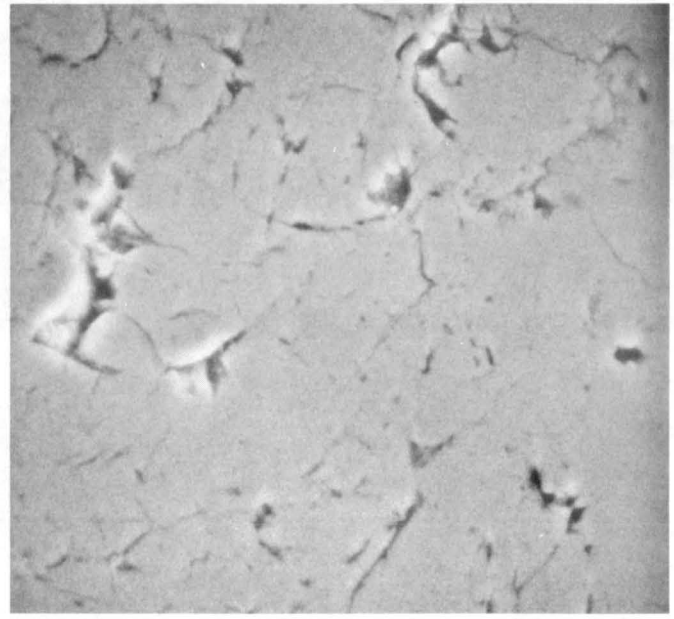

2000X

B) PRE-TEST SCANNING ELECTRON MICROGRAPH

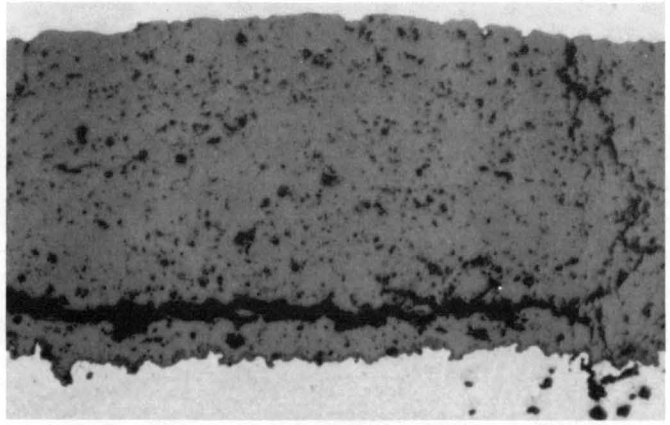

150X

C) POST-TEST LIGHT PHOTOMICROGRAPH

Figure 4-4 Microstructures observed in Task II coating system 3D (plasma spray 6 w% Y_2O_3 -ZrO_2, media surface finished) before and after 2110 cycles of burner rig exposure at 1107°C (2025°F)

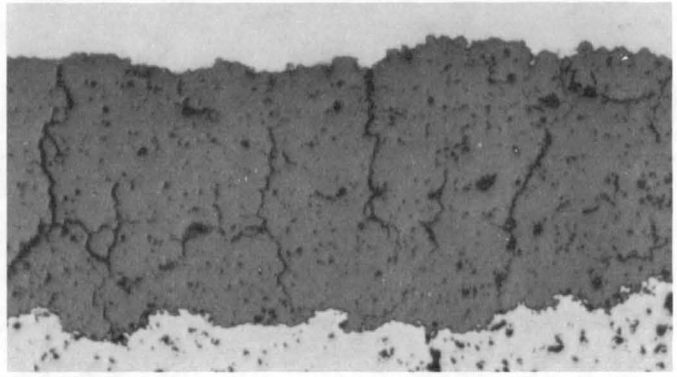

150X

A) PRE-TEST LIGHT PHOTOMICROGRAPH

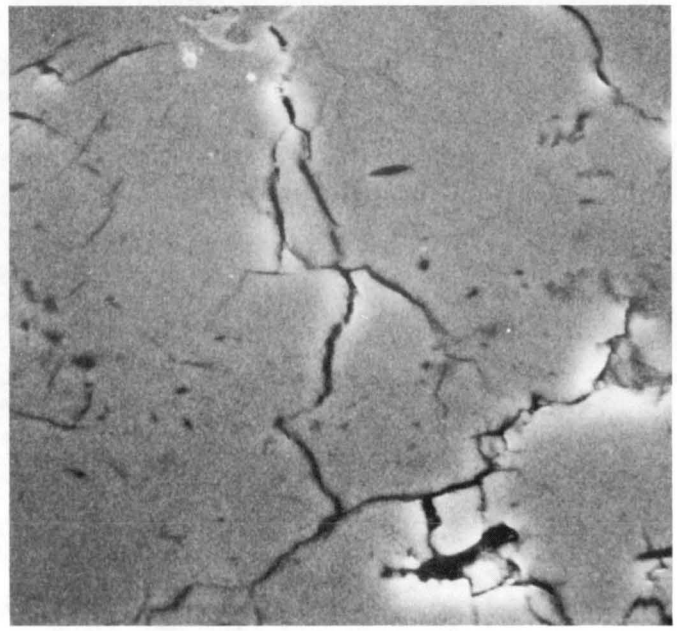

2000X

B) PRE-TEST SCANNING ELECTRON MICROGRAPH

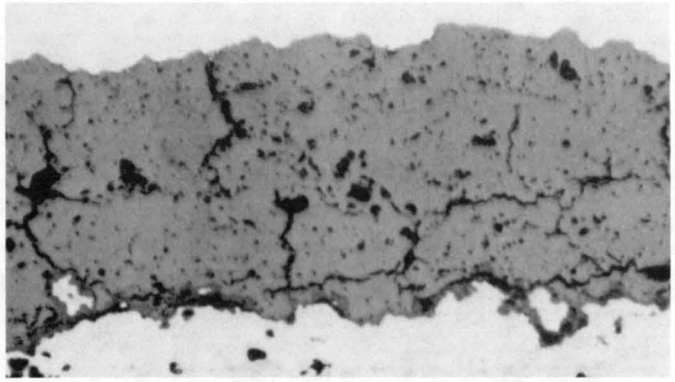

150X

C) POST-TEST LIGHT PHOTOMICROGRAPH

Figure 4-5 Microstructures observed in Task II coating system 8A (plasma spray 6 w% Y_2O_3 -ZrO_2, 1 inch gun-to-specimen distance) before and after 6180 cycles of burner rig exposure at 1107°C (2025°F)

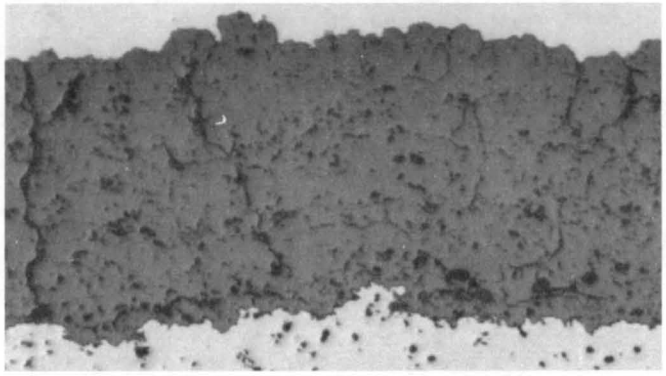

150X

A) PRE-TEST LIGHT PHOTOMICROGRAPH

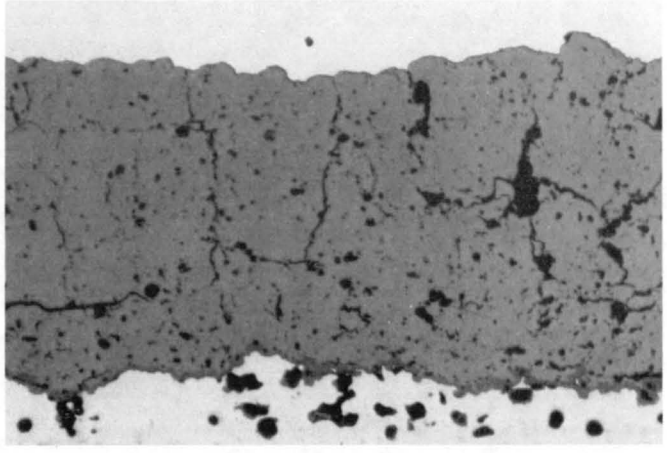

150X

C) POST-TEST LIGHT PHOTOMICROGRAPH

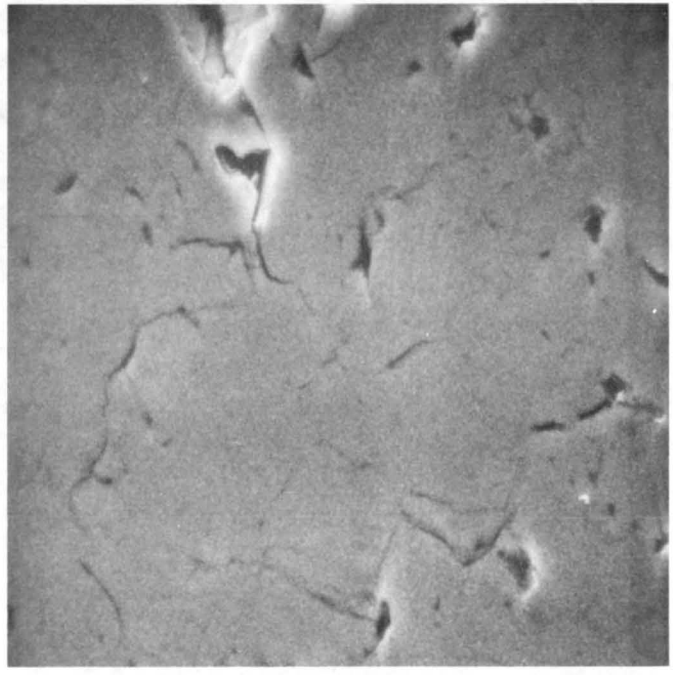

2000X

B) PRE-TEST SCANNING ELECTRON MICROGRAPH

Figure 4-6 Microstructures observed in Task II coating system 8B (plasma spray 6 w% Y_2O_3 -ZrO_2, 2 inch gun-to-specimen distance) before and after 6180 cycles of burner rig exposure at 1107°C (2025°F)

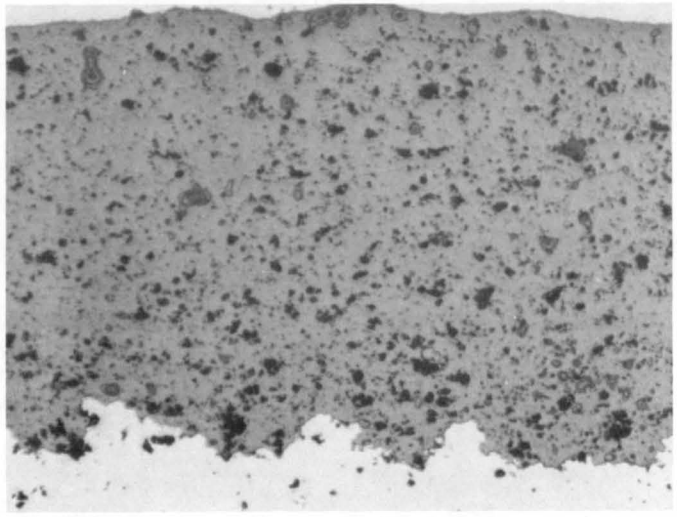

150X

A) PRE-TEST LIGHT PHOTOMICROGRAPH

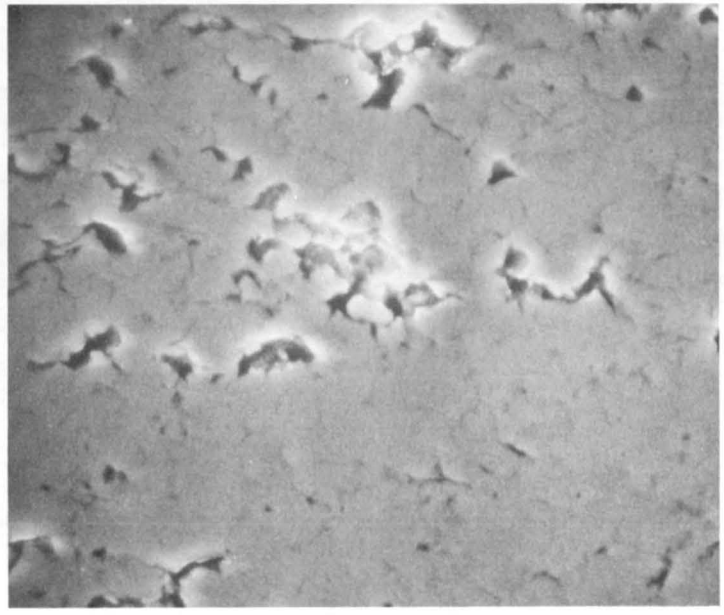

2000X

B) PRE-TEST SCANNING ELECTRON MICROGRAPH

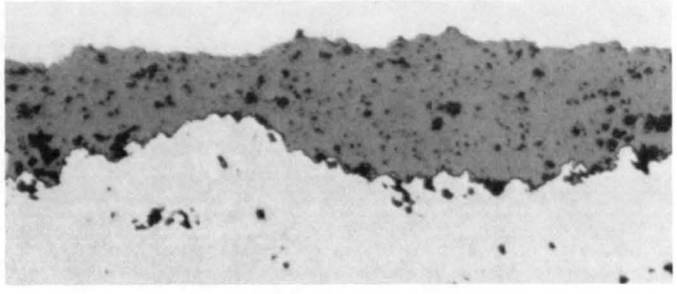

150X

C) POST-TEST LIGHT PHOTOMICROGRAPH

Figure 4-7 Microstructures observed in Task II coating system 8C (plasma spray 6 w% Y_2O_3 -ZrO_2) before and after 200 cycles of burner rig exposure at 1107°C (2025°F)

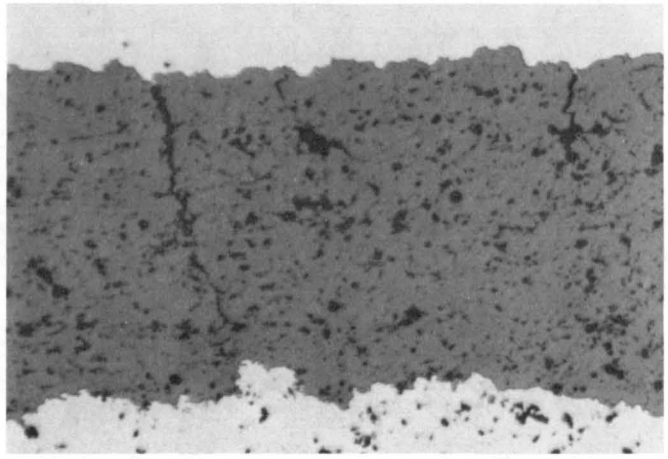

150X

A) PRE-TEST LIGHT PHOTOMICROGRAPH

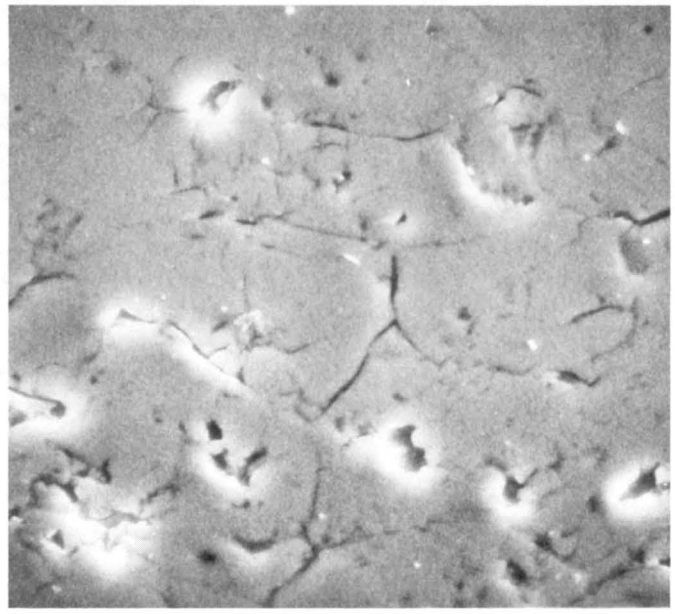

2000X

B) PRE-TEST SCANNING ELECTRON MICROGRAPH

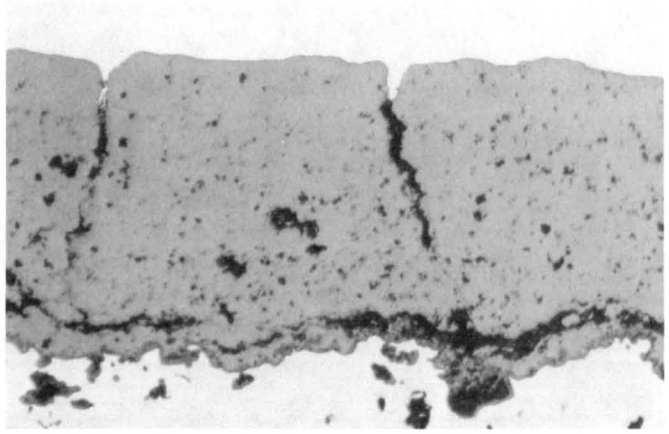

150X

C) POST-TEST LIGHT PHOTOMICROGRAPH

Figure 4-8 Microstructures observed in Task II coating system 8D (plasma spray 6 w% Y_2O_3 -ZrO_2) post-coating plasma surface treatment) before and after 2040 cycles of burner rig exposure at 1107°C (2025°F)

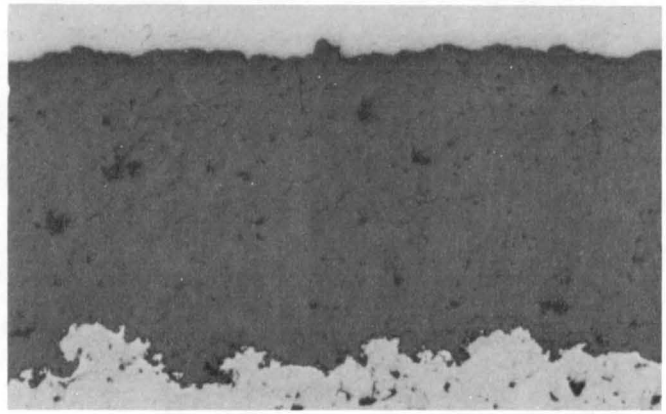

150X

A) PRE-TEST LIGHT PHOTOMICROGRAPH

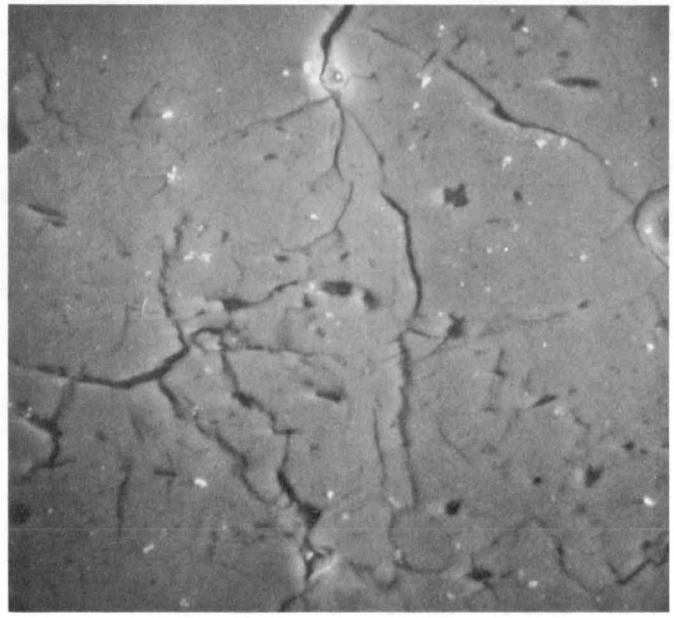

2000X

B) PRE-TEST SCANNING ELECTRON MICROGRAPH

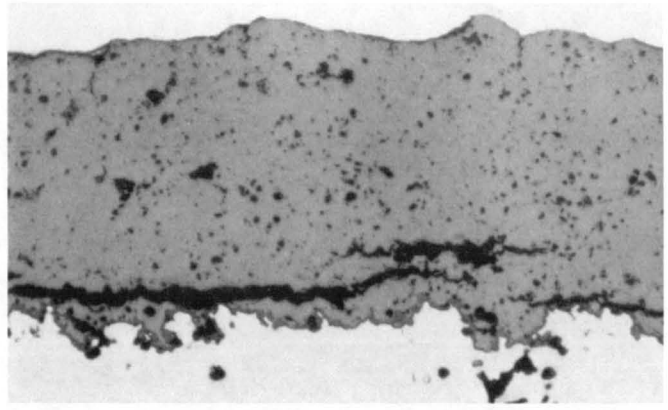

150X

C) POST-TEST LIGHT PHOTOMICROGRAPH

Figure 4-9 Microstructures observed in Task II coating system 13A (plasma spray 6 w% Y_2O_3 -ZrO_2, water quench from 892°C (1800°F) to room temperature) before and after 3240 cycles of burner rig exposure at 1107°C (2025°F)

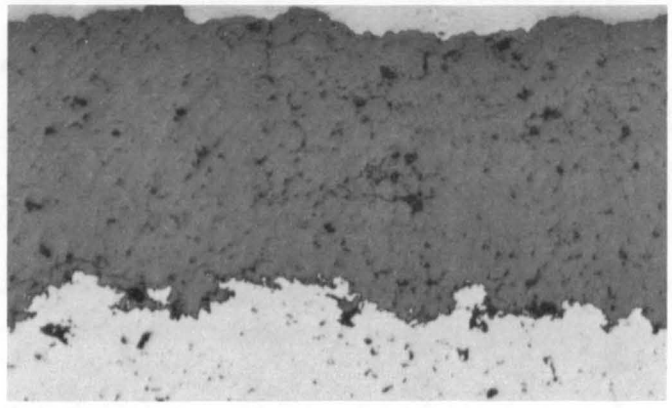

150X

A) PRE-TEST LIGHT PHOTOMICROGRAPH

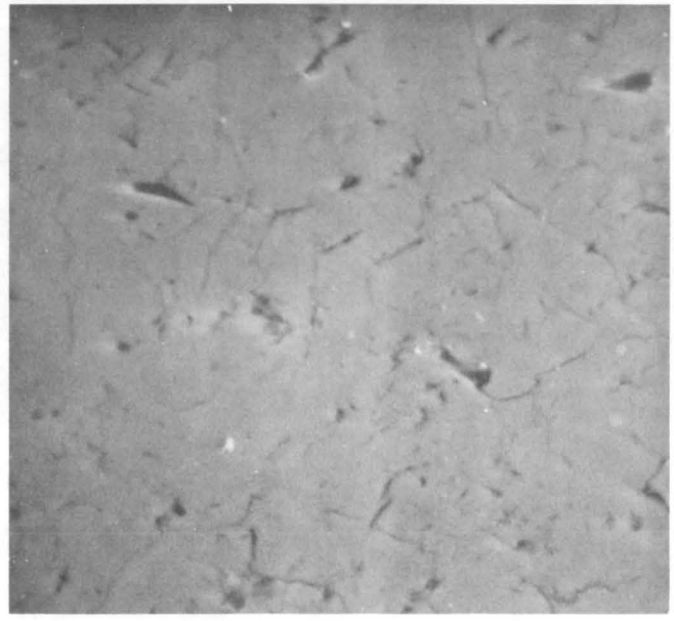

2000X

B) PRE-TEST SCANNING ELECTRON MICROGRAPH

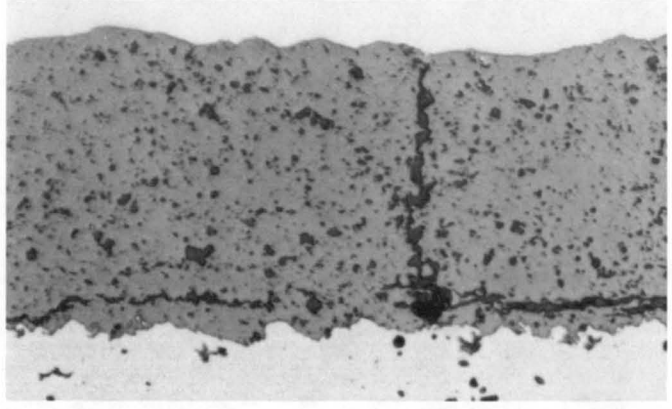

150X

C) POST-TEST LIGHT PHOTOMICROGRAPH

Figure 4-10 Microstructures observed in Task II coating system 13B (plasma spray 6 w% Y_2O_3 -ZrO_2, water quench from 1079°C (1975°F) to room temperature) before and after 3240 cycles of burner rig exposure at 1107°C (2025°F)

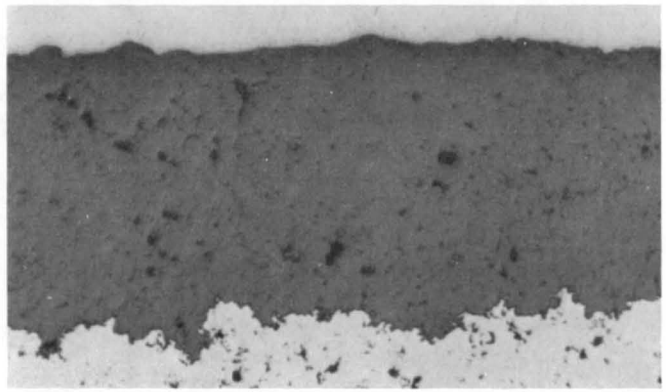

150X

A) PRE-TEST LIGHT PHOTOMICROGRAPH

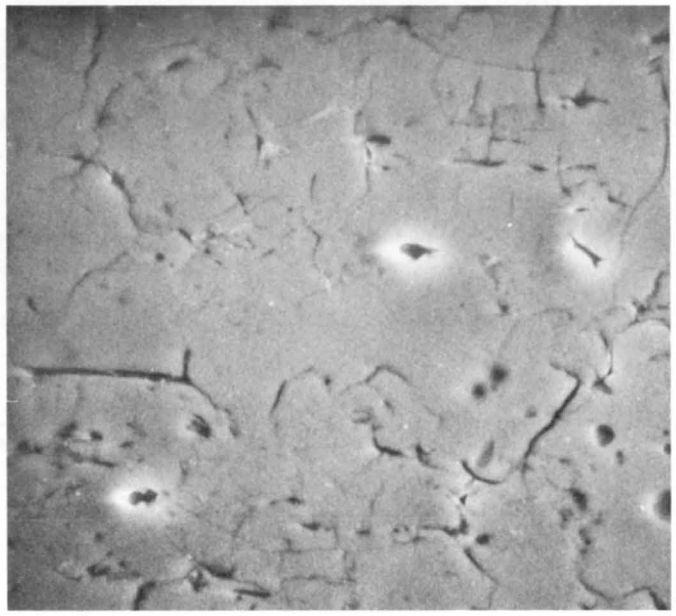

2000X

B) PRE-TEST SCANNING ELECTRON MICROGRAPH

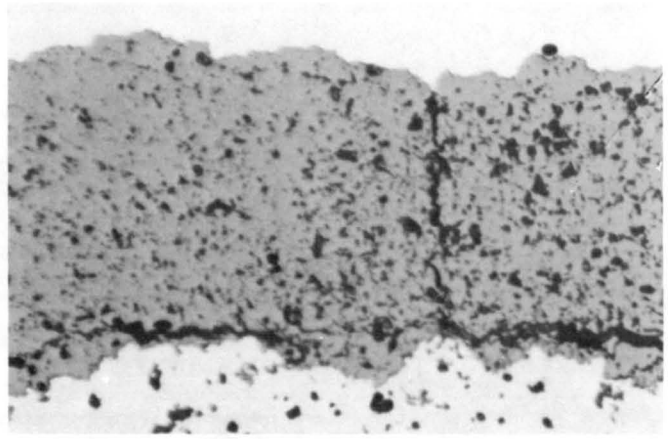

150X

C) POST-TEST LIGHT PHOTOMICROGRAPH

Figure 4-11 Microstructures observed in Task II coating system 13C (plasma spray 6 w% Y_2O_3 -ZrO_2, tin quench from 982°C (1800°F) to 221°C (430°F) before and after 1050 cycles of burner rig exposure at 1107°C (2025°F)

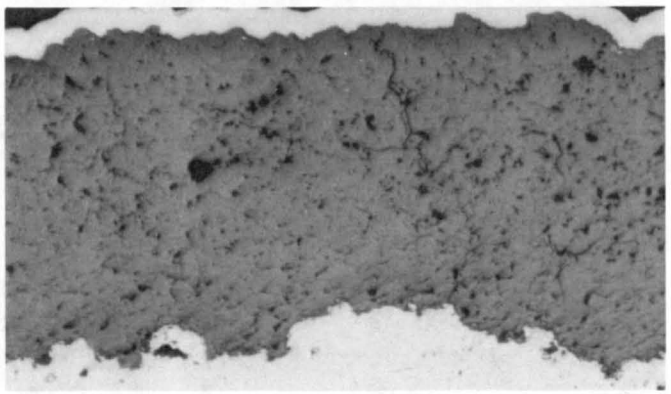

150X

A) PRE-TEST LIGHT PHOTOMICROGRAPH

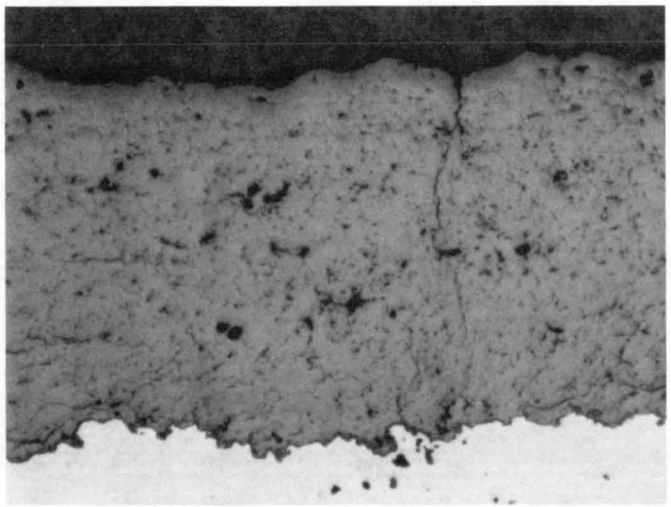

150X

C) POST-TEST LIGHT PHOTOMICROGRAPH

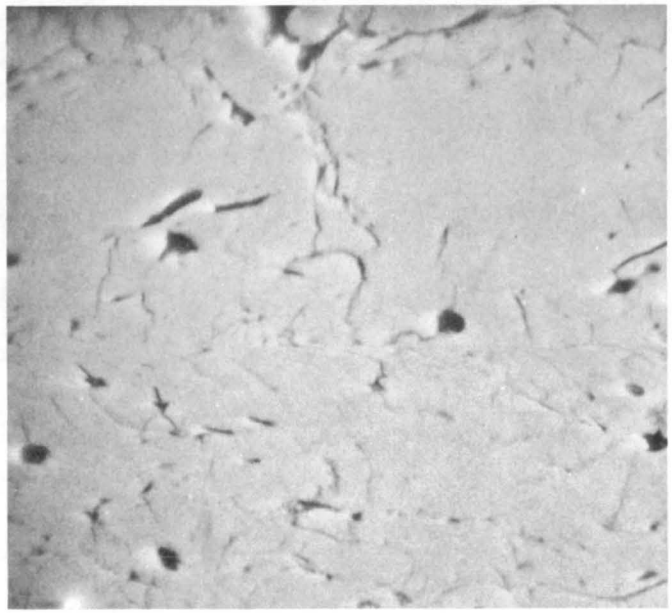

2000X

B) PRE-TEST SCANNING ELECTRON MICROGRAPH

Figure 4-12 Microstructures observed in Task II coating system 13D (plasma spray 6 w% Y_2O_3 -ZrO_2, tin quench from 1121°C (2050°F) to 221°C (430°F) before and after 2090 cycles of burner rig exposure at 1107°C (2025°F)

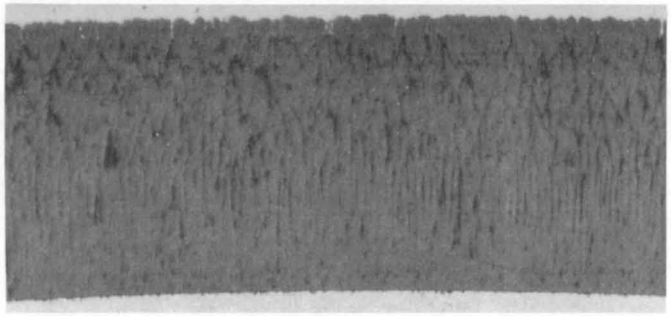

150X

A) PRE-TEST LIGHT PHOTOMICROGRAPH

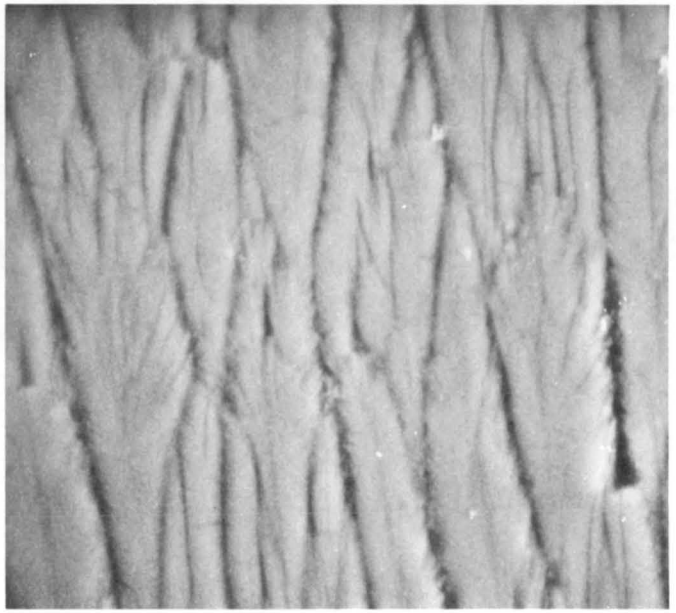

2000X

B) PRE-TEST SCANNING ELECTRON MICROGRAPH

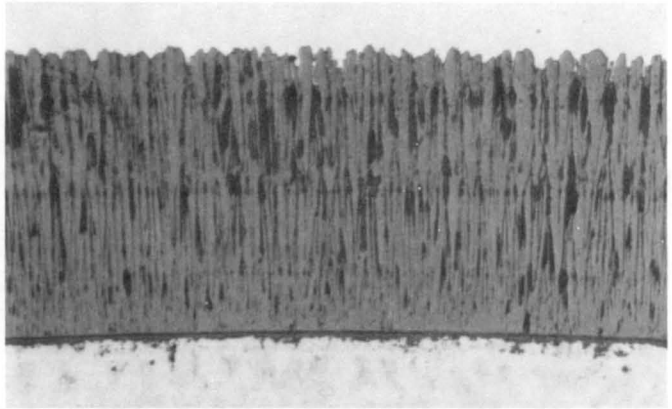

150X

C) POST-TEST LIGHT PHOTOMICROGRAPH

Figure 4-13 Microstructures observed in Task II coating system 16B (EB-PVD 6 w% Y_2O_3-ZrO_2) before and after 5770 cycles of burner rig exposure at 1107°C (2025°F)

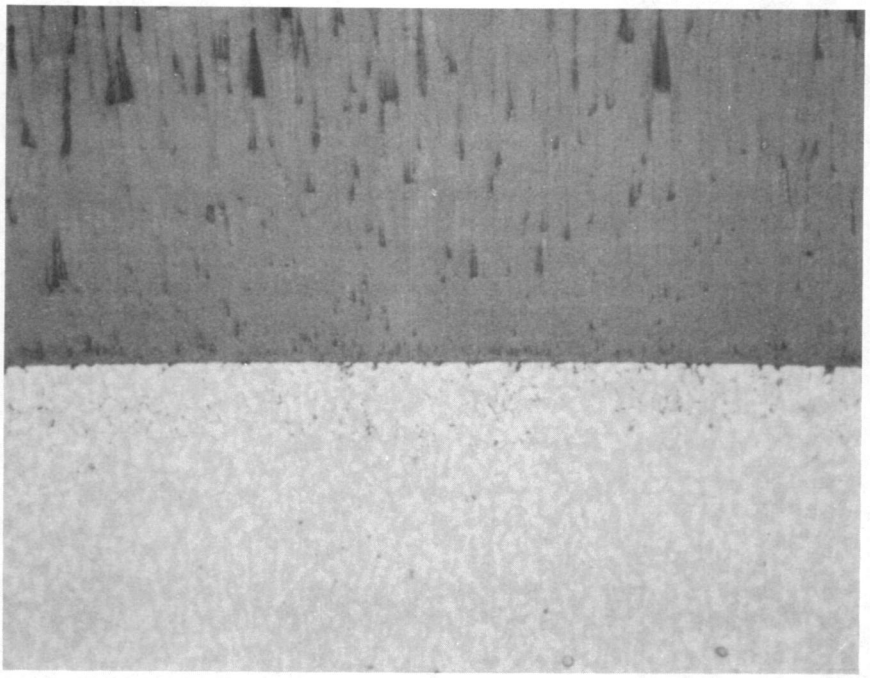

D) PRE-TEST INTERFACE 500X

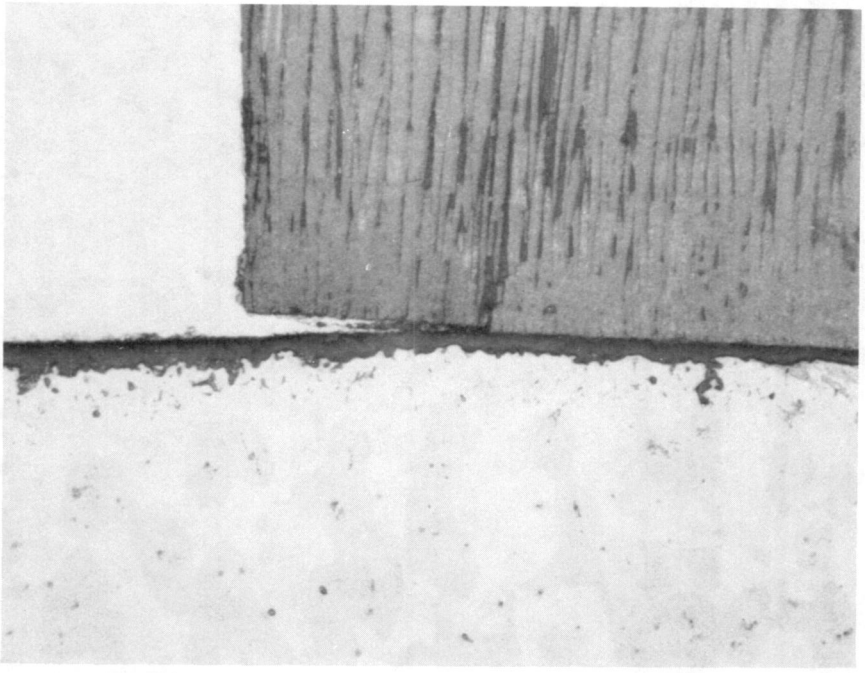

E) POST-TEST, SHOWING OXIDE SCALE GROWTH AT INTERFACE 500X

Figure 4-13 (Continued) Microstructures observed in Task II coating system 16B (EB-PVD 6 w% Y_2O_3-ZrO_2) showing detail of metallic ceramic interface before and after test

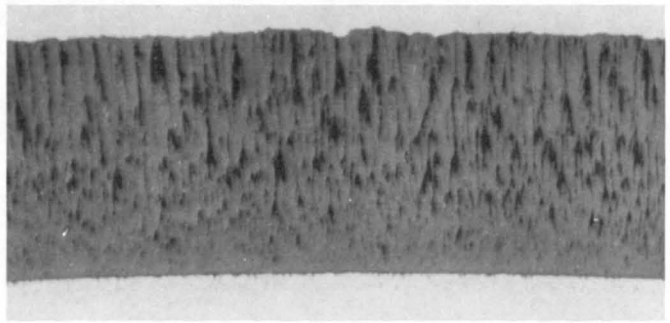

150X

A) PRE-TEST LIGHT PHOTOMICROGRAPH

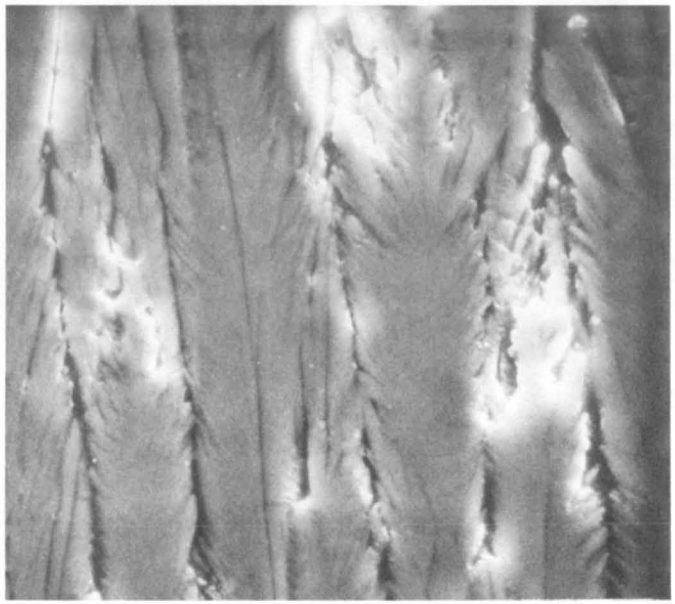

2000X

B) PRE-TEST SCANNING ELECTRON MICROGRAPH

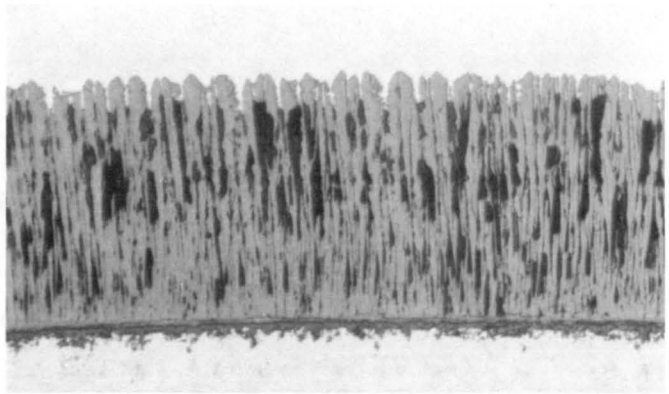

150X

C) POST-TEST LIGHT PHOTOMICROGRAPH

Figure 4-14 Microstructures observed in Task II coating system 16C (EB-PVD 12 w% Y_2O_3-ZrO_2) before and after 5640 cycles of burner rig exposure at 1107°C (2025°F)

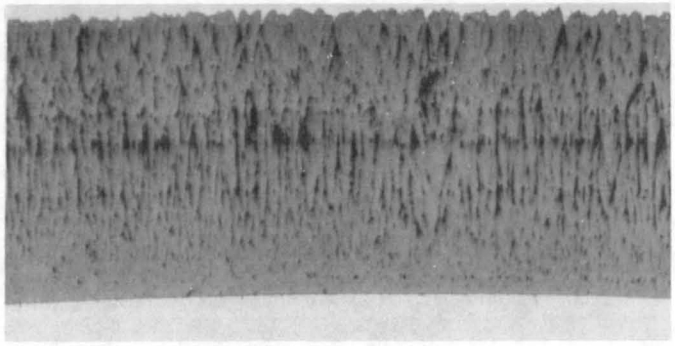

150X

A) PRE-TEST LIGHT PHOTOMICROGRAPH

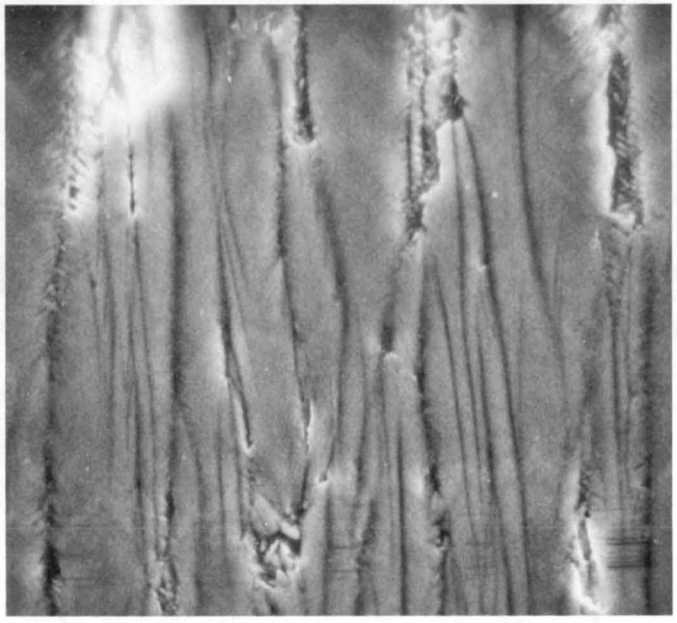

2000X

B) PRE-TEST SCANNING ELECTRON MICROGRAPH

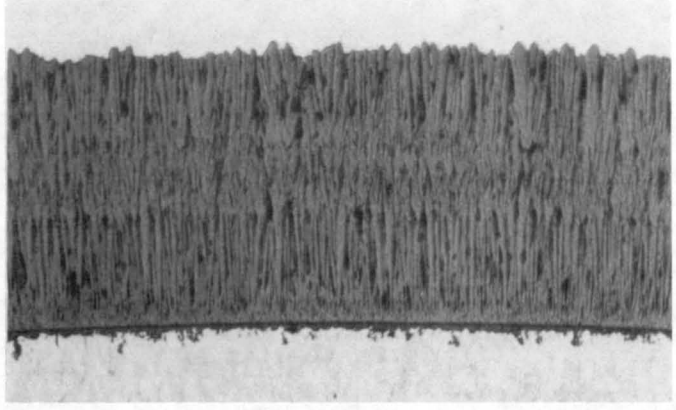

150X

C) POST-TEST LIGHT PHOTOMICROGRAPH

Figure 4-15 Microstructures observed in Task II coating system 16D (EB-PVD 23 w% CeO_2-ZrO_2) before and after 5070 cycles of burner rig exposure at 1107°C (2025°F)

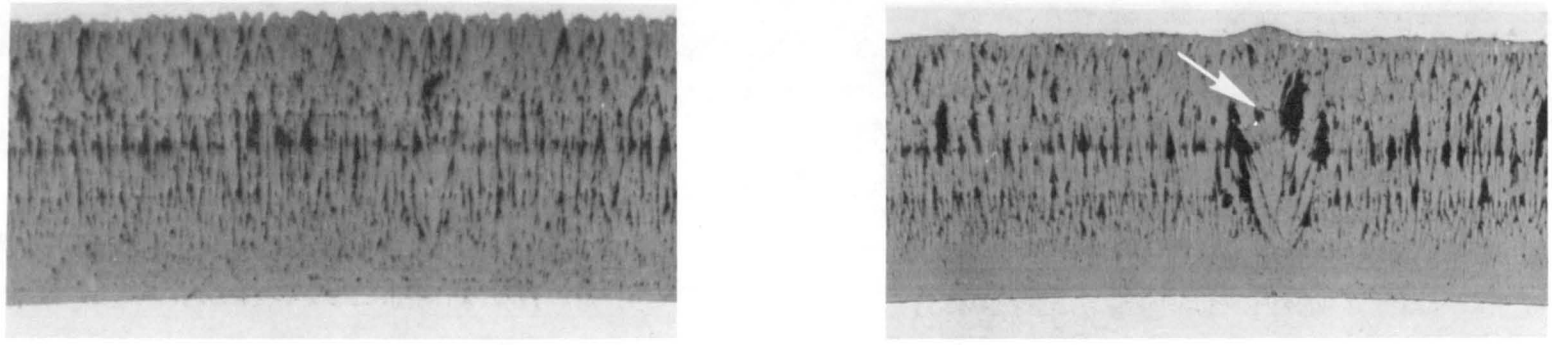

150X

A) NORMAL COATING MICROSTRUCTURE

150X

B) GROWTH IRREGULARITY

Figure 4-16 Pre-Test Microstructures of 23 w% CeO_2-ZrO_2 EB-PVD Coating System Modification 16D Exhibiting Normal Microstructure (Left) and Growth Irregularity (Right)

As expected, the three EB-PVD coatings which survived processing possessed a very high level of micro-segmentation resulting from the fine columnar nature of the EB-PVD microstructure (Figures 4-13 through 16). A few growth irregularities were observed in coating system 16D (EB-PVD 23 w% CeO_2 - ZrO_2) as shown in Figure 4-16; based on subsequently described burner rig test results, these structural irregularities apparently did not significantly degrade the performance of this coating. The plasma sprayed ceramic applied with 2.5 and 5.1 cm (1 and 2 inch) gun-to-specimen distances possessed high and moderately high levels of segmentation shown in Figures 4-5 and 4-6, respectively, with the balance of the plasma coatings having low-to-moderate levels of this strain relief feature (Figures 4-1 through 4-4 and 4-8 through 4-12).

Moderate to low levels of micro-cracking were observed in process variation 3A (fine spherical powder, Figure 4-1) and in the four quenched structures (systems 13A-D, Figures 4-9 through 4-12), with the balance of the plasma sprayed coatings having low or very low levels of micro-cracking (Figures 4-2 through 4-8 and 4-13 through 4-16). Substantial quantities of porosity and segmentation-cracking, observed in coating 3B (coarse spherical, Figure 4-2) and 8A (2.5, one inch, gun distance, Figure 4-5), respectively, may be beneficial in preventing catastrophic growth of the moderate-high levels of in-plane cracking found in these coatings.

4.3 TASK II BURNER RIG EVALUATION

Triplicate specimens coated with each of the systems listed in Table 4-I, except system 16A, were cyclic burner rig tested at 1107°C (2025°F). Test procedures and failure criteria were as described for Task I (Section 3.3 and Appendix A). Results of these tests are presented in Table 4-V and Figure 4-17. Coating systems/modifications identified as providing superior resistance to cyclic thermal spalling include plasma sprayed ceramics made with coarse spherical powder (system 3B), and with high energy input (system 8A). Promising electron beam vapor deposited coatings include both the 6 w% and 12w% Y_2O_3 - ZrO_2 compositions (systems 16B and C, respectively). Comments concerning the correlation between structural observations and burner rig performance of each coating are included in the following section.

4.4 EVALUATION OF TESTED SPECIMENS

Post-test evaluation included x-ray diffraction and metallographic examination. Results of these analyses are included with corresponding pre-test results in Table 4-III and in Figures 4-1 through 4-16.

As indicated by the x-ray data in Table 4-III, there is a general trend toward decreasing tetragonal and increasing cubic phase in the exposed plasma sprayed coatings. With the exception of system 13B, the percentages of tetragonal and cubic phases appear to stabilize in the range of 32 to 42 percent and 55 to 65 percent, respectively. The behavior of system 13B is not understood. There also is a general trend toward decreasing monoclinic phase except for those coatings which had no monoclinic in the as-deposited condition, in which cases small increases occur. All of the plasma sprayed coatings seem to stabilize with monoclinic percentages in the range of two to three percent.

TABLE 4-IV

PRE-TEST TASK II THERMAL BARRIER COATING
MICROSTRUCTURAL OBSERVATIONS

Coating Modification Systems		Segmentation or Segmentation-Cracking	Micro-Cracking	Porosity	In Plane Cracking
3A	Fine Spherical Powder (-325 mesh)	low-moderate	low-moderate	low	low
3B	Coarse Spherical Powder (45% + 325 mesh)	very low	low	moderate-high	moderate-high
3C	Bimodal Distribution Angular Powder	low-moderate	moderate	low	--
3D	Media Surface Finishing (See Mod. 3C)	low-moderate	moderate	low	--
8A	2.5 cm (1 inch) Gun-to-Specimen Distance	high	low	low	moderate
8B	5.1 cm (2 inch) Gun-to-Specimen Distance	moderate-high	low	low	low
8C	High Energy Gun	moderate	low	low-moderate	--
8D	Post-Coating Plasma Surface Treatment	moderate	moderate	low-moderate	--
13A	Water Quench 982°C (1800°F) to R.T.	low	moderate	low	low-moderate
13B	Water Quench 1079°C (1975°F) to R.T.	low	moderate	low	low-moderate
13C	Tin Quench 982°C (1800°F) to 221°C (430°F)	low	moderate	low	low
13D	Tin Quench 1121°C (2050°F) to 221°C (430°F)	moderate	moderate	low	moderate
16B	EB-PVD 6 w% Y_2O_3 - ZrO_2	very high	--	--	--
16C	EB-PVD 12 w% Y_2O_3 - ZrO_2	very high	--	--	--
16D	EB-PVD 23 w% CeO_2 - ZrO_2	very high	--	--	--

TABLE 4-V

TASK II CYCLIC THERMAL TEST RESULTS

Coating System Number	Ceramic Coating Layer	Post-Coating Processing	Cycles to [1] Ceramic Coating Failure Bar 1	Bar 2	Bar 3	Avg.
3A	6 w% Y_2O_3 - ZrO_2 Fine Spherical Powder (-325 Mesh)	1079°C (1975°F)/4 hrs./H_2	3910	4840	5250	4666
3B	6 w% Y_2O_3 - ZrO_2 Coarse Spherical Powder (45% + 325 Mesh)	1079°C (1975°F)/4 hrs./H_2	6920	6840	6180NF	6647
3C	6 w% Y_2O_3 - ZrO_2 Bimodal Distribution Angular Powder	1079°C (1975°F)/4 hrs./H_2	1540	1050	2380	1657
3D	6 w% Y_2O_3 - ZrO_2 (See Mod. 3C) Media Surface Finished	1079°C (1975°F)/4 hrs./H_2	1670	1790	2110	1857
8A	6 w% Y_2O_3 - ZrO_2 (See Mod. 3C) 2.5 cm (1 inch) Gun-Specimen Distance	1079°C (1975°F)/4 hrs./H_2	7830	6520	6180	6843
8B	6 w% Y_2O_3 - ZrO_2 (See Mod. 3C) 5.1 cm (2 inch) Gun-to-Specimen Distance	1079°C (1975°F)/4 hrs./H_2	5310	5450	6180	5646
8C	6 w% Y_2O_3 - ZrO_2 (See Mod. 3C) High Energy Gun	1079°C (1975°F)/4 hrs./H_2	200	200	200	200
8D	6 w% Y_2O_3 - ZrO_2 (See Mod. 3C) Post Coating Plasma Surface Treatment	1079°C (1975°F)/4 hrs./H_2	1740	600	2040	1460
13A	6 w% Y_2O_3 - ZrO_2 (See Mod. 3C)	1079°C (1975°F)/4 hrs./H_2 + Water Quench From 982°C (1800°F) to Room Temp.	3240	3240	1690	2723
13B	6 w% Y_2O_3 - ZrO_2 (See Mod. 3C)	1079°C (1975°F)/4 hrs./H_2 + Water Quench From 1079°C (1975°F) to Room Temp.	2090	1050	930	1357
13C	6 w% Y_2O_3 - ZrO_2 (See Mod. 3C)	1079°C (1975°F)/4 hrs./H_2 + Tin Quench From 982°C (1800°F) to 221°C (430°F)	1050	2090	2990	2043
13D	6 w% Y_2O_3 - ZrO_2 (See Mod. 3C)	1079°C (1975°F)/4 hrs./H_2 + Tin Quench From 1121°C (2050°F) to 221°C (430°F)	4800	2090	1400	2763
16B	6 w% Y_2O_3 - ZrO_2 EB-PVD	871 °C (1600°F)/4 hrs./Air	5770	8330NF	6340NF	6813
16C	12 w% Y_2O_3 - ZrO_2 EB-PVD	871 °C (1600°F)/4 hrs./Air	5640	6590NF	7630NF	6620
16D	23 w% CeO_2 - ZrO_2 EB-PVD	871 °C (1600°F)/4 hrs./Air	4940	5070	6460NF	5490

(1) NF: No Coating Failure - Testing Discontinued

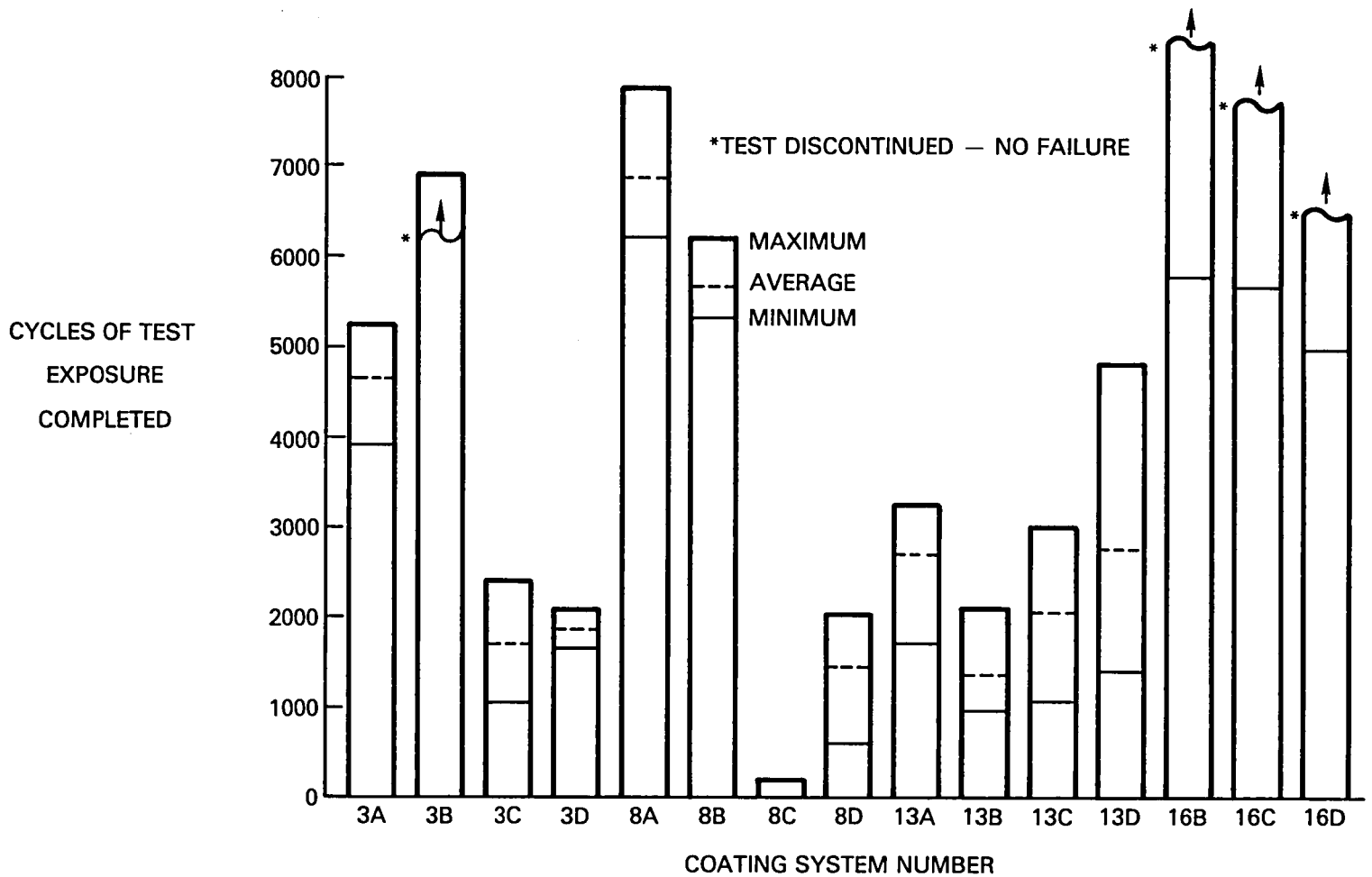

Figure 4-17 Thermal Cycle Test Exposure of Task II Experimental Thermal Barrier Coating Systems

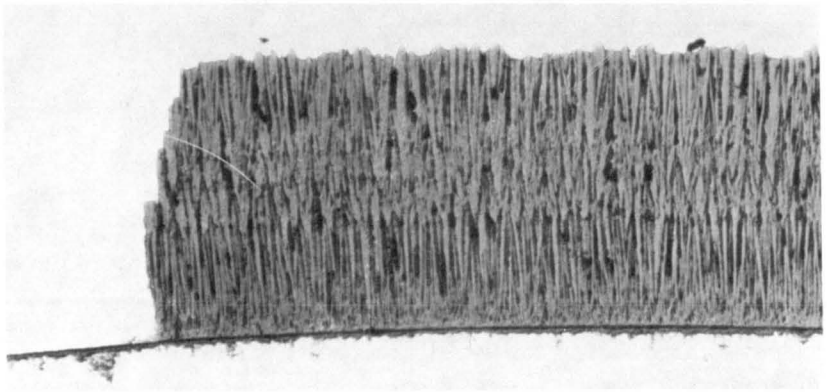

150X

Figure 4-18 Post-test microstructure of 23 w% CeO_2-ZrO_2 coating system modification 16D following 5070 cycles of test exposure, showing failure of the ceramic at the ZrO_2/Al_2O_3 interface

The trend toward decreasing tetragonal phase, stabilizing in the 32 to 42 percent range, is different from that seen for the same plasma sprayed 6 w% Y_2O_3- ZrO_2 ceramic composition tested in Task I, where the percentage of tetragonal phase increased to values between 71 and 87 percent during exposure (Table 3-III). This difference is not understood.

As in Task I, behavior of the EB coatings was different from the plasma coatings. Both the Y_2O_3 stabilized compositions were 100 percent cubic after exposure. The CeO_2 stabilized composition, which was 100 percent tetragonal as deposited, was converted to 70 percent cubic after the test.

Evaluation of the post-test microstructures indicated ceramic failure mechanisms similar to those observed in Task I. As illustrated, for example, in Figure 4-1C, the plasma coatings tend to fail by propagation of cracks parallel and adjacent to, but not co-incident with, the metal-ceramic interface. Electron beam coatings, on the other hand, appear to fail at the interface between the ceramic and the oxide scale formed on the surface of the MCrAlY layer (Figure 4-1B). As shown in Figures 4-1E and 4-13E, significant oxide scale grows at the metal-ceramic interface of both plasma and EB deposited coatings during cyclic elevated temperature exposure. In the case of the EB ceramic, failure resulting from thermal cycling occurs at the interface between the ceramic and the oxide scale. It is not clear whether this interface represents a weak point in the coating system or is the location of highest thermal stress generated as a result of the thermal cycling. The situation for plasma ceramic coatings is even less clear. Cyclic failure of this ceramic occurs near, but not coincident with, the ceramic-oxide scale interface. Whether the growth of the oxide scale influences the state of stress in, and thus the failure life of, the ceramic is not understood at present. Additional experimental effort is clearly required to separate these two effects.

Densification was observed in the plasma sprayed ceramics having a high initial level of porosity; the best example is coating system 3B, coarse spherical powder, shown in Figure 4-2. Relatively little densification was observed in ceramic coatings having lower pre-test levels of porosity such as coating systems 8A and B (Figure 4-5 and 4-6), or cyclic thermal rig tested for short times, such as system 8C (Figure 4-7).

Coating system 3B, coarse spherical powder, was superior to other system 3 coatings; this may be attributed to the strain-relief derived from the high level of porosity in the ceramic as shown in Table 4-IV and Figure 4-2. Coating systems 3C and D appeared to be too dense and were deficient in microcracking and segmentation cracking while 3A was less dense and exhibited a moderate level of strain-relief features (Figures 4-1, 4-4 and 4-5).

The best performing high energy input coating was system 8A (2.5 cm (1 inch) gun-to-specimen distance) which had a high concentration of segmentation cracking as indicated in Table 4-IV and Figure 4-5. The 5.1 cm (2 inch) gun-to-specimen distance, coating system 8B, also performed well with 5646 cycles to failure average. It exhibited a moderate-high level of segmentation cracking as shown in Table 4-IV and Figure 4-6. Although coating systems 8C and D, high energy gun spray and post coating plasma treatment, had moderate

levels of segmentation cracking (Table 4-IV and Figures 4-7 and 4-8, respectively), the specimen substrates in each system were unavoidably overheated (427°C (800°F)) during coating processing. This overheating is thought to be responsible for relatively early failure of those coatings in cyclic thermal testing. Figure 4-7C shows a residual portion of post-tested coating system 8C after complete spallation of the ceramic coating.

Although the thermal-shock coatings (system 13A-D) exhibited moderate-to-high levels of strain-relief features (Table 4-IV and Figures 4-9 through 4-12), the overall performance of these coatings was less than expected. As in the case with coating 3C and D, these system 13 coatings were all relatively dense, which is thought to have had a negative effect on the coating test lives; a minimum level of porosity apparently is required to prevent the catastrophic growth of in-plane cracks.

The system 16 coatings (EB-PVD 6 w% Y_2O_3 - ZrO_2, 12 w% Y_2O_3 - ZrO_2, and 23 w% CeO_2 - ZrO_2) generally exhibited long thermal cycle rig test lives which correlated well with the strain tolerance due to micro-segmentation which is inherent in these coatings (Table 4-IV and Figures 4-13 through 4-16).

In summary, the performances of the Task II coating systems generally are consistent with the amount and kinds of strain-relief features observed in the test specimens (Table IV) with the exception of the system 13 coatings which exhibited moderate-to-high amounts of segmentation-cracking, microcracking, and porosity, but performed relatively poorly.

4.5 SELECTION OF COATINGS FOR TASK III EVALUATION

The four coating/process systems listed in Table 4-VI were selected for evaluation in Task III. These coatings represent one selection from each of the four generically different process approaches evaluated in the first two tasks. Coating systems 3B and 8A were selected on the basis of their excellent burner rig test results in Task II. While the post plasma spray thermal shock system evaluated in Task II provided somewhat disappointing burner rig results, the good performance of Task I coating system 13, which was processed through a tin quench from 1079°C to 221°C (1975°F to 430°F), prompted the decision to reevaluate this processing concept in Task III. In an effort to combine processing benefits with the benefits provided by the coarse spherical powder used to produce Task II coating 3B, this powder was chosen for Task III evaluation of the high energy input spray (system 8A) and post plasma spray thermal shock (system 13) processes in Task III. Selection of the EB-PVD applied system as the fourth coating to be evaluated was based on the outstanding burner rig performance observed in Tasks I and II. The 6 w% Y_2O_3 - ZrO_2 ceramic was selected for the EB-PVD coating to eliminate composition as a variable in the Task III evaluation.

TABLE 4-VI

COATING/PROCESS SYSTEMS SELECTED FOR TASK III EVALUATION(1)

Coating System Number	Ceramic Coating Type	Ceramic Layer	Modification
3	Controlled Substrate Temperature Plasma Spray Process	6 w% Y_2O_3 - ZrO_2	Coarse Spherical Powder (45% + 325 Mesh)
8	High Energy Input Plasma Spray Process	6 w% Y_2O_3 - ZrO_2	Coarse Spherical Powder (45% + 325 Mesh) 2.5 cm (1 inch) Gun-to-Specimen Distance
13	Post Plasma Spray Thermal Shock	6 w% Y_2O_3 - ZrO_2	Coarse Spherical Powder (45% + 325 Mesh) Tin Quench from 1079°C (1975°F) to 221°C (430°F)
16	Micro-Segmented	Electron Beam Physical Vapor Deposited Ceramic	6 w% Y_2O_3 - ZrO_2

(1) = Plasma Deposited Ceramic Bond Coat Applied by Low Pressure Chamber Spray Using the Parameters Identified in Table 3-IID. EB Ceramic Was Deposited over EB Bond Coat.

5.0 TASK III - COATING DURABILITY

The objective of this task was to evaluate each of the four coating systems selected at the end of Task II using test conditions which more realistically simulate gas turbine operating conditions, and to select the best two systems for engine evaluation in Task IV.

5.1 SPECIMEN PREPARATION AND EVALUATION

Procedures and equipment used to fabricate the four ceramic coating systems evaluated in this task (Table 4-VI) were the same as those used to prepare corresponding coatings in Tasks I and II. The three plasma sprayed ceramic coatings were applied over low pressure chamber sprayed metallic coatings. The EB-PVD ceramic was deposited over EB-PVD metallic. As in prior tasks coatings were examined metallographically and by X ray diffraction prior to and after testing.

Results of pre- and post-test x-ray diffraction phase analyses on the Task III coatings are presented in Table 5-I. As in prior tasks, the predominant phase observed in as-deposited plasma sprayed 6 w% Y_2O_3 - ZrO_2 ceramics was tetragonal (Table 5-I). The monoclinic content was somewhat higher than seen previously, particularly in system 8. As observed previously, the electron beam coating was deposited (and remained) virtually all cubic.

Pre- and post-test photomicrographs of the four coating systems evaluated in this task are shown in Figures 5-1 through 5-4. The microstructure of coating system 3 is similar to the corresponding Task II structure (system 3B). As shown in Figure 5-1, the system 3 structure contains moderate amounts of porosity and microcracking. Although not shown in Figure 5-1, occasional segmentation cracking also was observed in this coating.

Coating systems 8 and 13 were processed to increase the amount of strain tolerant features such as segmentation and microcracking. As shown in Figure 5-2, this goal was achieved in the system 8 ceramic, which has a high concentration of segmentation cracking coupled with a moderate to high amount of heterogeneously distributed, relatively coarse porosity. However, the structure also contains relatively high amounts of less desirable in-plane cracking, indicating the need for very close process control in the fabrication of this coating. Despite the quenching applied to coating system 13, the structure of this coating (Figure 5-3) is virtually indistinguishable from that of system 3.

As observed previously, the structure of the EB-PVD coating, system 16 (Figure 5-4), consists of extremely fine segments (columns) aligned perpendicular to the plane of the coating.

TABLE 5-I

TASK III X-RAY DIFFRACTION PHASE ANALYSIS OF CERAMIC COATING SURFACE ON CYCLIC OXIDATION RIG TEST SPECIMENS

Coating System Number	Ceramic Coating	Exposure Time (hr) for Post-Test Specimens	Volume Percent Phase Present					
			Cubic ZrO_2		Tetragonal ZrO_2		Monoclinic ZrO_2	
			Pre-Test	Post-Test	Pre-Test	Post-Test	Pre-Test	Post-Test
3	Plasma Sprayed 6 w% Y_2O_3-ZrO_2 Coarse Powder (45% + 325 Mesh)	604	20	25	75	70	8	5
8	Plasma Sprayed 6 w% Y_2O_3-ZrO_2 Coarse Powder (45% + 325 Mesh), 2.5 cm (1 inch) Gun-to-Specimen Distance	459	15	12	70	75	15	13
13	Plasma Sprayed 6 w% Y_2O_3-ZrO_2 Coarse Powder, Tin Quench From 1079°C (1975°F) to 221°C (430°F)	427	28	28	65	67	7	5
16	Electron Beam Physical Vapor Deposited 6 w% Y_2O_3-ZrO_2	645	99(1)	(2)	-	-	-	-

(1) Remainder 1% cubic Y_2O_3

(2) Pattern could not be analyzed quantitatively - appeared to contain both cubic and tetragonal

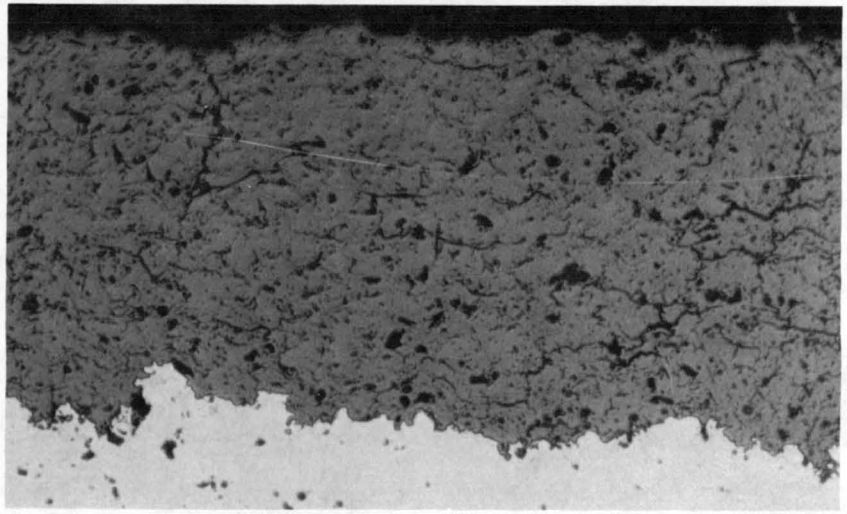

(A) PRE-TEST CONDITION 200X

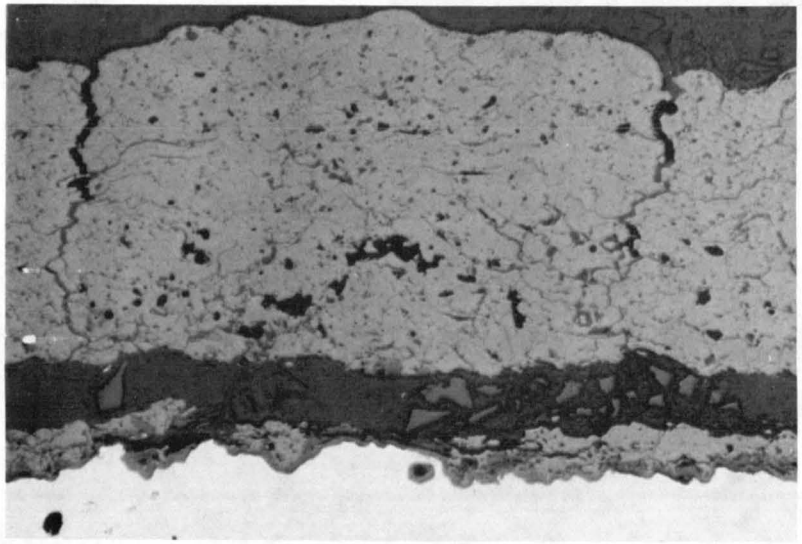

(B) CYCLIC OXIDATION RIG TESTED 200X

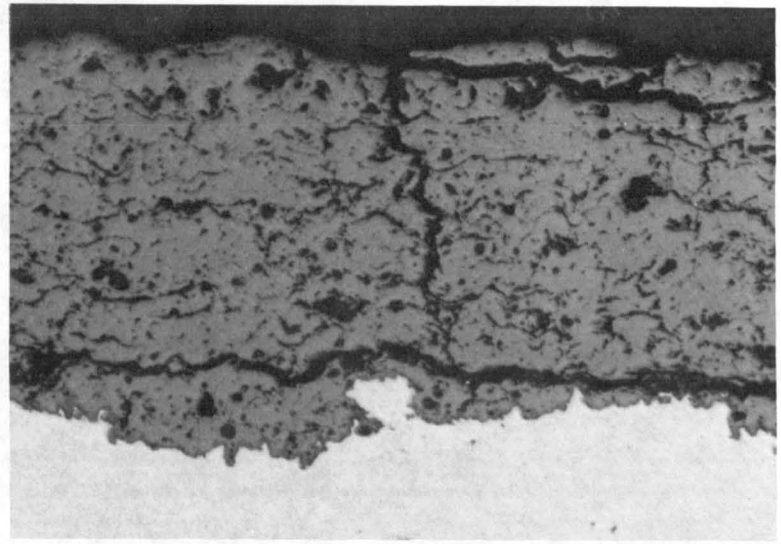

(C) CYCLIC HOT CORROSION RIG TESTED 200X

Figure 5-1 Light photomicrograph of Task III coating system 3 (6 w% Y_2O_3-ZrO_2, baseline system): (a) before test; (b) after 604 hours (cycles) in cyclic oxidation rig test at 1149°C (2100°F) ceramic and 982°C (1800°F) substrate temperature; (c) after 432 cycles/hours in cyclic hot corrosion rig test at 954°C 1750°F) ceramic surface temperature and 899°C (1650°F) substrate temperature.

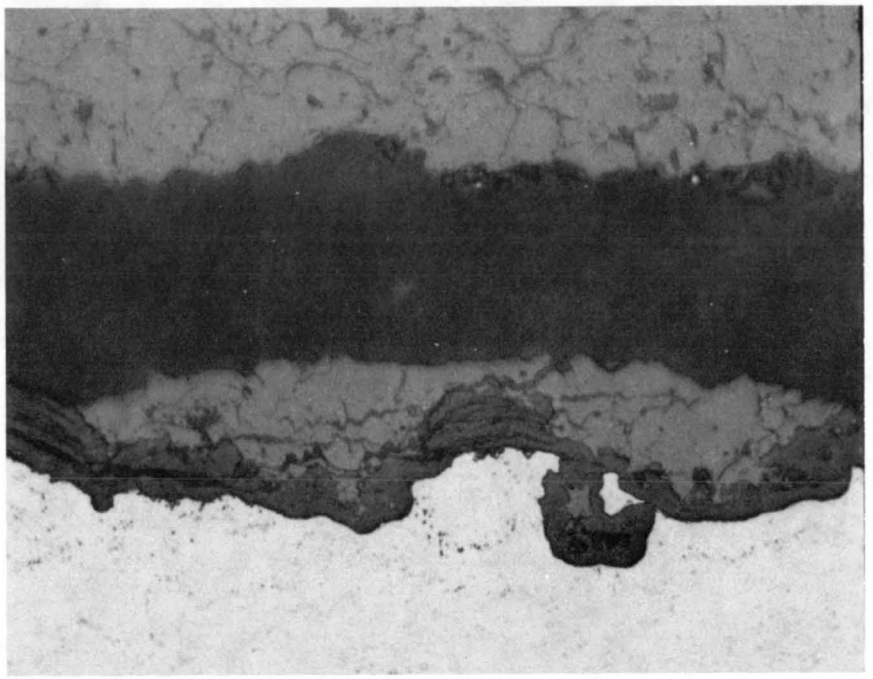

(D) 500X

Figure 5-1 (Continued) Light photomicrograph of Task III coating system 3 (6 w% Y_2O_3-ZrO_2, baseline system) showing oxide scale observed on bond coat surface of cyclic oxidation rig tested specimen.

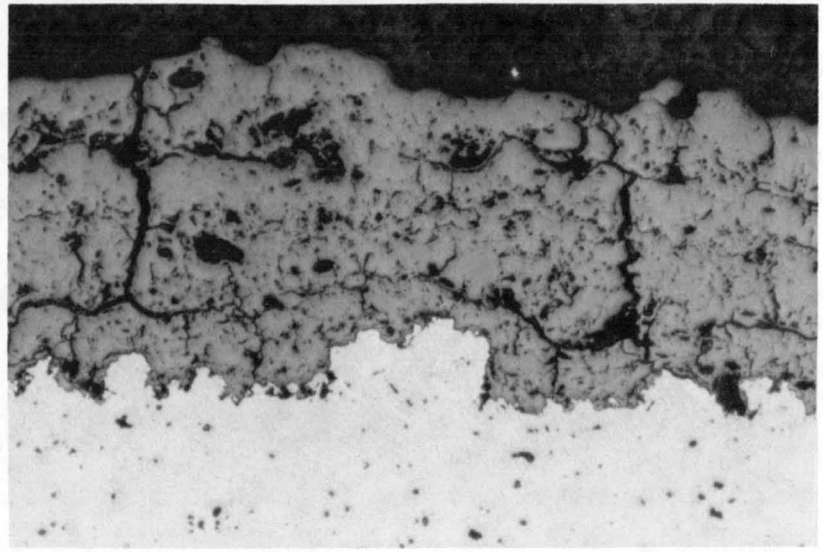

(A) PRE-TEST CONDITION 200X

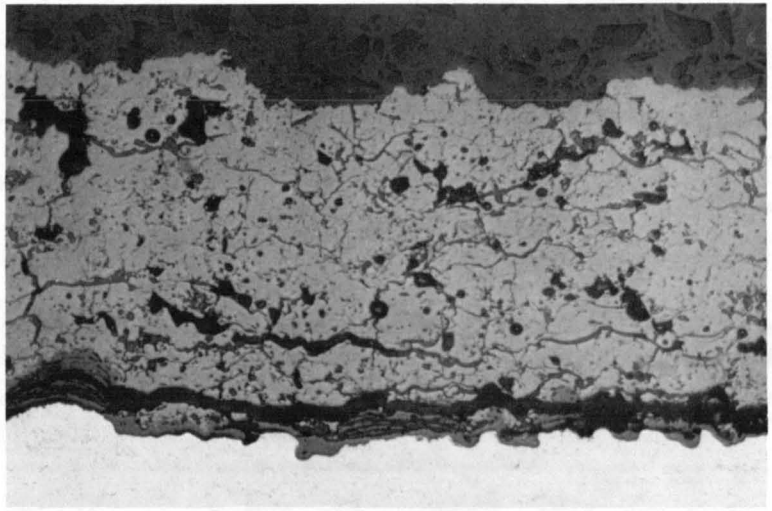

(B) CYCLIC OXIDATION RIG TESTED 200X

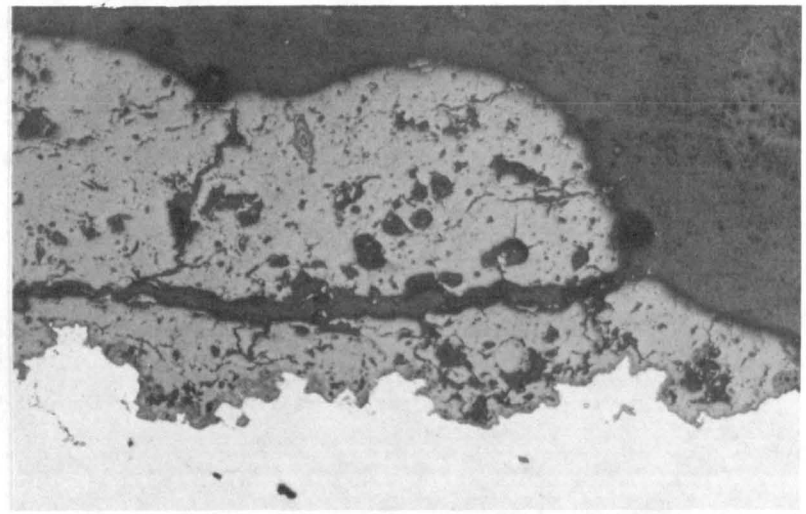

(C) CYCLIC HOT CORROSION RIG TESTED 200X

Figure 5-2 Light photomicrographic of Task III coating system 8 (6 w% Y_2O_3-ZrO_2, one inch gun-to-specimen distance): (a) before test; (b) after 459 hours (cycles) in cyclic oxidation rig test at 1149°C (2100°F) ceramic surface temperature and 982°C (1800°F) metal substrate temperature; (c) after 575 hours (cycles) in cyclic hot corrosion rig test at 954°C (1750°F) ceramic surface temperature and 899°C (1650°F) metal substrate temperature.

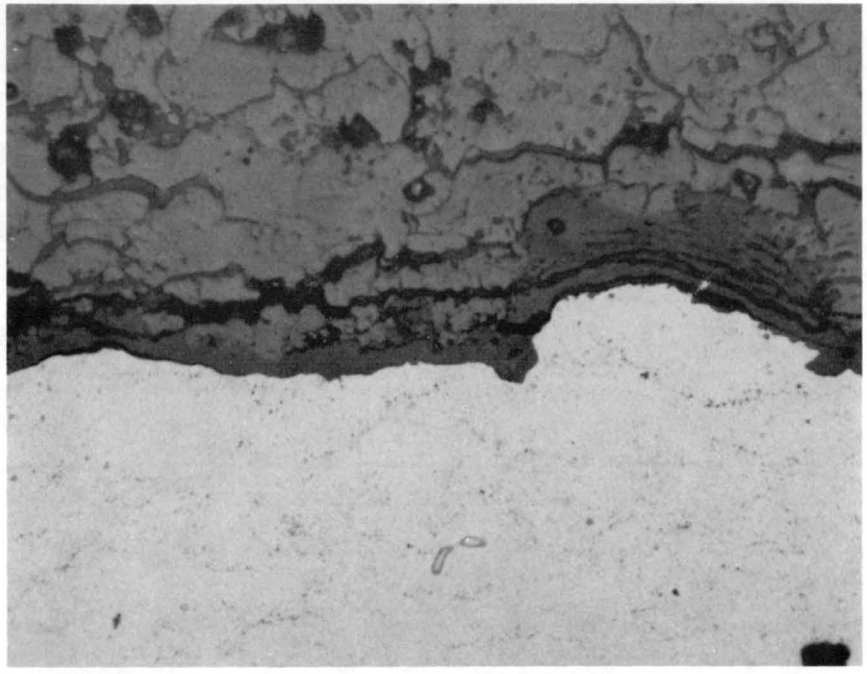

(D) 500X

Figure 5-2 (Continued) Light photomicrographic of Task III coating system 8 (6 w% Y_2O_3-ZrO_2, one inch gun-to-specimen distance) showing oxide scale observed on bond coat surface of cyclic oxidation rig tested specimen.

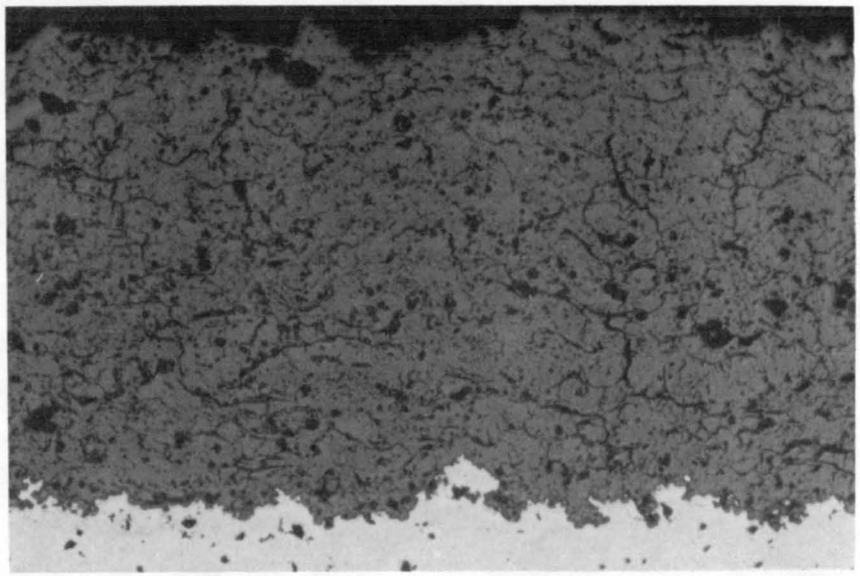

(A) PRE-TEST CONDITION 200X

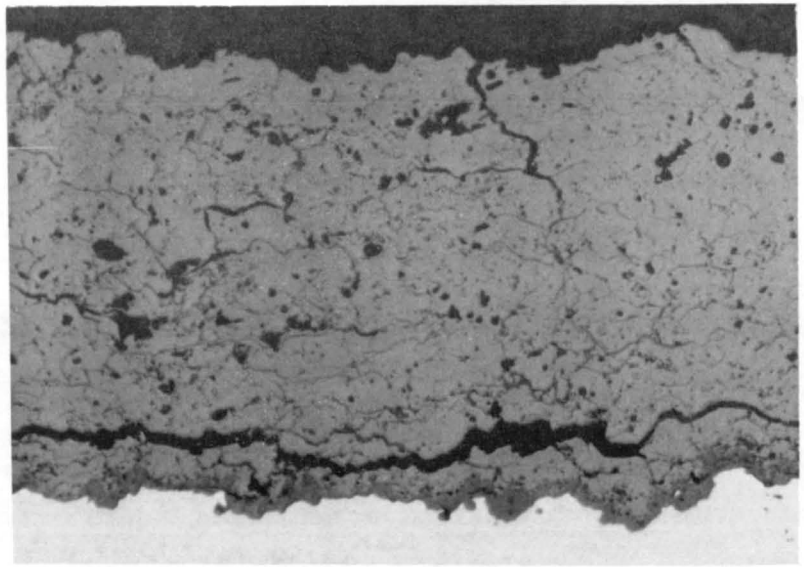

(B) CYCLIC OXIDATION RIG TESTED 200X

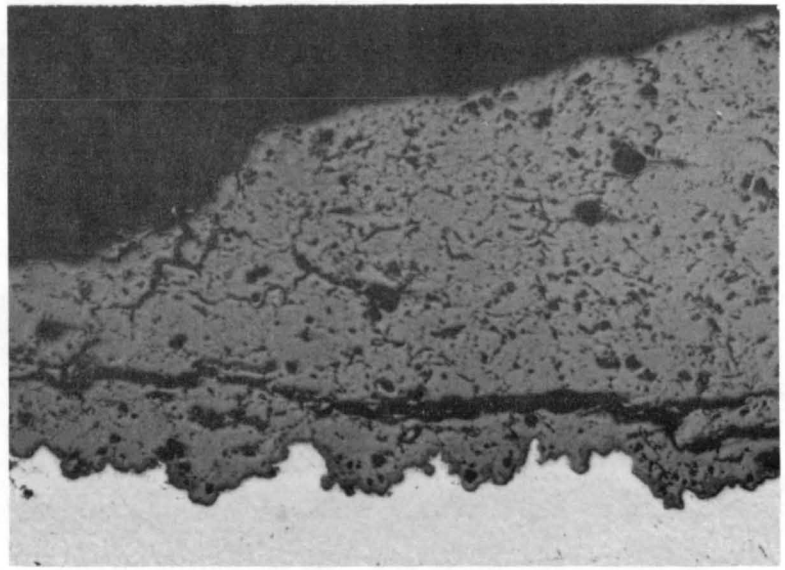

(C) CYCLIC HOT CORROSION RIG TESTED 200X

Figure 5-3 Light photomicrographs of Task III coating system 13 (6 w% Y_2O_3-ZrO_2, liquid tin quenched from 1975°F): (a) before test; (b) after 427 hours (cycles) in cyclic oxidation rig test at 1149°C (2100°F) ceramic surface temperature and 982°C (1800°F) metal substrate temperature; (c) after 453 hours (cycles) in cyclic hot corrosion rig test at 954°C (1750°F) ceramic surface temperature and 899°C (1650°F) metal substrate temperature.

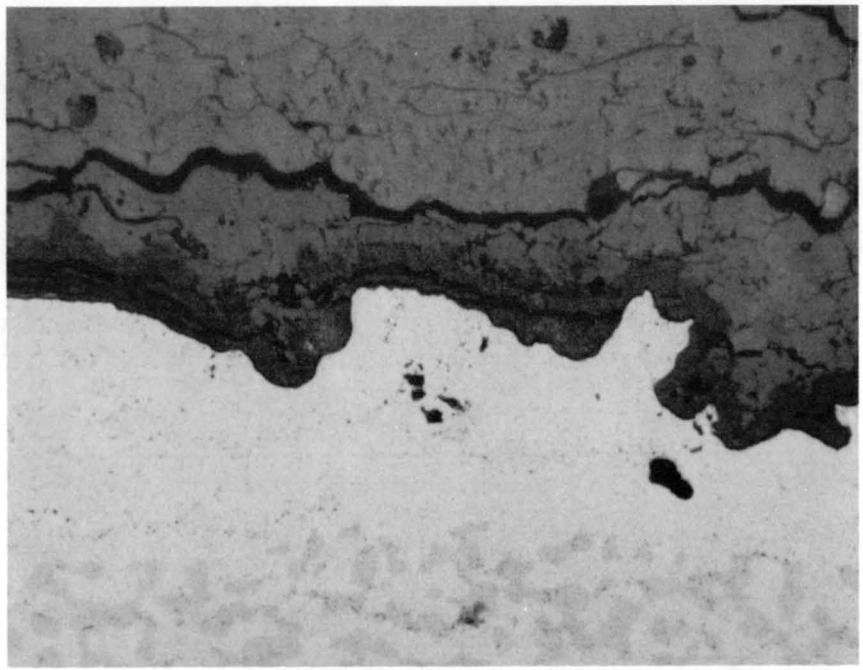

(D) 500X

Figure 5-3 (Continued) Light photomicrographs of Task III coating system 13 (6 w% Y_2O_3-ZrO_2, liquid tin quenched from 1975°F) showing oxide scale observed on bond coat surface of cyclic oxidation rig tested specimen.

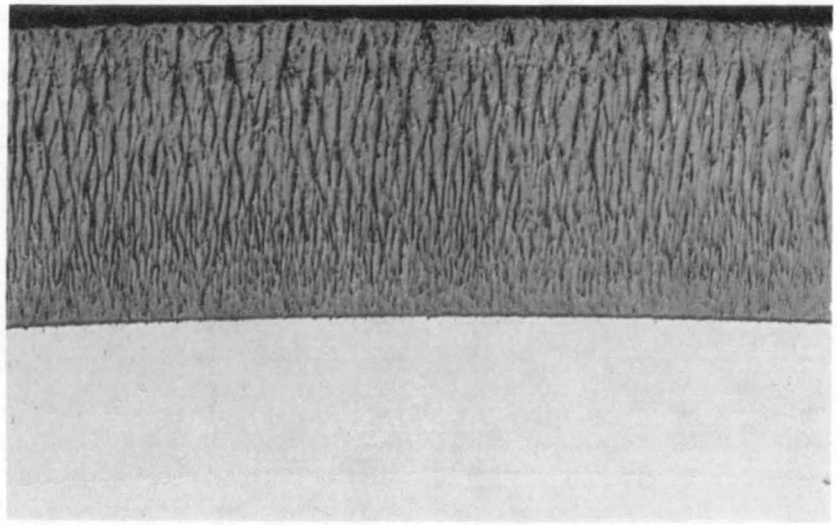

(A) PRE-TEST CONDITION 200X

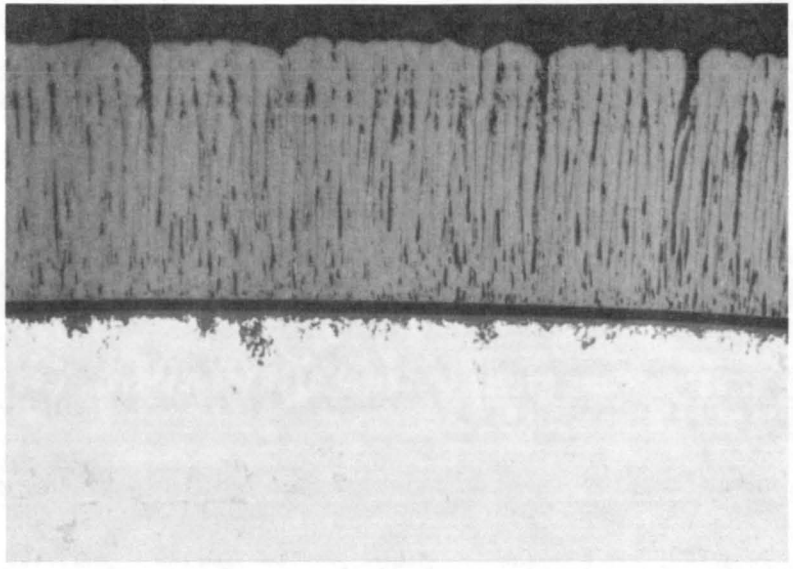

(B) CYCLIC OXIDATION RIG TESTED 200X

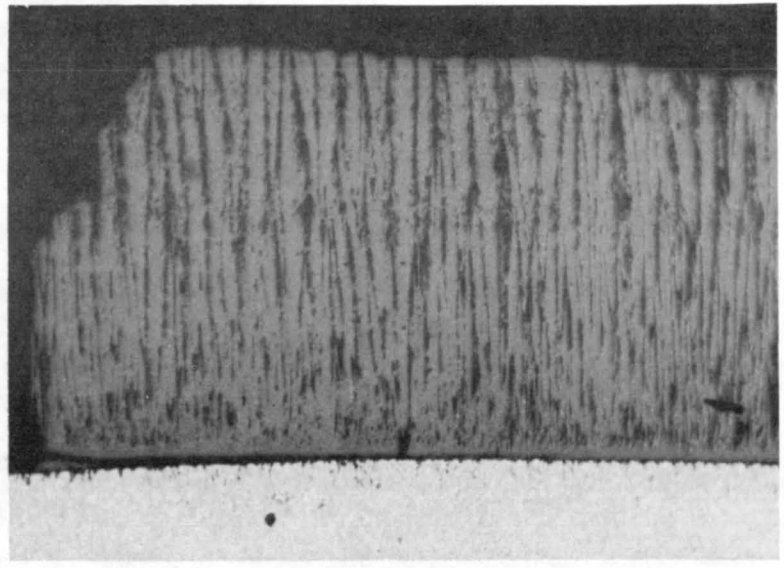

(C) CYCLIC HOT CORROSION RIG TESTED 200X

Figure 5-4 Light photomicrographs of Task III coating system 16 (EB-PVD 6 w% Y_2O_3-ZrO_2): (a) before test; (b) after 645 hours (cycles) in cyclic oxidation rig test at 1149°C (2100°F) ceramic surface temperature and 982°C (1800°F) metal substrate temperature; (c) after 444 hours (cycles) in cyclic hot corrosion rig test at 954°C (1750°F) ceramic surface temperature and 899°C (1650°F) metal substrate temperature.

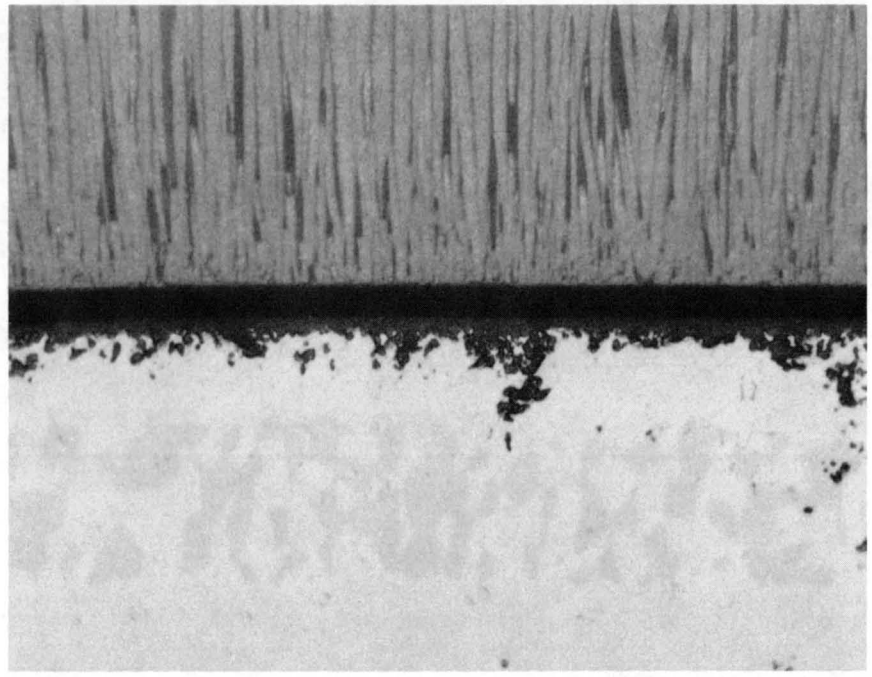

(D) 500X

Figure 5-4 (Continued) Light photomicrographs of Task III coating system 16 (EB-PVD 6 w% Y_2O_3-ZrO_2) showing oxide scale observed on bond coat surface of cyclic oxidation rig tested specimen. (Note gap between MCrAlY oxide and debonded ceramic.)

5.2 CYCLIC OXIDATION RIG TESTING AND EVALUATION

The objective of this testing was to evaluate the cyclic thermal durability of candidate coatings in an environment which more realistically simulates gas turbine engine operating conditions. As in Tasks I and II, tests were conducted in a jet-A fueled burner rig. Key differences between previous tests and the Task III tests were internal cooling of the Task III specimens, which provided a thermal gradient across the ceramic, and the use of a one hour cycle as opposed to the prior six minute cycle. Tests in this task were conducted with a ceramic surface temperature of 1149°C (2100°F) and a substrate temperature of 982°C (1800°F). Each cycle consisted of 57 minutes exposure to the combustion flame, followed by three minutes of compressed air cooling. Details of the test equipment and procedures are provided in Appendix B.

Results of the cyclic oxidation tests conducted on the four Task III coating systems are presented in Table 5-II and Figure 5-5. Because of the differences in test conditions, it is difficult to compare these results with those from prior tasks. When compared on the basis of test time, however, the results for systems 3 and 8 appear to be consistent with those for the corresponding systems 3B and 8A tested in Task II. Based on measured transients, the respective hot time in the Task II and III tests are approximately three minutes and 56 minutes per cycle. Based on these times, total respective average hot times for Task II system 3B and Task III system 3 are approximately 344 and 342 hours. Corresponding respective hot times for Task II system 8A and Task III system 8 are approximately 342 and 396 hours, indicating similar performance of the corresponding Task II and III coating based on total hot exposure time to failure. This observation suggests that thermal exposure (time at temperature) plays a significant role in thermal barrier coating degradation and failure. The relative importance of this factor in relation to cyclic thermal stress effects is not well understood at the present time. For typical aircraft engine applications, these hot times represent about 15,000 hours of engine operation with a typical block time of 1.5 hours.

As expected based on superior performance in Tasks I and II, the best coating in the oxidation test was the system applied by EB-PVD. Both systems 3 and 8 had performances which were only slightly lower than the EB coating, with the poorest performance coating being the quenched ceramic (system 13). The poor performance of this coating as compared to system 3, which had a similar structure (compare Figures 5-1 and 5-3) is not understood.

Post test metallographic and x-ray evaluation indicated very little change of structure or ceramic surface phase distribution after exposure. As illustrated in Figures 5-1B, 5-2B, 5-3B and 5-4B, the ceramic failure mode in the cyclic oxidation test was essentially the same as that observed in the Task I and II rapid cycle tests. The plasma coatings failed by cracking in the ceramic adjacent to the ceramic-metal interface (Figure 5-1B, 5-2B and 5-3B), while the EB coating appeared to fail at the interface between the ceramic and the oxide scale formed on the MCrAlY layer (Figure 5-4B). The post test ceramic structures seen in Figures 5-1 through 5-4 are not significantly different

TABLE 5-II

TASK III CYCLIC OXIDATION RIG TEST RESULTS
(1149°C; 2100°F Ceramic, 982°C; 1800°F metal substrate/57 min.
+ forced air cool/3 min.)

Coating System Number	Ceramic Coating	Number of Hours to Failure				
		Bar 1	Bar 2	Bar 3	Bar 4	Avg.
3	Plasma Sprayed 6 w% Y_2O_3-ZrO_2 Coarse Powder (45% + 325 Mesh)	147	344	367	604	366
8	Plasma Sprayed 6 w% Y_2O_3-ZrO_2 Coarse Spherical Powder (45% + 325 Mesh), 2.5 cm (1 inch) Gun-to-Specimen Distance	272	381	459	584	424
13	Plasma Sprayed 6 w% Y_2O_3-ZrO_2 Coarse Spherical Powder (45% + 325 Mesh), Tin Quench from 1079°C 1975°F) to 221°C (430°F)	79	175	417	427	274
16	Electron Beam Physical Vapor Deposited 6 w% Y_2O_3-ZrO_2	272	645	523	584	506

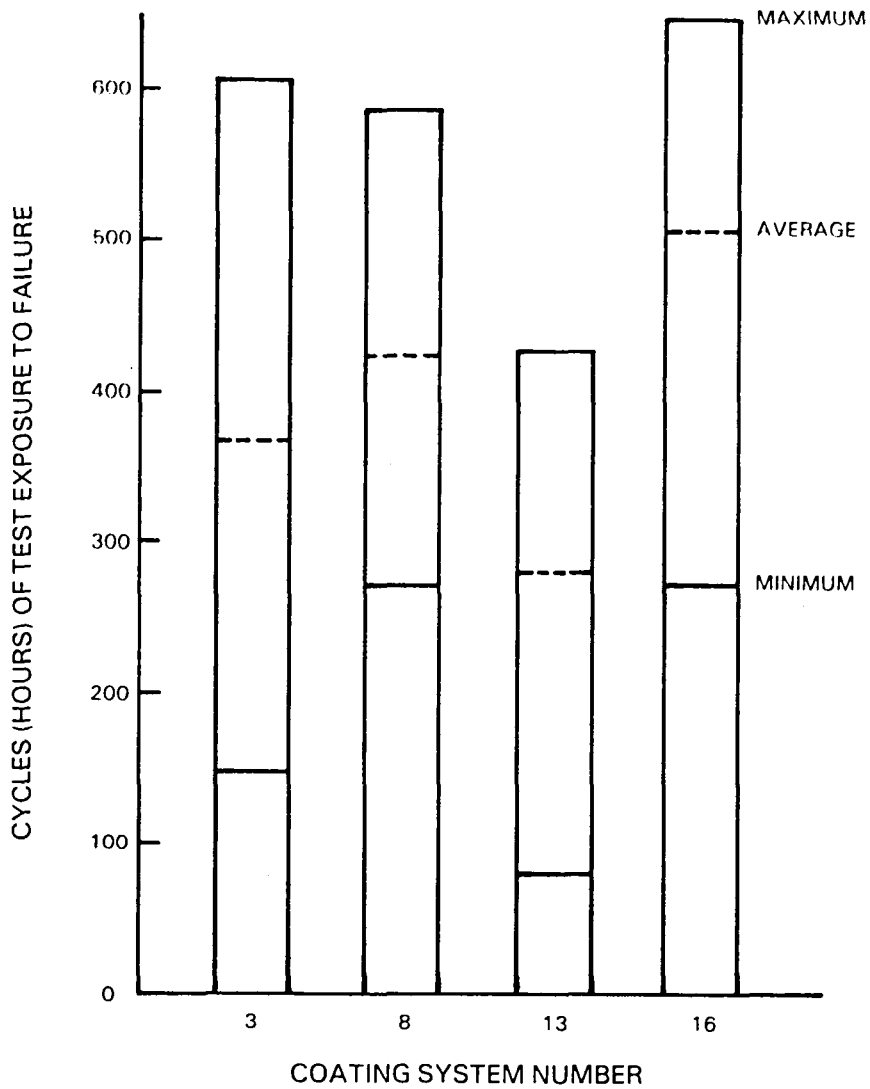

Figure 5-5 Task III Cyclic Oxidation Rig Test Results

from the corresponding pre-test structures shown in the same figures, indicating, at least for this test, ceramic sintering is not a significant factor in coating degradation. Except for the EB coating (system 16), post test x-ray diffraction results are, within the range of experimental error, virtually identical to pre-test results (Table 5-I). The x-ray diffraction pattern for the electron beam deposited coating appeared to contain both cubic and tetragonal peaks, but could not be analyzed quantitatively. These results suggest that, as opposed to the rapid cycle test where significant structural and phase changes were seen, the ceramic remains relatively "inert" during the cyclic oxidation exposure. Two factors may contribute to this difference of behavior. First, while the surface temperature is higher, the average ceramic temperature is lower in the cyclic oxidation than in the rapid cycle test. Second, the number of strain cycles experienced in the oxidation test is smaller by at least an order of magnitude. This may contribute to reduced transformation in a system which is known to be susceptible to strain induced phase transformation. Despite the lower metal temperature (compared with Task I and Task II rapid cycle tests), significant MCrAlY surface oxidation was observed under the ceramic layer (see Figures 5-1D, 5-2D, 5-3D, and 5-4D). As indicated previously, the relative importance of this oxide scale growth, and of other possible thermal exposure effects (such as sintering or phase changes) versus stress induced by thermal cycling as causal factors in ceramic coating failure is not well understood at the present time.

5.3 CYCLIC HOT CORROSION RIG TESTING AND EVALUATION

The objective of this testing was to evaluate the cyclic durability of candidate coatings in an environment which simulates typical aircraft gas turbine hot corrosion conditions. To accomplish this objective, burner rig tests were conducted with 30.5 liters/hr SO_2 (which converts to SO_3 during combustion) and 20 ppm synthetic sea salt (ASTM D-1141-52) added to the burner primary air supply. Initial trials were conducted at a ceramic surface temperature of 982°C (1800°F); however; detailed analysis of the specimen surface indicated no salt deposition was occurring. To achieve salt deposition, the ceramic surface temperature was reduced. The specimens were exposed to a ceramic surface temperature of 954°C (1750°F) and an inner diameter metal temperature of 899°C (1650°F) for 57 minutes in a ducted rig, followed by three minute cooling with a blast of compressed air at ambient pressure. Details of the test methods are provided in Appendix C.

Results of the cyclic hot corrosion tests are presented in Table 5-III and Figure 5-6. With the exception of coating system 8 (2.56 cm (1 inch) gun-to-specimen distance), these results are grouped closely at about 425 hours. Experience with metallic coating systems indicates that with the levels of salt and sulfur utilized for this testing, metallic coating rig lives are less than typical service lives by factors in the range of 2 to 5X. However, not enough is currently known about life prediction of ceramic coating performance from laboratory data to quantitatively predict airfoil coating life from these data.

Post test photomicrographs (Figures 5-1 through 5-4) show some change in the ceramic failure mode under hot corrosion conditions. While the predominant failure mode continues to involve cracking of the ceramic just above the

TABLE 5-III

TASK III CYCLIC HOT CORROSION RIG TEST RESULTS
(954°F; 1750°F Ceramic, 899°C; 1650°F Metal Substrate/57 min. + Forced Air Cool/3 min.)

Coating System Number	Ceramic Coating	Number of Hours/Cycles Accumulated				
		Bar 1 (1)	Bar 2	Bar 3	Bar 4	Avg.
3	Plasma Sprayed 6 w% Y_2O_3-ZrO_2 Coarse Spherical Powder (45% + 325 Mesh)	162-R	316-F	432-F	514-R	>421
8	Plasma Sprayed 6 w% Y_2O_3-ZrO_2 Coarse Spherical Powder (45% + 325 Mesh), 2.5 cm (1 inch) Gun-to-Specimen Distance	162-R	510-F	575-F	732-F	606
13	Plasma Sprayed 6 w% Y_2O_3-ZrO_2 Coarse Spherical Powder, Tin Quench From 1079°C (1975°F) to 221°C (430°F)	162-R	359-F	453-F	473-F	428
16	Electron Beam Physical Vapor Deposited 6 w% Y_2O_3-ZrO_2	162-R	72-F	444-F	789-F**	435

R - No failure/specimen removed from test for evaluation

F - Specimen removed from test due to spallation failure of ceramic coating.

F** - Removed from test due to corrosion of the specimen originating at the uncoated tip.

(1) - Removed at 162 hours for destructive examination - not included in average.

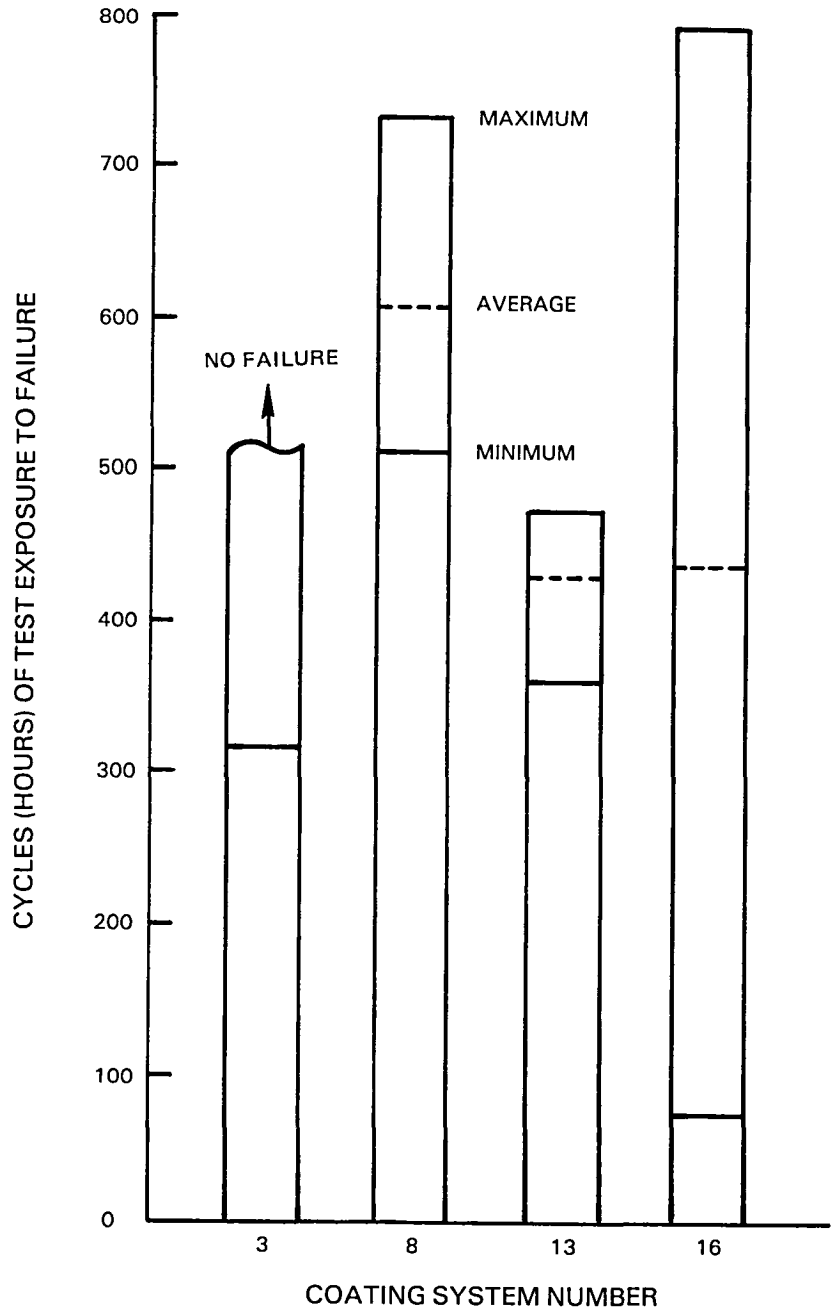

Figure 5-6 Task III Cyclic Hot Corrosion Rig Test Results

metal-ceramic interface, additional spalling of the ceramic in the outer layers also is seen. (See Figure 5-3C, for example). This observation supports the previously published hypothesis (Reference 21) that ceramic hot corrosion failure results from alternate freezing and thawing of corrodents which deposit in liquid form and infiltrate the ceramic. X-ray diffraction patterns obtained from remnant ceramic surfaces on failed specimens indicated the presence of various corrosion species (Table 5-IV). As shown in Figures 5-7 through 5-10, x-ray intensity maps indicate substantial infiltration of Na, Mg, and S in all four candidate ceramics. Surprisingly, the system 8 coating, which provided the best resistance to corrosion induced spallation, appears to have as much or more infiltrated corrodent than the other three coatings (see Figure 5-8).

5.4 SELECTION OF COATINGS FOR FUTURE ENGINE EVALUATION

Based on cyclic thermal spall results obtained in Tasks I and II and on the cyclic oxidation and hot corrosion results obtained in Task III, the two coating/process systems listed in Table 5-V were selected for future evaluation in Task IV. These systems were selected to provide a good balance of cyclic oxidation, hot corrosion and thermal spall performance. While performance of the EB-PVD system was outstanding in all tests except cyclic hot corrosion, this coating was not considered a candidate for Task IV evaluation because reproducible process methods for application to complex geometry turbine components have not yet been demonstrated.

TABLE 5-IV

TASK III XRD PHASE ANALYSIS
OF CYCLIC HOT CORROSION RIG TESTED SPECIMENS (VOLUME PERCENT)

Coating System Number	Exposure Time (hr) and Analyzed Bar	Cubic ZrO_2	Tetragonal ZrO_2	Monoclinic ZrO_2	Other
3	316	13%	65%	7%	10% NiO, S (v/o undetermined)
8	732	--	minor	trace	major (Ni, Fe) Cr_2O_4 major Fe_2O_3 minor $(0.4Na_2O\ 0.1CaO)_2SO_4$ trace NiO
13	473	trace	trace	--	major NiO major $(0.4Na_2O\ 0.1CaO)_2SO_4$ minor (Ni, Fe) Cr_2O_4
16	789	trace	trace	--	major (Ni, Fe) Cr_2O_4 minor NiO trace $(0.4Na_2O\ 0.1CaO)_2SO_4$

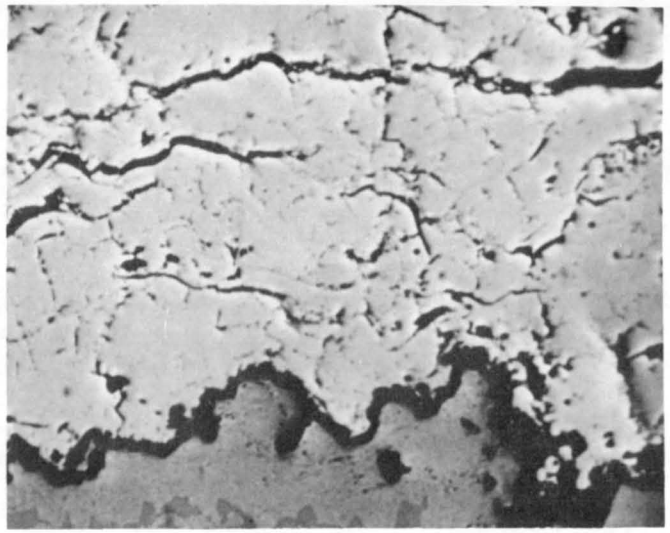

800X

(A) BACKSCATTERED ELECTRON IMAGE

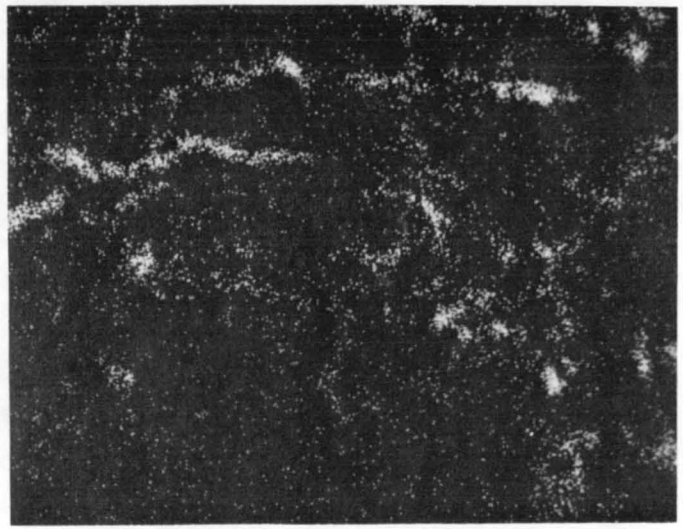

800X

(B) SULFUR X-RAY IMAGE

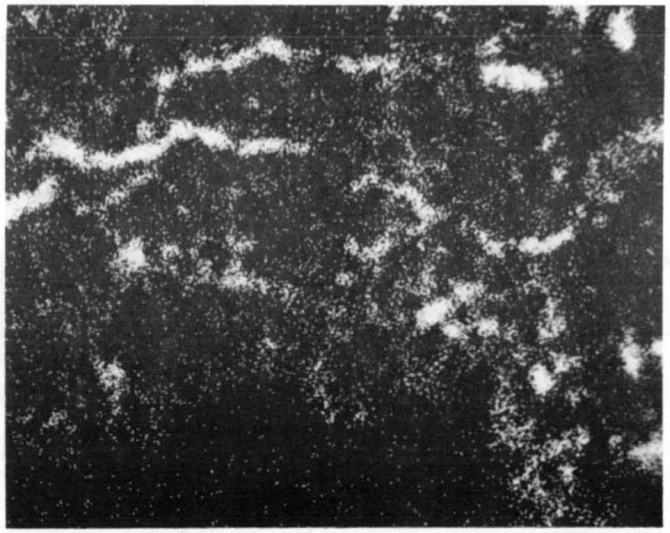

800X

(C) SODIUM X-RAY IMAGE

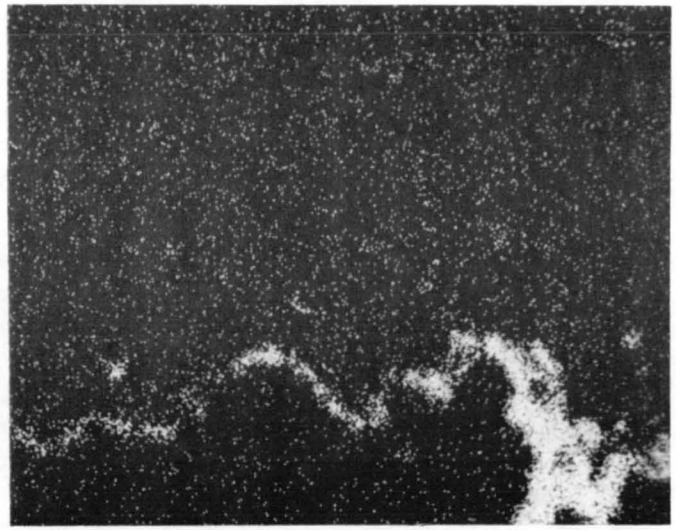

800X

(D) MAGNESIUM X-RAY IMAGE

Figure 5-7 Backscattered electron image photomicrograph (a) and x-ray image photographs showing the distribution of sulfur, sodium, and magnesium (b-d, respectively) in Task III coating system three (6 w% Y_2O_3-ZrO_2, baseline system) after 432 hours (cycles) of cyclic hot corrosion rig testing at 954°C (1750°F) ceramic surface temperature and 899°C (1650°F) metal substrate temperature.

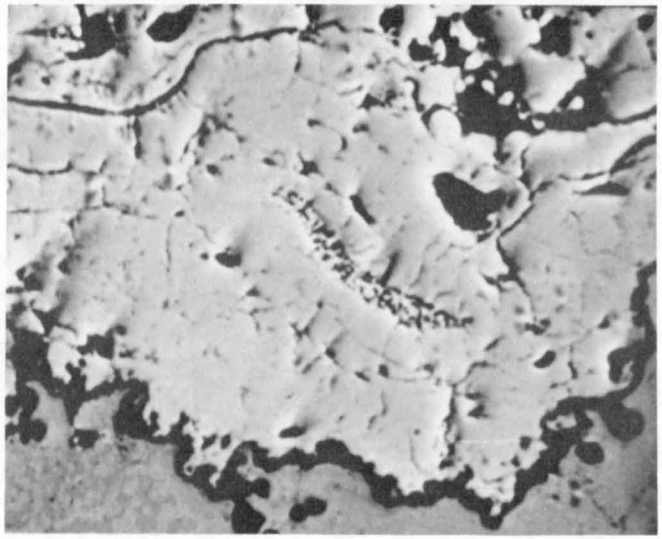

800X

(A) BACKSCATTERED ELECTRON IMAGE

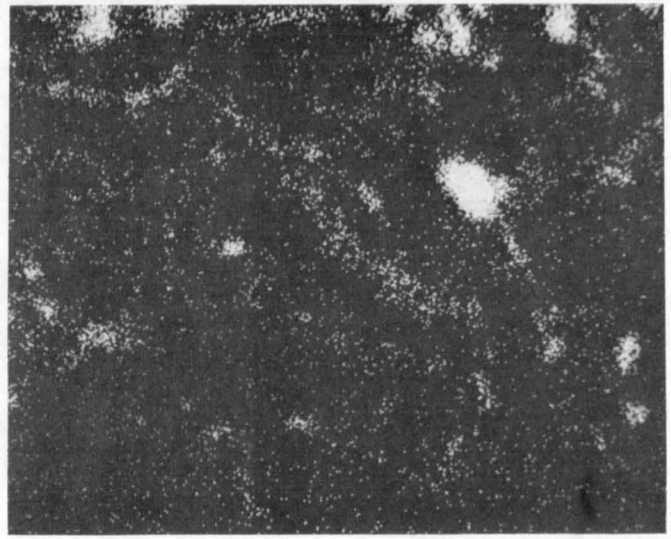

800X

(B) SULFUR X-RAY IMAGE

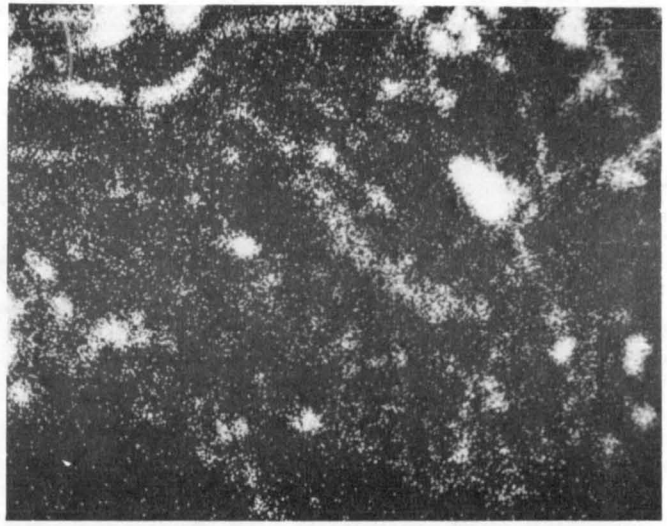

800X

(C) SODIUM X-RAY IMAGE

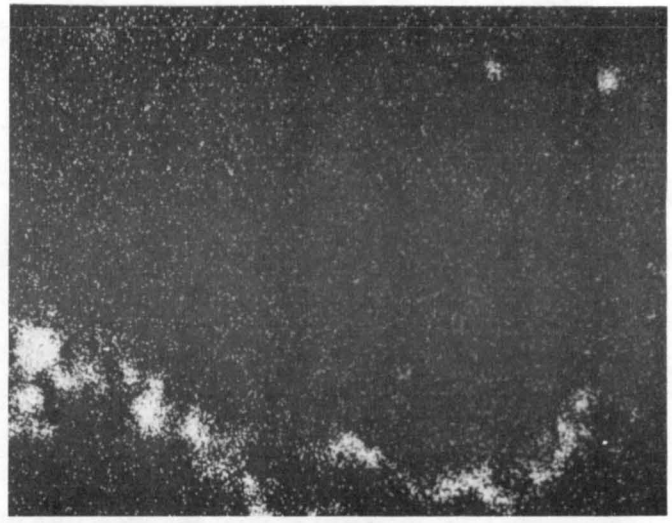

800X

(D) MAGNESIUM X-RAY IMAGE

Figure 5-8 Backscattered electron image photograph (a) and x-ray image photographs showing the distribution of sulfur, sodium, and magnesium (b-d, respectively) in Task III coating system eight (6 w% Y_2O_3-ZrO_2, one inch gun-to-specimen distance) after 575 hours (cycles) of cyclic hot corrosion rig testing at 954°C (1750°F) ceramic surface temperature and 899°C (1650°F) metal substrate temperature.

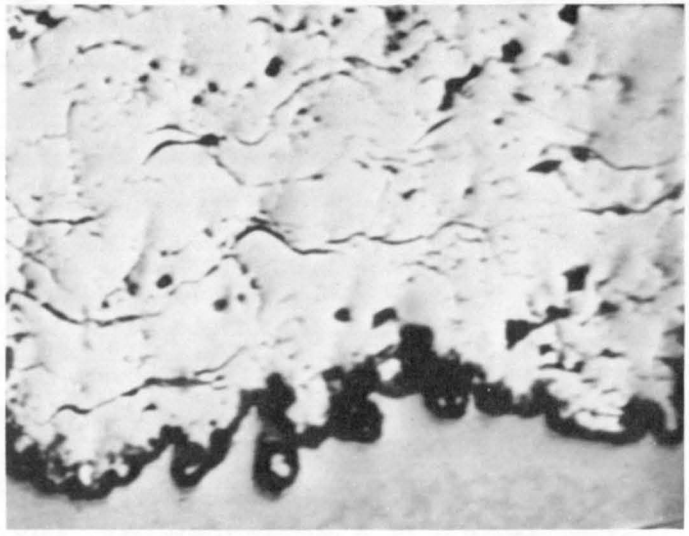

800X

(A) BACKSCATTERED ELECTRON IMAGE

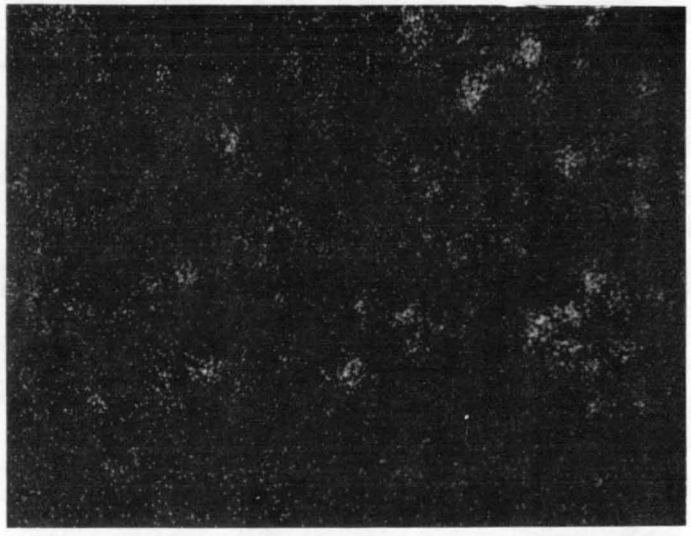

800X

(B) SULFUR X-RAY IMAGE

800X

(C) SODIUM X-RAY IMAGE

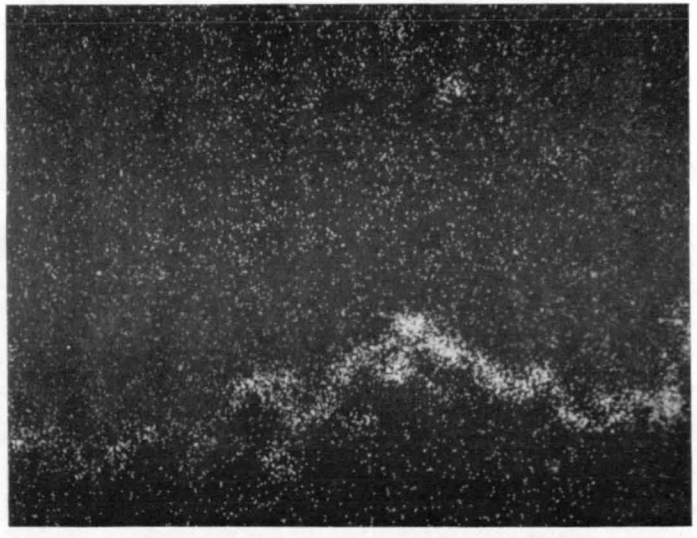

800X

(D) MAGNESIUM X-RAY IMAGE

Figure 5-9 Backscattered electron image photograph (a) and x-ray image photographs showing the distribution of sulfur, sodium, and magnesium (b-d, respectively) in Task III coating system 13 (6 w% Y_2O_3-ZrO_2, liquid tin quenched from 1975°F) after 453 hours (cycles) of cyclic hot corrosion rig testing at 954°C (1750°F) ceramic surface temperature and 899°C (1650°F) metal substrate temperature.

800X

(A) BACKSCATTERED ELECTRON IMAGE

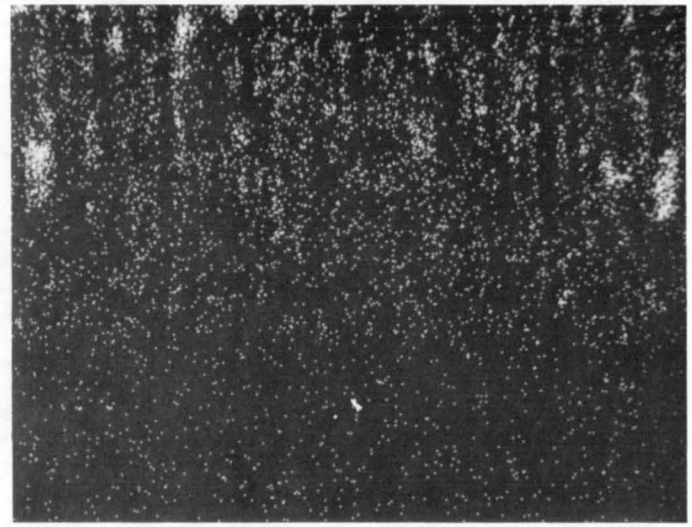

800X

(B) SULFUR X-RAY IMAGE

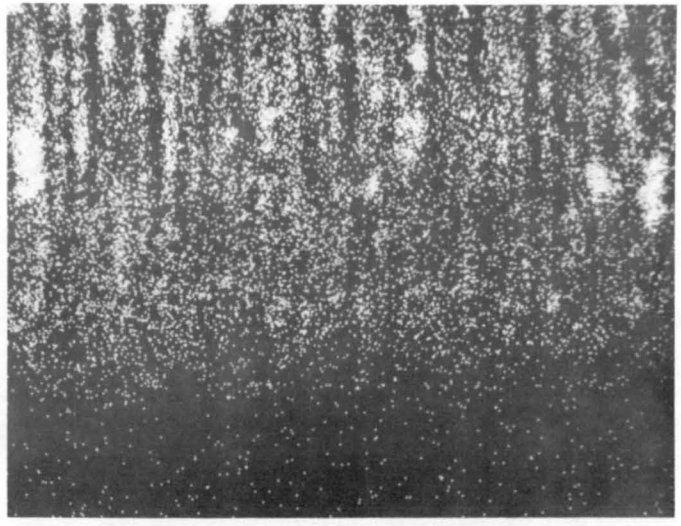

800X

(C) SODIUM X-RAY IMAGE

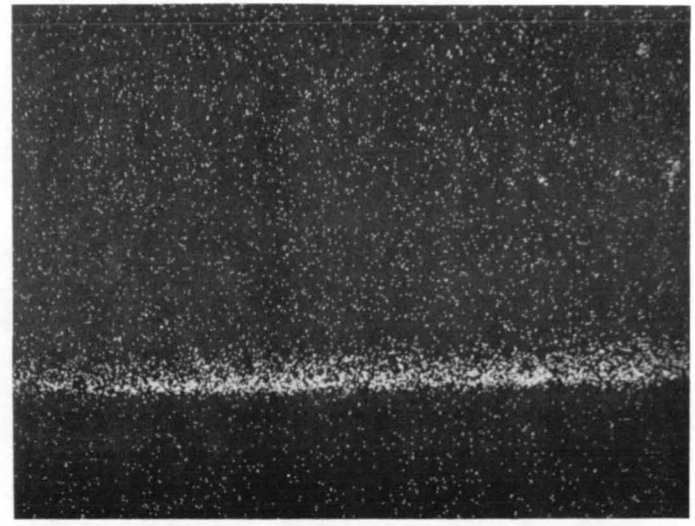

800X

(D) MAGNESIUM X-RAY IMAGE

Figure 5-10 Backscattered electron image photograph (a) and x-ray image photographs showing the distribution of sulfur, sodium, and magnesium (b-d, respectively) in Task III coating system 16 (EB-PVD 6 w% Y_2O_3-ZrO_2) after 444 hours (cycles) of cyclic hot corrosion rig testing at 954°C (1750°F) ceramic surface temperature and 899°C (1650°F) metal substrate temperature.

TABLE 5-V

PLASMA SPRAY COATING SYSTEMS SELECTED FOR TASK IV ENGINE EVALUATION

System Description	Ceramic Composition	Process Details
3	6w%Y_2O_3 - ZrO_2	Coarse Spherical Powder, 149°C (300°F) Substrate Temperature Control, 7.6 cm (3 inches) Gun-to-Specimen Distance
8	6w%Y_2O_3 - ZrO_2	Coarse Spherical Powder, 149°C (300°F) Substrate Temperature Control, 2.5 cm (1 inch) Gun-to-Specimen Distance

6.0 CONCLUSIONS

Based on the results of the initial burner rig screening tests, it is concluded that partially stabilized zirconia containing six weight percent yttria is the best of the tested ceramic compositions.

Based on results of the process optimization studies, it is concluded that processes which favor the formation of strain tolerant ceramic microstructures can provide substantial (more than 3X) benefits to cyclic thermal durability of ceramic coatings. The processes included electron beam - physical vapor deposition, optimization of plasma powder morphology, high energy plasma deposition, and ceramic residual stress control.

Results of cyclic oxidation tests on candidate optimized systems indicate ceramic durability comparable to over 15,000 engine flight hours. While the coating was found to be susceptible to failure as a result of corrodent infiltration under hot corrosion conditions, not enough is currently known about life prediction of ceramic coating performance from laboratory corrosion data to quantitatively predict airfoil coating life from the hot corrosion results.

Metallographic observation of failed coatings (spallation over 50 percent of the test zone) indicated that, under all test conditions except cyclic hot corrosion, spallation of the coating resulted from the formation of a dominant crack parallel and adjacent to, but not coincident with, the metal-ceramic interface. The formation of an MCrAlY oxide scale was clearly visible at the metal-ceramic interface. However, the data generated were not sufficient to determine the influence of this scale on coating failure or to separate the effects of thermal exposure (time at temperature) versus thermally induced stress cycling on coating life. In addition to cracking at the metal-ceramic interface, spalling of the ceramic in the outer layers was also seen in hot corrosion exposed specimens.

Based on the results of this program, two coating systems were considered suitable for experimental engine evaluation. These systems were six weight percent yttria stabilized zirconia plasma sprayed with two different process parameters. While performance of electron beam - physical vapor deposited coatings generally was outstanding, this coating was not considered a candidate for engine evaluation because reproducible process methods for application to complex geometry turbine components have not yet been demonstrated.

APPENDIX A
UNCOOLED BURNER RIG TEST DETAILS

The uncooled burner rig test employed in Tasks I and II involves cyclic flame heating and forced air cooling of coated cyclinderical test specimens illustrated in Figure A-1. A set of 12 specimens installed on a spindle ready for testing is shown in Figure A-2. These bars are rotated in the exhaust gases of a jet fuel burner rig (Figure A-3) to provide a uniform temperature for all specimens. The exhaust gases are the combustion products of Jet A fuel and air, with a velocity of Mach 0.3. Specimen temperature is monitored and controlled using an optical pyrometer and automatic feedback controller. Emittance of the bars is periodically measured and corrections are made to maintain the desired set point temperature. During rig operation the fuel pressure is regulated automatically to maintain the desired temperature. To provide cyclic cooling, the burner is automatically moved away from the specimens for the cool-down portion of the cycle, during which a compressed air blast is applied to the specimens. Cycle duration totals six minutes, with four minutes in the flame and two minutes of forced air cooling. Testing is interrupted approximately every 20 hours to allow for visual examination of the specimens. Failure is considered to have occurred when spallation occurs over approximately 50 percent of the "test" zone of the bar. The "test" zone includes an area which is approximately 2.5 cm (1 inch) long at the center of the exposed portion of the bar, having a uniform temperature during testing. This failure criterion recognizes that some ceramic loss may occur without severe degradation of the protective nature of the ceramic. It should be noted that once initiated, spallation failure propagates relatively rapidly, so that the stated coating life is not highly sensitive to end point definitions.

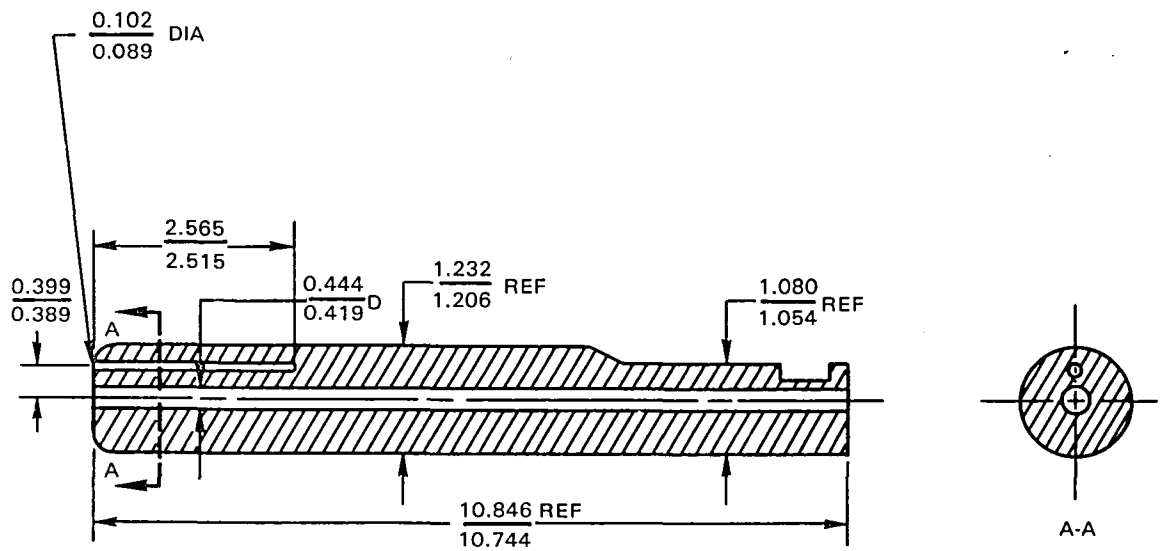

Figure A-1 Diagram of Specimen Used for Burner Rig Testing. Dimensions are expressed in centimeters.

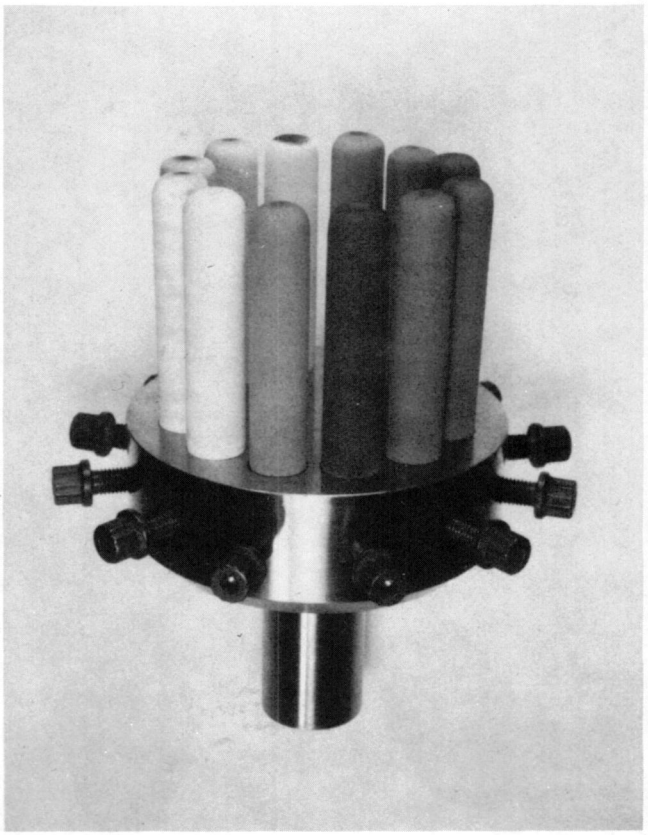

Figure A-2 Specimens in Fixture Ready for Burner Rig Testing. Coating color variations are due to slight losses of stoichiometry (oxygen depletion) from the heat treat operation.

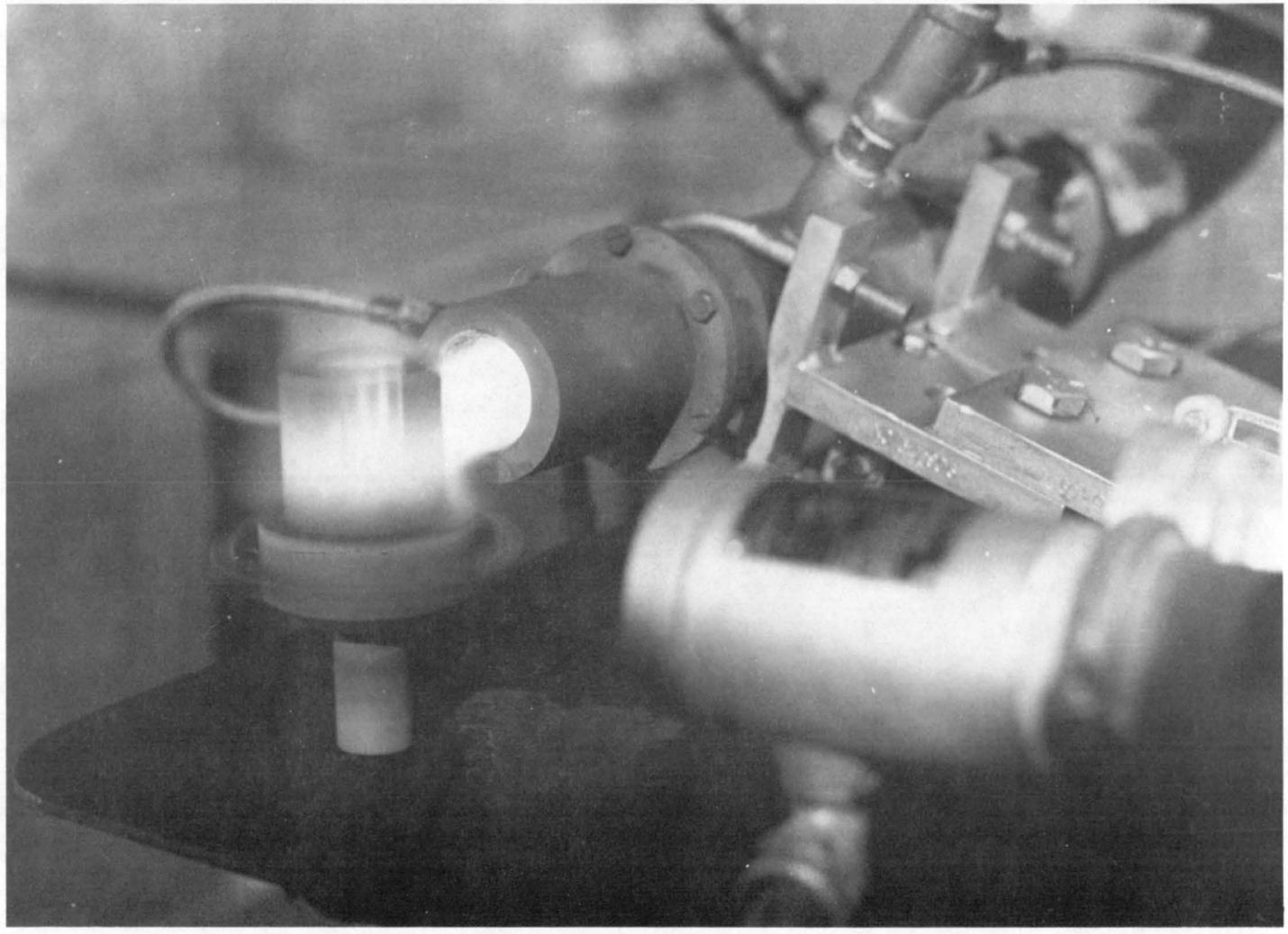

Figure A-3 Burner Rig in Operation during the Hot Portion of the Cycle.

APPENDIX B
OXIDATION BURNER RIG TEST

The cyclic oxidation exposure burner rig test utilized in Task III defined the capabilities of improved coating systems selected from Task II under simulated field service oxidation conditions. The test rig is similar to that previously described in Appendix A in that it maintains full automatic control of test temperature and cooling cycles; it also features a special rotating specimen mounting fixture, shown in Figure B-1, with internal passages and flow valves for individual control of internal specimen cooling air impingement tubes inside the hollow test specimens. This fixture provides for simultaneous test of twelve air-cooled specimens. The test specimen illustrated in Figure B-2 permits internal cooling and temperature monitoring during rig testing.

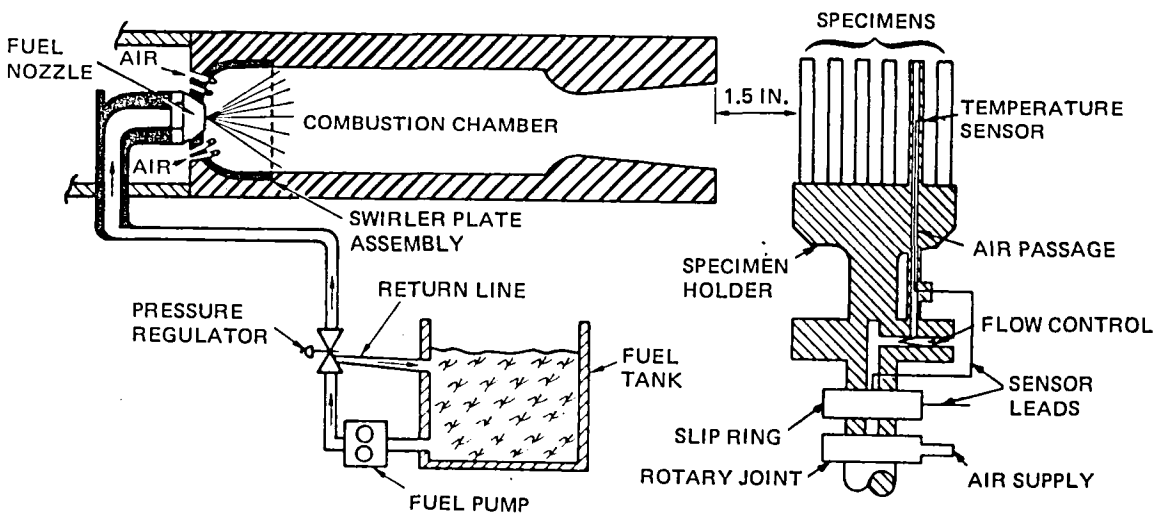

Figure B-1 Schematic Diagram of Burner Rig Test Apparatus for Cyclic Oxidation Exposure in Task III

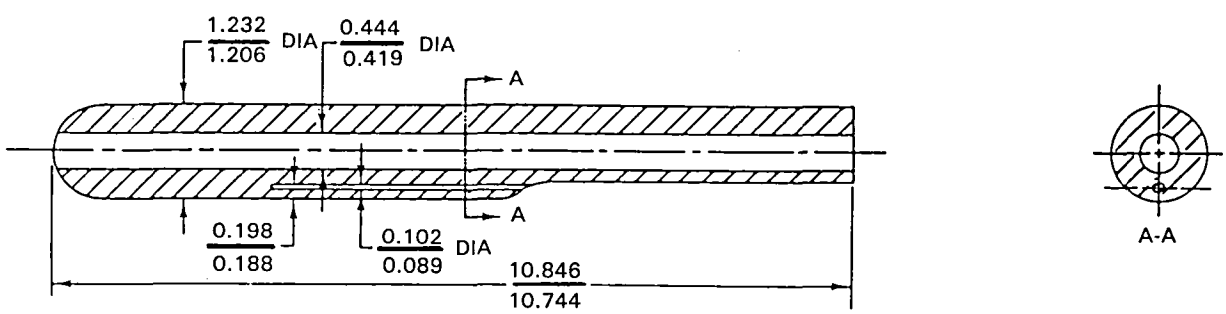

Figure B-2 Oxidation/Corrosion Burner Rig Test Specimen. Dimensions are expressed in centimeters.

The rig is operated with an unrestricted burner exhaust to the specimen area as shown in the schematic in Figure B-1. This unducted design has been selected since clean fuel oxidation test conditions do not require controlled addition of air contaminants as required for hot corrosion evaluation.

Basic burner operation is controlled by using an infrared optical device calibrated to read the ceramic coating surface temperature of the specimens. The output of the infrared detector is fed through automatic devices which vary fuel pressure and consequently control gas temperatures. In addition, four specimens in each rotating cluster are instrumented with type "S" immersion thermocouples installed to measure the metal temperature in the substrate 1.02 mm (0.040 inches) below the interface between the substrate and the metallic coating layer in the ceramic coating system. The thermocouple signals are passed through multi-channel mercury slip rings to automatic monitoring devices for measurement of specimen temperatures.

Prior to the initiation of testing, the cooling air flow is balanced to equivalent values for all specimens in the cluster using flow meters and the integral flow control valving used in the specimen fixture (Figure B-1). The specimen metal temperature is then maintained by control of air supply pressure during testing.

The cyclic oxidation test conditions were 1148°C (2100°F) ceramic surface temperature and 982°C (1800°F) metal temperature. These conditions were selected to simulate typical anticipated operating conditions for a thermal barrier coated turbine airfoil. The one hour test cycle used in this exposure was 57 minutes flame immersion and three minutes forced air cool.

APPENDIX C
CORROSION BURNER RIG TEST

A cyclic hot corrosion test was also utilized in Task III to aid in defining the capabilities of coating systems selected from Task II under simulated field service conditions. Specific test conditions were selected to model a mixed oxidation-hot corrosion type of exposure encountered in relatively high temperature aircraft turbine exposure with "clean" fuels and moderate atmospheric contaminants.

Intensive study of hot corrosion phenomena at Pratt & Whitney Aircraft has shown that the primary contaminants responsible for hot corrosion attack in aircraft turbine engines operating on clean fuels are sea salt from near ground level air (ingested during take-off) and sulfur trioxide from the combustion gases. A comprehensive analysis of hot corrosion mechanisms has shown conclusively that acidification of contaminant salt deposits by sulfur trioxide is critically related to turbine hot corrosion and that meaningful laboratory hot corrosion testing requires that the activity of SO_3 be maintained at levels characteristic of turbine operation. Accordingly, the hot corrosion test rig used in Task III provides for control of both salt contaminant loading and for control of combustion gas composition by effectively limiting excess dilution air.

The test rig used in the hot corrosion exposure evaluation was specifically designed for evaluation of turbine materials in contaminated environmental conditions. The rig is similar to that previously described in Appendix B for oxidation test evaluation in that it maintains full automatic control of test temperature and cooling cycles and that it features a special rotating specimen mounting fixture with internal passages and flow valves for individual control of internal specimen cooling air. This fixture provides for simultaneous test of twelve air-cooled specimens. There is also provision for metered injection of contaminants to allow accurate simulation of aircraft turbine environments. Temperature control of the hot corrosion test rig is conducted in the same manner as previously discussed for oxidation test rigs.

The major modification in the hot corrosion test rig is that the cooled specimen cluster is operated inside a burner exhaust gas duct as shown schematically in Figure C-1. This ducted exhaust allows specific restriction of ambient air dilution and consequently provides for optimum control of the level of exhaust gas sulfur and air contaminants.

The hot corrosion test conditions used in Task III simulate typical hot corrosion conditions encountered in near ground aircraft engine operation. Selection of the 899°C (1650°F) metal temperature and the 954°C (1750°F) ceramic surface temperature were based on conditions that exist where major salt loading from atmosphere contamination occurs. The test cycle was the same as that used for cyclic oxidation testing, i.e., 57 minutes in the flame and three minutes for air cooling.

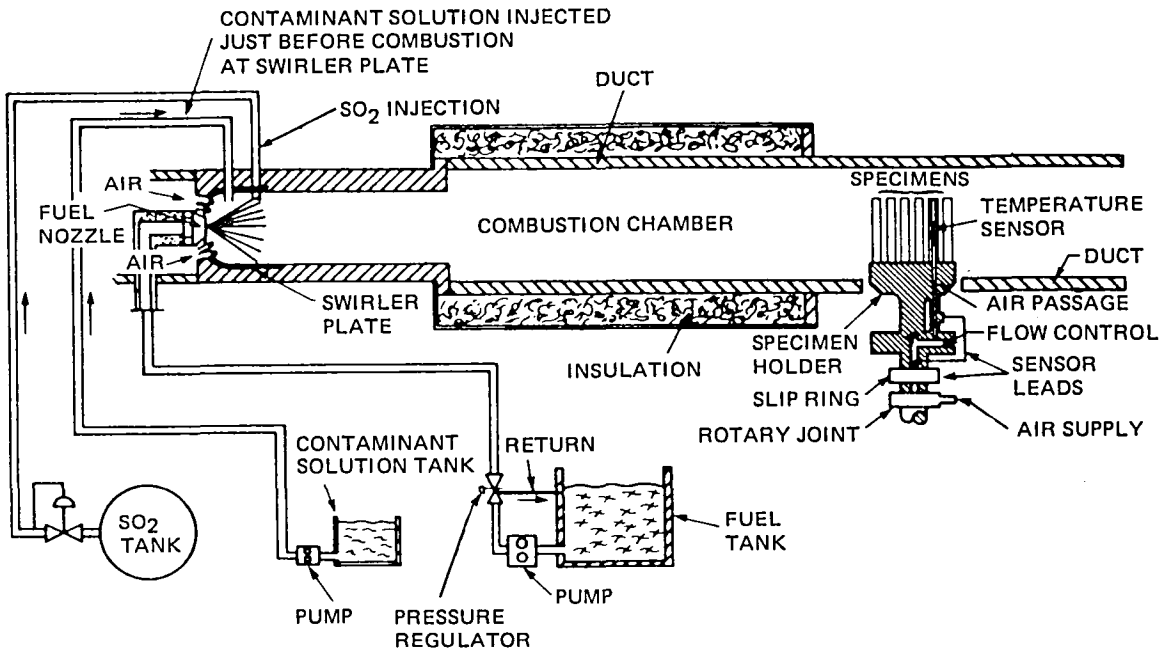

Figure C-1 Schematic Diagram of Ducted Burner Rig Test Apparatus for Task III Hot Corrosion Exposure. Test specimens are enclosed to allow precise control of SO_3 and other contaminants.

REFERENCES

1. Liebert, C., et. al., "Durability of Zirconia Thermal Barrier Ceramic Coatings on Air Cooled Turbine Blades in Cyclic Jet Engine Operation", NASA TM X-3410, 1976.

2. Grisaffe, S. J. and Levine, S. R., Proceedings of First DOE/EPRI Conference on Advanced Materials for Alternative Fuel Capable Directly Fired Heat Engines, Castine, ME, 1979, p. 680.

3. Ruckle, D. L., "Evaluation of PLasma Sprayed Ceramic Coatings for Turbine Engine Components", Thin Solid Films, 64 (1979), p. 327.

4. Bratton, R. J., et. al., "Evaluation of Present Day Thermal Barrier Coatings for Industrial/Utility Applications", Thin Solid Films, 73 (1980), p. 429.

5. McKee, D. W., et. al., "Resistance of Plasma Sprayed Ceramic Thermal Barrier Coatings for Gas Turbine Applications", Proceedings of First DOE/EPRI Conference on Advanced Materials for Alternative Fuel Capable Directly Fired Heat Engines, Castine, ME, 1979, p. 258.

6. Hodge, P. E., et. al., "Evaluation of the Hot Corrosion Behavior of Thermal Barrier Coatings", Thin Solid Films, 73 (1980), p. 447.

7. Stecura, S., "Two Layer Thermal Barrier Coating for High Temperature Components", American Ceramic Society Bulletin, 56(12), Dec. 1977.

8. Grot, A. S. and Martyn, J. K., "Behavior of Plasma Sprayed Ceramic Thermal Barrier Coating for Gas Turbine Applications", American Ceramic Society Bulletin, 60(8), Aug. 1981, p. 807.

9. Sumner, I. E. and Ruckle, D., "Development of Improved Durability Plasma Sprayed Ceramic Coatings for Gas Turbine Engines", AIAA Paper No. 80-1193, June 1980.

10. Cassenti, B. N., Brinkley, A. M. and Sinko, G. C., "Thermal and Stress Analysis of Thermal Barrier Coatings", AIAA Paper No. 81-1482, July 1981.

11. Sheffler, K. D., Graziani, R. A. and Sinko, G. C., "JT9D Thermal Barrier Coated Vanes", NASA CR-167964, 1982.

12. Ruckle, D. L., "Plasma Sprayed Ceramic Thermal Barrier Coatings for Turbine Vane Platforms", Thin Solid Films, 73 (1980) pp. 455-461.

13. Scott, H. G., "Phase Relationships in the Zirconia-Yttria System", Journal of Materials Science, 10 (1975) pp. 1527-1535.

14. Viechnicki, D. and Stubican, V. S., "Mechanism of Decomposition of the Cubic Solid Solutions in the System ZrO_2-MgO", Journal of the American Ceramic Society, 48 (1965), p. 292.

15. Stubican, V. S., et. al., "Phase Equilibria and Ordering in the System ZrO_2-Y_2O_3", Journal of the American Ceramic Society, 61 (1978), pp. 17-21.

16. Levine, S. R., "Adhesive/Cohesive Strength of a ZrO_2-12 w% Y_2O_3/NiCrAlY Thermal Barrier Coating", NASA TM-73792, 1978.

17. Stecura, S., "Effect of Compositional Changes on the Performance of a Thermal Barrier Coating System", NASA TM-78976, 1979.

18. Hodge, P. E., et. al., "Thermal Barrier Coatings: Burner Rig Hot Corrosion Test Results", NASA TM-79005, 1978.

19. Gedwill, M. A., "Improved Bond Coatings for Use with Thermal Barrier Coatings", NASA TM-81567, 1980.

20. Gedwill, M. A., "Burner Rig Evaluation of Thermal Barrier Coating Systems for Nickel Base Alloys", NASA TM-81685, 1981.

21. Hodge, P. E., et. al., "Evaluation of Hot Corrosion Behavior of Thermal Barrier Coatings", NASA TM-81520, 1980.

DISTRIBUTION LIST

GOVERNMENT AGENCIES

NASA Headquarters
600 Independence Avenue
Washington, DC 20546
Attention: Dr. R. Colladay/RW
Dr. M. Greenfield/RWM
Dr. L. Harris/RW

NASA Lewis Research Center
21000 Brookpark Road
Cleveland, OH 44135

Attention: Mr. S.J. Grisaffe	MS 49-1
Dr. S.R. Levine	M.S. 105-1
Library	MS 60-3 (2 copies)
Mr. Curt Liebert	MS 77-2
Materials Division File	MS 49-1
Material, Struct. & Grants Sec.	MS 501-305
Mr. J. P. Merutka	MS 105-1 (25 copies)
Mr. N. T. Musial	MS 500-113
Mr. Al Powers	MS 501-10
Report Control Office	MS 5-5
Mr. John E. Rohde	MS 77-2
Technology Utilization	MS 3-19
Army R&T Propulsion Laboratory	MS 302-2

NASA Ames Research Center
Moffett Field, CA 94035
Attention: Library

NASA Goddard Space Flight Center
Greenbelt, Maryland 20771
Attention: Library

NASA Langley Research Center
Langley Field, VA 23665
Attention: Library, M.S. 185
Mr. B. Stein, MS 188-B

NASA Manned Spaced Craft Center
Houston, Texas 77058
Attention: Technical Library, Code JM6

NASA George C. Marshall Space Center
Marshall SFC, AL 35812
Attention: Mr. Gene Cataldo
Library

NASA Scientific and Technical Information Facility
P.O. Box 8757
B.W.I. Airport, Maryland 21240
Attention: Acquisition Dept. (25 copies)

Applied Technology Lab
DAVDL-ATP-ATP
Ft. Eustis, VA 23604
Attention: J. Lane

Army Aviation R&D Com.
4300 Goodfellow
St. Louis, MO 63120
Attention: Mr. Mike Bauccio DRDAV-DS

Army Material & Mech. Research Center
Arsonel Street
Watertown, MA 02192
Attention: Mr. Joseph J. Falco
Mr. C. Levy, Building 312

Department of Energy
Office of Coal Utilities
Germantown, MD 20767
Attention: Mr. J. Fairbanks MS E178

Department of Energy
20 Massachusetts Avenue
Washington, DC 20545
Attention: Mr. S. Dapkunas

Department of the Navy
Naval Air Development Center
Warminster, PA 18974
Attention: Mr. R. Mahorter Code 60634

Department of the Navy
Naval Air System Command
Washington, DC 20361
Attention: Mr. Joe Collins Code Air-5163C

NAVAL Air Propul. Test Center
1440 Parkway Avenue
Trenton, NJ 08628
Attention: Mr. William G. Barker
Mr. R. Dobrowolski, PE 42

Naval Air Propulsion Test Center
Explor. Dev. Branch
Trenton, NJ 08628
Attention: Mr. J. W. Glatz, Material Engr.

Naval Sea Systems Command
Washington, DC 20362
Attention: S. B. Shepard Code 5231

Naval Ship R&D Center
Annapolis, MA 21402
Attention: Mr. G. A. Wacker, Metals Division

Naval Surface Weapons Center
White Oak Laboratory
Silver Spring, MD 20910
Attention: Mr. Charles Rowe K22

D. Taylor Naval Ship
R & D Center
Annapolis, MD 21402
Attention: Mr. L. F. Aprigliano
Dr. Robert Clarke Code 2813

Wright-Patterson Air Force Base
Dayton, Ohio 45433
Attention: Mr. E. E. Bailey AFWAL-DO
Mr. N. Geyer AFWAL/MLLM
Mr. L. Hjelm AFWAL/MLL
Mr. Sylvester Lee AFWAL/MLTM
Mr. Shiro-Fujishiro AFWAL

ENGINE MANUFACTURERS

AVCO-Lycoming
550 S. Main Street
Stratford, CT 06497
Attention: Mr. A. F. Deferrari
Mr. Joseph Goebel
Mr. S. Naik
Mr. Lyle B. Speigel

Cummins Engine Company
1900 McKinley Avenue
Columbus, IN 47201
Attention: Mr. Ray Kamo

Curtiss-Wright Corporation
Materials Engr. Department
One Passaic Street
Woodridge, NJ 07075
Attention: Dr. Sam Wolosin

Detroit Diesel Allison
General Motors Company
P.O. Box 894
Indianapolis, IN 46206
Attention: Mr. D. Hanink
Mr. H. Herman W8
Mr. Kenneth Ryan

General Electric Co.
Aircraft Engine Group
Cincinnati, OH 45215
Attention: Dr. R. G. Carlson Mail Drop M-85
Mr. Ram Darolia MPTL Mail Drop M-85
Mr. H. Heckler Mail Drop D-83
Dr. R. Hillery MPTL, Mail Drop M-85
Mr. E. Kerzicnik, MPTL, Mail Drop M-85
Mr. R. Medios
Mr. David Rigney

General Electric Co.
Evandale, OH 45215
Attention: Mr. E. C. Duderstadt Mail Drop 99

General Electric Co.
Gas Turbine Products Division
Schenectady, NY 12345
Attention: Mr. H. Doering, Bld 53-316
Mr. W. Schilling, Bld 53-316

General Electric Co.
R & D Center
Schenectady, NY 46206
Attention: Mr. M. R. Jackson, K1
Dr. W. B. Hillig, K1, 4A21
Library
Dr. William P. Minnear, K-1, 4A45
Mr. J. R. Rairden, K1
Dr. Paul Siemers, K1, 4A21
Dr. Donald Wood, ID4

Pratt and Whitney Aircraft Group
Commercial Products Division
E. Hartford, CT 06108
Attention: Mr. Scott Duvall
Dr. M. Gell
Dr. D. K. Gupta

Pratt & Whitney Aircraft Group
Government Products Division
West Palm Beach, FL 33402
Attention: Mr. R. Hecht
Library
Mr. R. L. Shamakian

Solar Turbines, Inc.
2200 Pacific Highway
P.O. Box 80966
San Diego, CA 92138
Attention: Ms. Lulu Hsu
Mr. A. R. Stetson
Mr. J. W. Vogan

Solar Turbines Inc.
499 South Capital Street, SW, Suite 422
Washington, DC 20003
Attention: Mr. Don Kearns

Teledyne CAE
1330 Laskey Road
Toledo, Ohio 43612
Attention: Mr. Robert Beck
Mr. Fred Mahler

United Technologies Library
400 Main Street
East Hartford, CT 06108
Attention: M. Donnelly

United Technologies Research Center
Silver Lane
East Hartford, CT 06108
Attention: Mr. N. Bornstein
Dr. E. R. Thompson

Westinghouse Electric
Combustion Turbines System
P.O. Box 251
Concordville, PA 19331
Attention: Ms. Danna Barksdale
Mr. S. T. Scheirer
Mr. Tom Sherlock

AIRFRAME MANUFACTURERS

The Boeing Company
P.O. Box 3707
Seattle, WA 98124
Attention: Propulsion Engineering

AIRLINES

American Airlines
Main. & Engr. Center
Tulsa, OK 74151
Attention: Mr. Sid Glucksman
Mr. P. C. Johnson, Proj. Mgr.

Eastern Airlines, Inc.
International Airport
Miami, FL 33148
Attention: Mr. Mark Fulmer
Mr. Harry A. Hokanson

Pacific Southwest Airlines
7007 Consolidation Way
San Diego, CA 92121
Attention: Mr. Bob Lay

Pam Am World Airways, Inc.
JKF International Airport
Jamaica, NY 11430
Attention: Mr. N. Perenson, Bldg. 208, Rm. 2215E

Trans World Airlines
P. O. Box 20126-R2-452 MCI
Kansas City, MO 64295
Attention: Mr. R. Etzenhouser
Mr. J. R. Jensen

United Air Lines
International Airport
San Francisco, CA 94128
Attention: Mr. W. W. Clarke

UNIVERSITIES

University of California
Lawrence Berkeley Laboratory
Inorganic Material Research
Berkeley, CA 94720
Attention: Dr. Donald H. Boone
Mr. A. V. Levy

University of California
Materials Department
6532 Boelter Hall
Los Angeles, CA 90024
Attention: Dr. R. F. Bunshah

University of Dayton
Research Center R 162 KL
300 College Park Avenue
Dayton, Ohio 45409
Attention: Mr. George A. Graves

Georgetown University
Department of Physics
Washington, DC 20057
Attention: Professor Tran NGOC

University of Illinois
Ceramic Engineering Department
Urbana, IL 61801
Attention: Dr. Sherman D. Brown

Ohio State University
116 West 19th Avenue
Columbus, Ohio 43220
Attention: Professor R. A. Rapp

State University of New York
Department of Materials Science
Stonybrook, L.I., NY 11794
Attention: Professor M. Herman
Professor L. Seigle

OTHERS

Aerospace Corporation
P.O. Box 92957
Los Angeles, California 90009
Attention: Reports Acquisition

Airesearch Mfg. Co.
111 S. 34th Street
Phoenix, AZ 85034
Attention: Mr. Duane Ruckle
Dr. T. E. Strangman

Airesearch Mfg. Co.
2525 W. 190th Street
Torrance, CA 90509
Attention: Mr. D. E. Schwab

Alloy Metals Inc.
501 Executive Drive
Troy, MI 48084
Attention: Mr. Frank Hermanek

Alloy Surfaces Co.
100 S. Justison Street
Wilmington, DE 19899
Attention: Mr. A.L. Baldi
Mr. John M. Richardson, III

Applied Coatings, Inc.
775 Kaderly Drive
Columbus, Ohio 43228
Attention: Dr. H. Beale

Argonne National Lab
9700 South Cass Avenue
Argonne, IL 60439
Attention: Harold Herman

Armco, Inc.
Middletown, Ohio 45043
Attention: Dr. Jerry L. Arnold

AVCO Systems Division
201 Lowell Street
Lowell, MA 01851
Attention: Library

Battelle Memorial Institute
505 King Avenue
Columbus, Ohio 43201
Attention: MCIC
Mr. D. Niesz
Mr. I. G. Wright

Battelle Memorial Institute
Pacific Northwest Laboratories
P.O. Box 999
Richland, WA 99352
Attention: Mr. Darrell Hayes
Dr. John Prater

Brown Boveri Turbomainery
711 Anderson Avenue, North
St. Cloud, Mn 56301
Attention: Mr. Steven Mussman

Bruswick Technetics
2000 Brunswick Lane
Deland, FL 32720
Attention: Mr. David A. Day

Cabot Corporation
Stellite Division
P.O. Box 746
Kokomo, Indiana 46901
Attention: Dr. A. I. Asphahani
Library

Chromalloy R&T
Chromalloy American Group
Blaisdell Road
Orangeburg, NY 10962
Attention: Mr. Charles Ammann
Mr. Volker Wilms

Coating Technology Corp.
2 Commercial Street
Brandford, CT 06405
Attention: Mr. G. W. Goward

Corning-Zircoa
315-1 Solan Road
Solan, Ohio 44139
Attention: Mr. Stanley L. Bost
Mr. D. K. Ratcliffe
Mr. Donald E. Snedecker
Dr. David M. Thompson

Deere & Company
Technical Center
3300 River Drive
Moline, IL 61265
Attention: Dr. Gopal S. Revankar

E.P.R.I.
3412 03 Hillview Avenue
Palo Alto, CA 94304
Attention: Mr. Arthur Cohn
Dr. R. I. Jaffee
Mr. John Stringer

Ford Motor Company
Scientific Laboratory
Dearborn, MI 48121
Attention: Mr. D. Hartsock, Rm E-3172

Mr. James Gangler
6730 Kenwood Forest Lane
Chevy Chase, MD 20815

Howmet Corporation
Technical Center
699 Benston Road
Whithall, MI 49461
Attention: Mr. Elliot Lassow
Mr. S. Shankar

Howmet Turbine Company
475 Steamboat Road
Greenwich, CT 06830
Attention: Mr. W. R. Freeman, Jr.

ITT Research Institute
10 West 35th Street
Chicago, IL 60616
Attention: Mr. Y. Horada
Dr. M. A. H. Howes

Jet Propulsion Lab.
4800 Oak Grove Drive
Pasadena, CA 91103
Attention: Library/Acquisitions

Magnesium Elektron, Inc.
Star Route A, Box 202-1
Fleminton, NJ 08822
Attention: Mr. Mark L. Spinner

METCO Inc.
1101 Prospect Avenue
Westbury, L.I., NY 11590
Attention: Mr. John Klein
Mr. Frank N. Longo
Mr. M. Ortner
Mr. S. Rangaswamy

Norton Co.
1 New Bond Street
Worcester, MA 01606
Attention: Mr. Dean Arvidison, Jr.

DISTRIBUTION LIST (Cont'd)

Plasma Coating Corp.
15331 Avalon
Gardina, CA 90248
Attention: Mr. Andy Mueller

Plasma Technics, Inc.
3717 Mt. Diablo Blvd.
Lafayette, CA 94549
Attention: Mr. S. Mutialu

Rocketdyne
6633 Canoga
Canoga Park, CA 91304
Attention: Mr. A. Lakin, AC-10

Rockwell International
Energy Systems Group
8900 Desoto Avenue
Canoga Park, CA 91304
Attention: Dr. William Lee

San Fernado Laboratories
10258 Norris Avenue
Pacoima, CA 91331
Attention: Mr. Robert A. Holzl

Shell Development Corp.
P.O. Box 1380
Houston, TX 77001
Attention: Mr. Randy C. John

Technical Reports Library
Oak Ridge National Laboratory
Oak Ridge, Tenn. 37830

TRW - AECR
1400 N. Cameron Street
Harrisburg, PA 17105
Attention: John Kocis
Dr. Owen

TRW Equipment
23355 Euclid Avenue
Cleveland, Ohio 44117
Attention: Dr. C. Kortovich
I. M. Matay, TM-2966
J. N. McCarthy, TM-2110
Dr. T. S. Piwonka, TM-2966

Turbine Coat. Facility
2850 Seventh Street
Berkeley, CA 94720
Attention: Mr. W. K. Halnan

Union Carbide Corp.
Linde Division
1500 Polco Street
Indianapolis, IN 46224
Attention: Dr. T. A. Taylor
Dr. R. C. Tucker, Jr.

Westinghouse R & D Center
1310 Beulah Road
Pittsburgh, PA 15235
Attention: C. A. Anderson
Mr. R. J. Bratton
Dr. S. C. Singhal
Mr. R. A. Wenglarz

3M Co., 3M Center
Building 219-1
St. Paul, MN 55144
Attention: Mr. Donald Cardinal